Academic Year 2024-25 DISEG

Politecnico di Torino

Master thesis on

Structural Assessment of Ferrocement Elements Using Four-Point Bending Tests and Digital Image Correlation

Master's degree in civil engineering

Candidate:
Soheila Albooyeh

Supervisor:
Prof. Francesco Tondolo

Contents

1 INTRODUCTION 1

2 THEORETICAL BACKGROUND OF FERROCEMENT 5

2.1 Introduction of Ferrocement 5

2.2 Mechanical Behavior of Ferrocement under Flexural Loading 7

2.3 Previous Experimental Studies on Ferrocement Beams and Panels 9

2.4 Analytical Formulation and Theoretical Framework 12

2.5 Non-Destructive and Optical Techniques for Structural Assessment 13

3 GEOMETRIC FRAMEWORK OF THE ESPOSIZIONI STRUCTURE IN TORINO ... 15

3.1 Spatial Configuration of Hall C and Its Structural Scheme 15

3.2 Historical Sources, Design Documents, and On-Site Metric Evidence 16

3.3 Extraction of the Undulated Ferrocement Geometry for the Mock-Up 20

4 EXPERIMENTAL RESULTS AND DISCUSSSION 22

4.1 Ferrocement Analysis 23

4.1.1 Test Setup 24

4.2 Matlab work 26

4.3 Flexural Load–Deflection Response of Ferrocement Beam 26

4.4 Load–Time Response 28

4.5 Load–Strain Relationship (strain Gauges) 28

4.5.1 Load–Strain Relationship – Top Gauges (Compression) 29

4.5.2 Load–Strain Relationship – Bottom (tension) Gauges 31

4.6 Strain Analysis in the Digital Image Correlation (DIC) zone 32

4.7 Deflection Analysis Using Displacement Transducers (LVDTs) 33

4.8 Macroscopic Observations 36

5 DIGITAL IMAGE CORRELATION 38

5.1 Optical Properties 39

5.1.1 Focal length 39

5.1.2 Circle of Confusion of the circle 39

5.1.3 Aperture (Diaphragm) 39

5.1.4 Exposure time 40

5.1.5 ISO sensitivity 40

5.1.6 Hyperfocal distance 40

5.1.7 Angle of view 40

5.1.8 Field of View (FOV) 40

5.1.9 Depth of Field (DOF) 41

5.2 Digital Image Correlation Process 41

5.2.1 Subset Definition and Correlation Principal size 41

5.2.2 Subset Spacing and Grid Resolution 41

5.2.3 Correlation Criteria and Matching Accuracy 42

5.2.4 Shape Functions and Local Deformation Mapping 43

5.2.5 Strain Computation 43

5.2.6 Error Sources and Mitigation **43**

5.2.7 Out-of-Plane Motion and Correlation Loss **44**

6 DIGITAL IMAGE PRELIMINARY COMPRESSION TEST ON CONCRETE CUBE WITH VIC-2D **45**

6.1 Purpose of the Preliminary Test ***45***

6.1.1 Specimen Preparation and Pattern Application **46**

6.1.2 Final Protocol for Speckle Pattern Application: **49**

6.1.3 Silicone Curvature Phenomenon **52**

6.1.4 Silicone Stencil Behavior and Speckle Application **53**

6.2 Camera Setup and Calibration for Digital Image Correlation ***55***

6.2.1 Equipment Description **55**

6.2.2 Camera Calibration and Parameter Selection **56**

6.2.3 Image Processing and Analysis in VIC-2D **57**

6.2.4 Loading Procedure **57**

6.2.5 Noise Analysis and Observations **57**

6.3 Conclusions about the Preliminary Test ***58***

7 DIGITAL IMAGE CORRELATION WITH NCORR **60**

7.1 Explanation of NCORR ***60***

7.2 NCORR Procedure ***61***

7.3 Discussion and Concluding Remarks ***61***

7.4 NCORR Analysis Workflow ***62***

7.4.1 Definition of the Region of Interest (ROI) **62**

7.4.2 Choice of subset parameters 63

7.4.3 Seed placement and start of correlation 64

7.4.4 Calibration and strain computation 65

7.5 Local NCORR Analysis of the Bottom Part of the Beam 66

7.5.1 Strain State at 20 kN – Fully Elastic Response (Bottom Part) 67

7.5.2 Strain State at 30 kN – First Tensile Concentration (Bottom Part) 68

7.5.3 Strain State at 50 kN – Crack Initiation (Bottom Part) 70

7.5.4 Strain State at 70 KN – Fully Developed Diagonal Shear Crack (Bottom Part) 72

7.6 Local NCORR Analysis of the Upper Part of the Beam 74

7.6.1 Strain State at 20 KN – Uniform Elastic Compression 74

7.6.2 Strain State at 30 KN – Development of Compression Gradient 75

7.6.3 Strain State at 50 KN – Shear–Compression Interaction 77

7.6.4 Strain State at 70 KN – Fully Developed Compressive–Shear Band 78

7.6.5 Summary of Strain Evolution in the Upper Part 79

7.7 Consistency between Sensor-Based (Matlab) and DIC-Based (Ncorr) Results 81

7.7.1 Introduction 81

7.8 Results and Interpretation After normalization: 95

7.8.1 Residual differences (10–30%) are expected because: 95

7.9 Results 96

8 CONCLUSIONS 97

8.1 Integration of Geometry, Materials, and Full-Scale Testing 97

8.2 Global Structural Response Under Four-Point Bending 97

8.3 Strain Behavior from Strain Gauges 97

8.4 Validation and Performance of Digital Image Correlation 98

8.4.1 VIC-2D Preliminary Test 98

8.4.2 NCORR Main Test 98

8.5 Crack Evolution and Failure Mechanism 98

8.6 Consistency Between Analytical, Sensor-Based and DIC Results 98

8.7 Limitations of the Study 99

8.8 Recommendations for Future Research 99

8.9 Final Summary 99

References 101

List of figures

Figure 1.1 Average crack width of the slabs measured at ultimate loads using DIC 3
Figure 2.1 Panel layer thickness details 6
Figure 2.2 Typical failure of ferrocement (a) on the front face, (b) on the rear face. 9
Figure 2.3 Palazzetto dello Sport, Rome, Italy (1957) 10
Figure 2.4 Torino Esposizioni (Pavillion C), Turin, Italy 11
Figure 2.5 Stadio Flaminio, Rome, Italy (1959) 11
Figure 2.6 Four-point bending test (FPBT) setup and digital image correlation (DIC) zones. 12
Figure 3.1 Hall C in Torino Expositions, the inclined arches and the ribbed ferrocement vault..15
Figure 3.2 UAV image; the Hall C during its construction site in images of the time in 1950....17
Figure 3.3 Historical drawings for hall C, from CSAC Archive, Parma 18
Figure 3.4 Deviation map comparing the NURBS model 19
Figure 3.5 Cracking pattern observed at the base of the inclined 20
Figure 3.6 Schematic representation of the full-scale mock-up cross-section 21
Figure 4.1 Displacement Transducers 22
Figure 4.2 Strain Gauges 22
Figure 4.3 Area of DIC drawing 23
Figure 4.4 ferrocement surface 24
Figure 4.5 Beam preparation, test environment and installation of the camera prior to testing ...25
Figure 4.6 setup of the beam 26
Figure 4.7 Global Load-Deflection response 27
Figure 4.8 Applied load as a function of time 28
Figure 4.9 Load–strain relationship of top compression gauges 29
Figure 4.10 Load–strain relationship 5 30
Figure 4.11 Top compression Gauges 31
Figure 4.12Bottom partSG3 31
Figure 4.13 Bottom part SG6 32
Figure 4.14 Comparative load–strain curves for bottom 32
Figure 4.15 Comparative load–strain curves 33
Figure 4.16 Displacement Transducers drawing 34
Figure 4.17 load deflection on right side 35
Figure 4.18 load deflection of supports on right side 35

Figure 4.19 load-deflection supports on right side 36
Figure 4.20 load Deflection right side 36
Figure 4.21 Left, sliding of the beam on supports, Right deformation at the end of the test. 37
Figure 4.22 Appearance of the plane rupture 37
Figure 6.1cube 150*150 cm 45
Figure 6.2: laboratory of politecnico di Torino 46
Figure 6.3 concrete cube 46
Figure 6.4 manual marking 48
Figure 6.5 stencil and spray Method 49
Figure 6.6 Spray application using a test stencil 50
Figure 6.7 Illustration of speckle pattern quality 51
Figure 6.8 Example of stencil produced by a commercial supplier 52
Figure 6.9 silicone curvature during spray application 53
Figure 6.10 Behavior of the stencil: Left, without holes; Right, with holes (5 cm × 5 cm) 53
Figure 6.11 Results of spray application with different methods. 54
Figure 6.12 Application of the speckle pattern on the beam 55
Figure 6.13 Camera used during calibration and testing 56
Figure 6.14 camera settings 57
Figure 6.15results of the test in excel file 59
Figure 6.16 strain Measurements 59
Figure 7.1 NCORR main interface inserting the photos 62
Figure 7.2 Definition of the Region of Interest on the reference image 63
Figure 7.3 Window for the definition of subset radius and subset spacing in NCORR 64
Figure 7.4 Window for the definition of seeds 65
Figure 7.5 window with displacement and strain fields after calibration 66
Figure 7.6 Bottom part of Beam, εyy at 20 kN 68
Figure 7.7 Bottom part of Beam, εyy at 30 KN 69
Figure 7.8 Bottom part of Beam, εyy at 50 kN 71
Figure 7.9 Bottom part of Beam, εyy at 70 kN 74
Figure 7.10 Upper surface of the beam, εyy at 20 kN with Points A and B. 75
7.11 Upper surface of the beam, εyy at 30 kN with Points A and B. 76
Figure 7.12 Upper surface of the beam, εyy at 50 kN with Points A and B. 78

Figure 7.13– Upper surface of the beam, εyy at 70 kN with Points A and B. 79
Figure 7.14 comparison between ncorr and matlab datas 82
Figure 7.15 SG10 at 20KN 83
Figure 7.16 SG9 AT 20KN 83
Figure 7.17 SG8 AT 20 KN 83
Figure 7.18 SG10 AT 30 KN 84
Figure 7.19 SG9 AT 30KN 84
Figure 7.20 SG8 AT 30KN 85
Figure 7.21 SG10 AT 50 KN 85
Figure 7.22 SG9 AT 50 KN 86
Figure 7.23SG8 AT 50 KN 86
Figure 7.24 SG10 AT 70KN 87
Figure 7.25 SG9 AT 70 KN 87
Figure 7.26 SG8 AT 70 KN 88
Figure 7.27 SG4 AT 20 KN 88
Figure 7.28 SG5 AT 20 KN 89
Figure 7.29 SG7 AT 20KN 89
Figure 7.30 SG4 AT 30 KN 90
Figure 7.31 SG 5 AT 30 KN 90
Figure 7.32 SG7 AT 30 KN 91
Figure 7.33 SG4 AT 50KN 91
Figure 7.34 SG 5 AT 50 KN 92
Figure 7.35 SG7 AT 50 KN 92
Figure 7.36 SG4 AT 70 KN 93
Figure 7.37 SG 5 AT 70 KN 93
Figure 7.38 SG 7 AT 70 KN 94
Figure 7.39 Matlab analysis for Bottom gauges in order to the loads 94
Figure 7.40 Matlab analysis for Top gauges in order to the loads 95

1 INTRODUCTION

Ferrocement is a material that bridges engineering innovation and architectural elegance. Its thin mortar layers reinforced with multiple meshes of fine steel wires have long attracted interest for lightweight and efficient construction. Since its early applications in the twentieth century, ferrocement has been valued for combining strength, ductility, and formability. Yet, its performance under mechanical loads remains complex due to distributed reinforcement, small thickness, and the gradual development of cracking. As many existing ferrocement structures face deterioration, accurate structural assessment is essential not only for their preservation but also for advancing modern design practices based on this technology.

Experimental testing remains one of the most effective approaches for understanding the true mechanical behavior of ferrocement components. When coupled with advanced optical measurement techniques, such tests make it possible to identify local deformations, early cracking, and stress redistribution that would otherwise go unnoticed by traditional sensors. Among modern non-contact methods, Digital Image Correlation (DIC) has emerged as one of the most powerful tools in experimental mechanics.

DIC is an optical technique that quantifies full-field displacements and strains by tracking random surface patterns commonly referred to as speckle patterns captured before and after deformation. Each subset of pixels correlated with its deformed counterpart, creating a detailed map of displacement and strain across the specimen. Unlike strain gauges, which provide discrete data points, or mechanical transducers that measure overall deflection, DIC delivers continuous spatial information with sub-pixel precision. This makes it particularly effective for materials such as ferrocement, where multiple cracks form and propagate across small distances, creating highly localized strain fields.

The reliability and resolution of DIC have improved significantly in recent years, supported by advances in imaging sensors, calibration procedures, and data-processing algorithms. Modern DIC systems can capture minute displacements and reveal complex deformation patterns without physically interfering with the specimen. This is particularly valuable in thin ferrocement elements, where even minimal contact instrumentation could alter the local stress field. Furthermore, DIC allows real-time visualization of the deformation process, providing an intuitive and quantitative understanding of how the material responds from the elastic phase to ultimate failure.

Despite its potential, the application of DIC to ferrocement has remained relatively limited compared to other cementitious or composite materials. Most existing studies have focused on small-scale samples or simple bending tests, while comprehensive analyses of full-scale ferrocement elements under four-point bending are still rare. Investigating such configurations is essential, as the four-point bending setup provides a constant bending moment region that allows detailed observation of cracking behavior and strain evolution.

The present work focuses on the structural assessment of ferrocement elements under four-point bending, integrating DIC as the main tool for monitoring the deformation field. The experimental program aims to characterize the flexural response of the material, evaluate its cracking mechanisms, and validate DIC results against conventional measurement systems. High-resolution cameras, precise calibration, and optimized speckle patterns were used to ensure accurate image tracking and reliable data extraction.

This study contributes to a deeper understanding of ferrocement's mechanical behavior and supports the development of DIC as a dependable and high-resolution technique for structural assessment. The main objectives of this research are:

1. To analyze the flexural response and crack evolution of ferrocement beams under controlled four-point bending.
2. To validate and calibrate the Digital Image Correlation method for thin cementitious materials.
3. To contribute to the methodological framework for non-destructive experimental evaluation of ferrocement structures.

By combining conventional structural testing with advanced optical monitoring, this work enhances the experimental understanding of ferrocement behavior and strengthens the methodological foundation for both modern engineering design and the preservation of existing ferrocement structures.

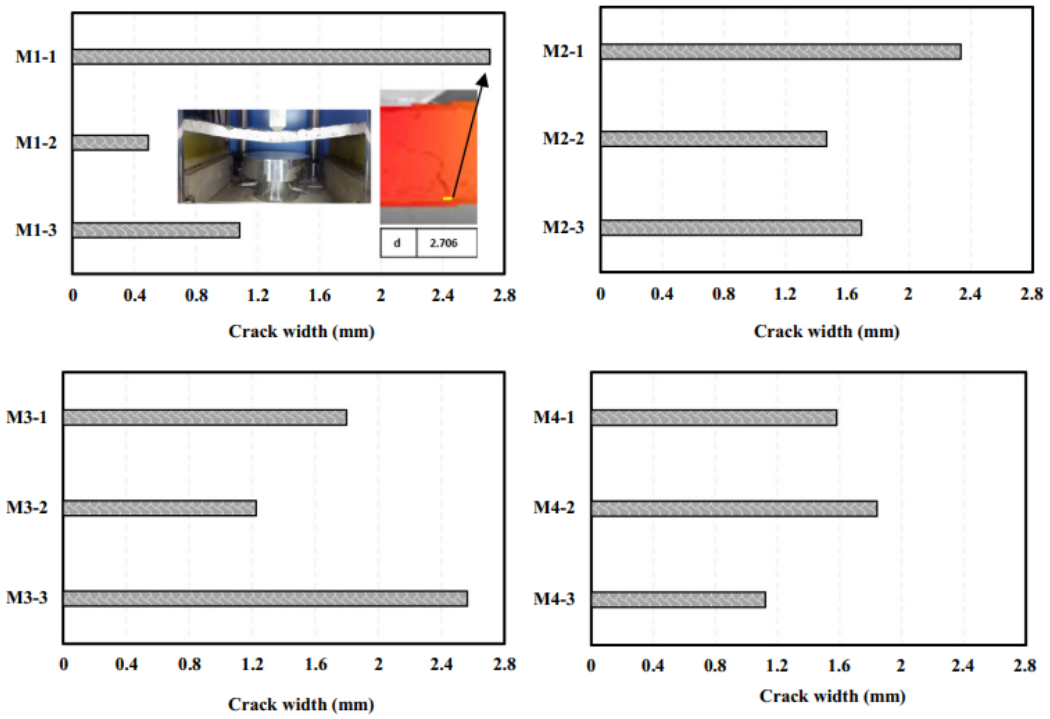

Figure 1.1 Average crack width of the slabs measured at ultimate loads using DIC

The outcomes of this research contribute not only to the ongoing efforts to preserve the legacy of ferrocement structures but also to the advancement of modern structural engineering practices, where precision measurement is increasingly essential for safety verification, material modeling, and performance-based design. A key phase in achieving reliable results was the meticulous preparation of the experimental setup, aimed at maximizing the accuracy and stability of the Digital Image Correlation (DIC) system. Since the quality of optical measurements depend heavily on surface texture and illumination, significant attention was devoted to the preparation of the specimen's surface. A carefully applied speckle pattern composed of fine, high-contrast black dots sprayed uniformly on a matte white background was designed to create optimal image features for correlation tracking. The pattern's density, dot size, and contrast were adjusted through several preliminary trials until consistent results were achieved under laboratory lighting. This ensured that the camera system could detect subtle displacements and strain gradients across the entire observed surface without signal loss or pattern distortion during loading. Following surface preparation, an extensive calibration process was carried out to align the optical system and eliminate geometric distortions between the paired cameras. This step was essential for obtaining high-fidelity images and maintaining sub-pixel precision in the computed displacement fields. Calibration targets and dedicated software were used to establish accurate spatial relationships between the cameras, allowing the DIC algorithms to interpret deformations in true physical coordinates.

Prior to the main testing phase, several trial acquisitions were performed to verify focus, exposure, and image stability. These preliminary tests were followed by a series of controlled load applications, during which high-resolution images were captured continuously at each load increment. Data processing was performed using specialized software packages—VIC-2D and NCorr both of which are widely recognized for their robustness and open accessibility in experimental mechanics. Their use enabled a cross-validation approach: results from one software were compared with those from the other to ensure internal consistency and identify potential differences arising from subset size or correlation algorithms.

The DIC-based measurements were then compared with the readings from conventional instruments such as strain gauges and linear variable displacement transducers (LVDTs). This comparison highlighted the advantages of DIC in capturing full-field deformation patterns with higher spatial resolution, as well as its ability to monitor localized strain concentrations that traditional sensors might overlook. Moreover, DIC proved more flexible in setup, requiring no direct physical contact with the specimen, thus minimizing interference with the structural response. The combined evaluation of these methods not only verified the reliability of DIC for ferrocement testing but also demonstrated its potential as a standard tool for future experimental investigations and structural diagnostics.

2 THEORETICAL BACKGROUND OF FERROCEMENT

2.1 Introduction of Ferrocement

Ferrocement is a thin, high-strength composite material that behaves as a continuous reinforced mortar system. Its efficiency lies in the close spacing of wire mesh layers that distribute tensile stresses uniformly across the section, resulting in multiple fine cracks rather than a few wide ones, a behavior typical of ductile materials. The performance of ferrocement is therefore governed more by mechanical parameters such as mesh configuration, volume fraction of reinforcement, and interface bonding, rather than by the chemical composition of the matrix itself.

The mortar matrix functions as a load-transfer medium that binds the wire meshes and ensures composite action. A well-proportioned mix provides sufficient stiffness to resist deformation while remaining flexible enough to avoid brittle failure. Maintaining a fine aggregate size (≤ 2 mm) allows the mortar to fully penetrate through the mesh layers, producing a uniform and void-free section. The use of superplasticizers or similar admixtures is often necessary to ensure proper compaction and coating of each wire without increasing the water content.

From a structural standpoint, ferrocement panels and beams exhibit an excellent strength-to-weight ratio, making them ideal for lightweight shells, footbridges, and rehabilitation applications. Experimental results indicate that increasing the number of mesh layers or using woven meshes with smaller openings enhances flexural capacity and ductility. However, excessive reinforcement can lead to congestion, poor bonding, and reduced efficiency; therefore, design optimization is essential to achieve the desired stiffness while maintaining constructability.

Another key factor is the matrix–reinforcement interaction, which determines how efficiently load is transferred between materials. A dense matrix ensures high bond strength and limits crack width, while the orientation and tension capacity of the mesh affect stress redistribution during loading. Proper anchorage of mesh edges and overlap between layers are critical for ensuring structural continuity and minimizing stress concentrations. In recent years, ferrocement has gained renewed attention in structural rehabilitation, particularly for strengthening RC slabs, walls, and marine structures where corrosion resistance and crack control are essential. Its ability to form thin, lightweight, and shape-flexible members makes it a sustainable alternative to traditional reinforced concrete in both repair and new construction. Mortar Mix Design and Microstructure, Unlike traditional reinforced concrete, ferrocement relies on a fine mortar matrix without coarse aggregates. The absence of large particles allows the cement paste to penetrate and encapsulate several layers of mesh reinforcement. The mortar typically contains sand with a maximum grain size of about 2 mm,

combined with cement at ratios ranging from 1:2 to 1:3 by weight. The water-to-cement ratio usually lies between 0.35 and 0.45. Maintaining a low water content ensures higher density and compressive strength, though it may reduce workability; therefore, modern admixtures such as superplasticizers are often used to achieve proper flow without compromising compactness. The microstructure of this matrix evolves through hydration, forming a network of C–S–H gel and capillary pores. A controlled curing regime, either water immersion or continuous humid curing for at least two weeks, is vital to sustain hydration and limit shrinkage cracking. The resulting matrix must be sufficiently dense to bond with the reinforcement but also flexible enough to accommodate local strain gradients without brittle failure.

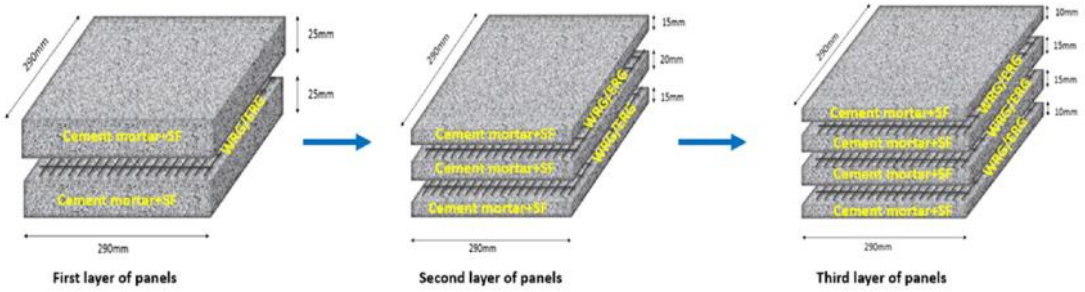

Figure 2.1 Panel layer thickness details

Advances through Supplementary Cementitious Materials (SCMs) in Recent developments in ferrocement have mainly aimed at improving mechanical performance and durability rather than altering its chemical composition. The inclusion of Supplementary Cementitious Materials (SCMs) such as silica fume, fly ash, and ground granulated blast-furnace slag has proven effective in refining the mortar structure and improving long-term performance under service loads. From an engineering perspective, these materials modify the matrix density and stiffness, influencing how stresses are transferred to the mesh reinforcement. Experimental studies have shown that introducing moderate amounts of silica fume into the matrix can increase the ultimate flexural strength of ferrocement slabs by nearly 20 percent, while also improving crack distribution and post-cracking stiffness. Similarly, the inclusion of fly ash has been linked to higher impact resistance and better retention of strength at elevated temperatures. Hybrid systems combining SCMs with small-scale natural fibers, such as human hair or polypropylene strands, show even greater ductility. These fibers act as micro reinforcement bridges, delaying crack propagation and maintaining load-carrying capacity after first cracking. The result is a multi-cracking pattern with narrower crack widths, which is desirable in structural repair and marine applications where corrosion control is critical. In 2023, another investigation explored the performance of ferrocement panels under varying temperature exposures,

revealed that exposure to high temperatures caused dehydration of the C–S–H phase and decomposition of calcium hydroxide, leading to a reduction in strength. However, incorporating fly ash into the mix improved thermal stability by forming additional hydration products that sealed micro voids and mitigated damage. A more recent work in 2025 introduced a hybrid ferrocement matrix incorporating fly ash, silica fume, and human hair fibers. The combination of mineral and organic additives produced a denser and more resilient matrix capable of bridging cracks and resisting sudden failure. The hair fibers acted as micro-reinforcement, increasing the strain capacity, while the pozzolanic materials enhanced bonding between matrix and reinforcement. The overall result was a composite that exhibited multiple fine cracks under bending rather than a few wide ones a desirable trait for ductile ferrocement behavior.

2.2 Mechanical Behavior of Ferrocement under Flexural Loading

The mechanical behavior of ferrocement under flexural loading is distinct from that of ordinary reinforced concrete, mainly because of its finely distributed reinforcement and thin-section geometry. Instead of experiencing a few dominant cracks and sudden loss of stiffness, ferrocement develops numerous fine cracks that gradually spread along the tension zone. This phenomenon, known as *multi-cracking behavior*, enables the structure to maintain integrity even after initial cracking and allows stresses to redistribute more uniformly between the mortar matrix and the mesh reinforcement.

When a ferrocement beam or panel is subjected to bending, its response can typically be divided into three distinct stages:

1. Uncracked Elastic Stage: The material behaves linearly, and both the mortar and the mesh share the applied stress. The stiffness at this stage depends primarily on the modulus of elasticity of the mortar and the reinforcement volume fraction.
2. Cracking and Stress Redistribution: Once the tensile stress in the matrix exceeds its tensile strength, microcracks appear in the tension zone. The load is then progressively transferred to the mesh layers, allowing new cracks to form at nearby locations. This results in a sequence of evenly spaced fine cracks rather than a few wide ones.
3. Post-Cracking and Ultimate Stage: Beyond the stabilized cracking phase, the load–deflection curve shows a gradual reduction in stiffness. Failure may occur either due to yielding or fracture of the mesh, or through crushing of the mortar in the compression zone.

A typical *load–deflection curve* for ferrocement under four-point bending exhibits an initial

linear segment followed by a transition region with multiple cracking and, finally, a plateau leading to failure. The area under the curve is often used as an indicator of toughness and energy absorption, both of which are considerably higher in ferrocement compared to plain mortar elements. Factors Affecting Flexural Strength, several parameters influence the flexural behavior of ferrocement:

1. Type and Geometry of Mesh: The reinforcement mesh (welded, hexagonal, expanded metal, or polymer-based) governs both stiffness and crack spacing. Studies have shown that smaller mesh openings result in higher ultimate loads and better crack control.
2. Number of Layers: Increasing the number of mesh layers enhances the moment capacity but can also raise the risk of incomplete mortar penetration, leading to voids or weak interfaces.
3. Matrix Strength and Bond Quality: A dense, well-cured mortar matrix ensures effective stress transfer and limits premature debonding. The bond between matrix and reinforcement directly affects crack width and propagation rate.
4. Load Configuration and Support Conditions: Four-point bending tests create a constant bending moment region between the two loading points, which helps in identifying true flexural properties without significant shear interference.

Crack Formation and Strain Distribution, the formation of cracks in ferrocement is a progressive process rather than a singular event. As load increases, the matrix first develops invisible microcracks that later merge into visible surface cracks. These cracks tend to initiate near the mid-span region where tensile stresses are highest and propagate upward with further loading. Because of the small thickness of ferrocement sections, the neutral axis shifts rapidly upward during loading, indicating a highly nonlinear strain distribution.The relationship between applied moment and curvature is also nonlinear, with a gradual decrease in stiffness after the first crack. Studies using DIC have provided new insights into this behavior by mapping full-field strain patterns. The advantage of DIC lies in its ability to detect localized deformation zones before cracks become visible to the naked eye, allowing a more detailed understanding of the onset and evolution of damage.

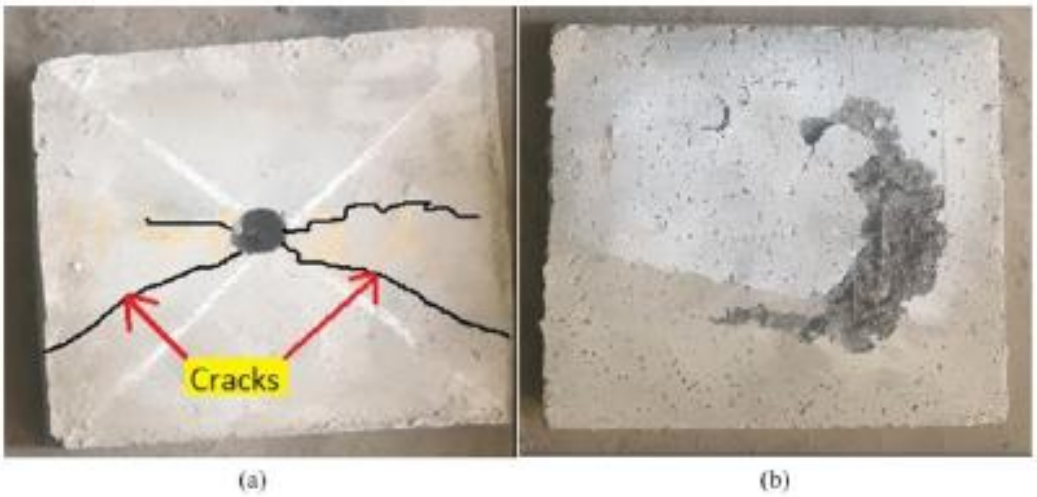

Figure 2.2 Typical failure of ferrocement (a) on the front face, (b) on the rear face.

Moment–Curvature Relationship, the moment–curvature relationship of ferrocement reflects its ability to undergo significant deformation while maintaining load-bearing capacity. The initial linear portion corresponds to elastic bending, while the nonlinear region represents the development of multiple cracks. The curvature at first cracking and at ultimate load are important indicators of ductility. Experimental findings show that ferrocement beams reinforced with multiple mesh layers or improved mortar composition exhibit higher curvature values before failure, confirming their enhanced energy dissipation and deformation capacity.

Failure Modes, Failure in ferrocement beams under flexure can occur through different mechanisms, depending on the reinforcement and matrix properties:

1. Tension failure occurs when the reinforcement yields or fractures after extensive cracking.
2. Compression failure results from crushing of the mortar in the top fiber when the section can no longer resist compression stresses.
3. Debonding or Delamination can occur between mesh and matrix if the bond strength is insufficient.

   Four-point bending tests provide a clear distinction between these failure modes because of the uniform bending region between loading points, allowing the true flexural capacity to be determined without interference from shear.

2.3 Previous Experimental Studies on Ferrocement Beams and Panels

Research on ferrocement flexural behavior has evolved significantly over the past three decades,

shifting from simple strength-based assessments to advanced, full-field deformation monitoring using optical methods such as Digital Image Correlation (DIC). This progression reflects a broader movement within structural engineering toward non-destructive, precision-based evaluation.

Early studies primarily relied on deflection gauges, mechanical dial indicators, and strain gauges attached at discrete points. Although these methods provided valuable insight into load–deflection relationships, they failed to capture the distributed cracking and strain gradients typical of ferrocement structures. Researchers such as Naaman (2000) and Paul & van Zijl (2012) established baseline understanding of ferrocement's multi-cracking behavior and demonstrated how increasing reinforcement ratio enhances ductility and toughness.

Figure 2.3 Palazzetto dello Sport, Rome, Italy (1957)

Figure 2.4 Torino Esposizioni (Pavillion C), Turin, Italy

Figure 2.5 Stadio Flaminio, Rome, Italy (1959)

Later experiments introduced more sophisticated setups involving four-point bending tests (FPBT). The FPBT configuration produces a constant bending moment region between the two loading points, allowing clearer observation of cracking and strain distribution while minimizing

shear influence. A schematic representation is shown in

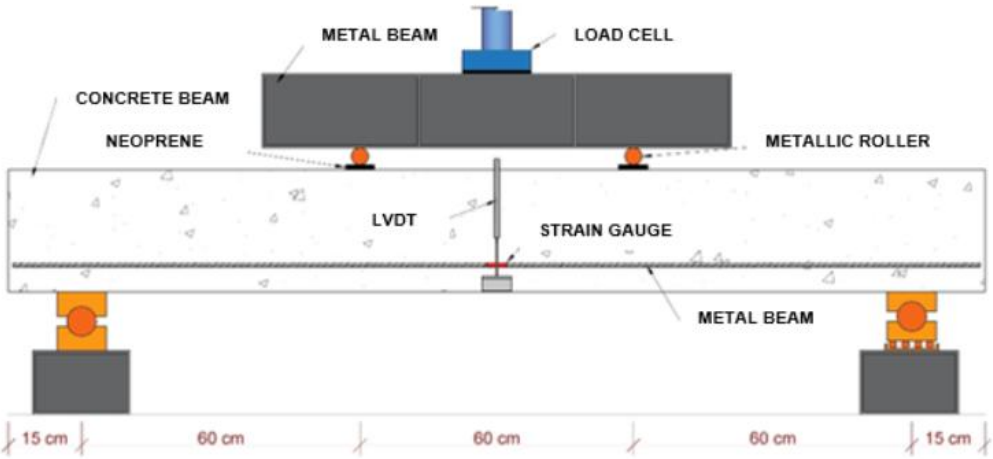

Figure 2.6 Four-point bending test (FPBT) setup and digital image correlation (DIC) zones.

2.4 Analytical Formulation and Theoretical Framework

The load–deformation behavior of ferrocement elements under four-point bending is governed by the relationship between applied moment, curvature, strain distribution, and deflection. Analytical expressions are essential to interpret experimental results obtained through traditional sensors and Digital Image Correlation (DIC). The following equations summarize the theoretical background adopted in this study, based on classical beam theory, empirical relationships, and recent experimental observations.

Static Equilibrium in Four-Point Bending

In the standard four-point bending test (FPBT), the specimen of span $\boldsymbol{L}$is simply supported at both ends, and two equal loads $\frac{\boldsymbol{P}}{\boldsymbol{2}}$are applied symmetrically at a distance $\boldsymbol{a}$from each support.

The shear force and bending moment distribution are expressed as:

$$RA = RB = \frac{P}{2}$$

$$V(x) = \begin{Bmatrix} \frac{P}{2}, 0 < x < a\ ;\ 0, a < x < L - a\ ; \\ -\frac{P}{2}, L - a < x < L \end{Bmatrix}$$

$$M(x) = \begin{Bmatrix} \left(\frac{P}{2}\right)x, 0 < x < a\ ;\ \left(\frac{P}{2}\right)a, a < x < L - a\ ; \\ \left(\frac{P}{2}\right)(L - x), L - a < x < L \end{Bmatrix}$$

The constant moment region between the two loads ($\boldsymbol{a < x < L - a}$) is ideal for strain measurement and DIC observation, since shear effects are negligible and plane sections remain approximately plane.

load–Deflection Relationship, Using effective stiffness, the midspan deflection under an applied load $\boldsymbol{P}$becomes:

$$\delta(P) = \frac{P\, a(3L^2 - 4a^2)}{48\, E\, I_{\text{eff}}(P)}$$

Calibration of Flexural Rigidity Using DIC, By combining DIC-derived curvature $\boldsymbol{\phi_{DIC}}$with the known applied bending moment $\boldsymbol{M = \frac{P}{2}a}$, the experimental flexural rigidity can be evaluated as:

$$(EI)_{\text{exp}} = \frac{M}{\phi_{\text{DIC}}} = \frac{\frac{P}{2}a}{\phi_{\text{DIC}}}$$

This equation provides a direct method to validate the analytical stiffness model and quantify degradation of rigidity due to cracking. The comparison between $\boldsymbol{(EI)_{exp}}$and theoretical $\boldsymbol{EI_{eff}}$helps assess how well the analytical assumptions reflect real material behaviour. Strain Measurement and DIC Derivations For two-dimensional DIC, the in-plane displacement fields $\boldsymbol{u(x,y)}$and $\boldsymbol{v(x,y)}$correspond to horizontal and vertical motions, respectively. The small-strain components are derived as:

$$\varepsilon_{xx} = \frac{\partial u}{\partial x}, \varepsilon_{yy} = \frac{\partial v}{\partial y}, \gamma_{xy} = \frac{\partial u}{\partial y} + \frac{\partial v}{\partial x}$$

These strain maps form the basis for curvature estimation along the beam's height:

$$\phi(x) = \frac{\varepsilon_t(x) - \varepsilon_c(x)}{h}$$

where $\boldsymbol{\varepsilon_t}$and $\boldsymbol{\varepsilon_c}$are the tensile and compressive strains obtained from DIC at the outer fibers. This approach offers high precision without physical sensors and aligns closely with theoretical bending behavior. This relationship enables direct comparison between analytical predictions and DIC-based measurements of deflection or curvature.

2.5 Non-Destructive and Optical Techniques for Structural Assessment

In Accurate evaluation of the structural behavior of ferrocement requires precise and non-invasive measurement techniques. Traditional mechanical sensors, such as strain gauges, LVDTs, and dial indicators, have long been used in laboratory tests to record discrete strain or displacement

data. However, these devices can only measure at specific points, making them less effective for materials like ferrocement, where micro-cracks are widely distributed and deformation is highly localized.

In recent years, the development of optical and image-based techniques has transformed experimental mechanics. Among these methods, Digital Image Correlation (DIC) has emerged as one of the most versatile tools for full-field, non-contact deformation measurement. DIC operates by comparing successive digital images of a speckle-patterned surface during loading. Through mathematical correlation of subsets of pixels, it determines local displacements $(\boldsymbol{u}, \boldsymbol{v})$and subsequently computes strain fields. The technique provides continuous spatial information with sub-pixel accuracy, allowing researchers to visualize complex strain gradients that cannot be captured by traditional sensors.

Compared to ultrasonic pulse velocity, acoustic emission, or laser profilometry, DIC offers a unique advantage: it simultaneously provides both qualitative visualization and quantitative measurement of deformation. It can capture initiation and evolution of cracks, rotation of the neutral axis, and progressive stiffness degradation, all crucial phenomena in ferrocement structures. Moreover, since DIC is non-contact and fully optical, it avoids the interference that bonded sensors may introduce into thin mortar layers.

However, the method also requires meticulous experimental preparation. The quality of the speckle pattern (contrast, size, and uniformity), proper camera calibration, stable lighting conditions, and optimal subset size all play a vital role in the accuracy of correlation results. Modern open-source and commercial software such as *Ncorr*, *VIC-2D*, and *GOM Correlate* include built-in filtering and calibration routines that have made DIC practical for both small-scale and full-scale structural tests.

In the context of this research, DIC serves as the primary measurement system for capturing strain, curvature, and crack evolution on the surface of the ferrocement beam. The integration of DIC with load–deflection data allows a precise, full-field interpretation of the flexural response, bridging the gap between theoretical models and experimental evidence.

3 GEOMETRIC FRAMEWORK OF THE ESPOSIZIONI STRUCTURE IN TORINO

3.1 Spatial Configuration of Hall C and Its Structural Scheme

Hall C of the Torino Expositions complex, designed by Pier Luigi Nervi between 1949 and 1950, represents one of the most refined applications of mid-century ferrocement technology.

Figure 3.1 Hall C in Torino Expositions, the inclined arches and the ribbed ferrocement vault.

The pavilion consists of a rectangular plan (approximately 50 × 65 m) covered by a ribbed ferrocement vault supported by four inclined reinforced-concrete arches.

This hybrid system, combining precast ferrocement thin elements with in-situ concrete, creates a spatial structure where geometry plays a critical mechanical role. The vaulted roof is formed by precast ferrocement panels 2–4 cm thick, used both as lost formwork and as a structural skin. These panels host cast-in-place ribs arranged at 45°, forming a stiffened shell with a lightweight yet load-effective configuration. At the perimeter, a continuous undulated slab made of 9.5 m long corrugated ferrocement elements provide horizontal stiffness and redistributes the outward thrust of the vault toward the arches. The four arches, inclined to align with the resultant of the vault and slab forces, act as the primary load-bearing elements. Archival records show that Nervi specified two distinct concrete mixes—Type 500 and Type 680—depending on the stress hierarchy along the arch. Recent diagnostic campaigns confirmed this differentiation.

Together, these components form a geometric system where the morphology of each element vault curvature, rib spacing, corrugation amplitude, and arch inclination determines the global structural behavior.

3.2 Historical Sources, Design Documents, and On-Site Metric Evidence

The geometry of Hall C has been documented extensively through a combination of archival material and modern survey techniques.

(a)

(b)

Figure 3.2 UAV image; the Hall C during its construction site in images of the time in 1950

Original drawings stored at the CSAC Archives in Parma include cross-sections, profiles of ferrocement waves, reinforcement layouts, and construction-stage photographs. Recent multidisciplinary research campaigns complemented these documents with high-resolution metric data. UAV photogrammetry provided dense mapping of the extrados surfaces, while terrestrial LiDAR captured the intrados geometry with millimetric accuracy.

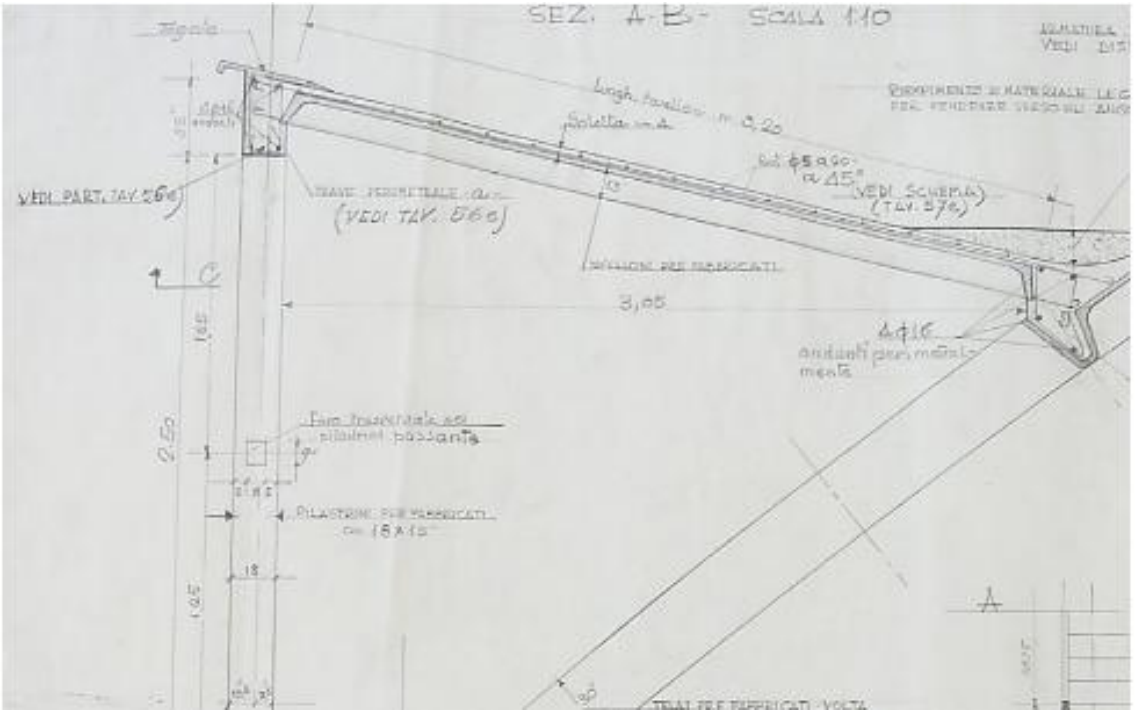

Figure 3.3 Historical drawings for hall C, from CSAC Archive, Parma

A unified topographic network ensured the co-registration of indoor and outdoor datasets, enabling consistent measurement of curvature, slab deformation, and element alignment. Deviation analyses performed on the NURBS reconstruction indicated discrepancies below 1 cm for over 90% of the measured points.

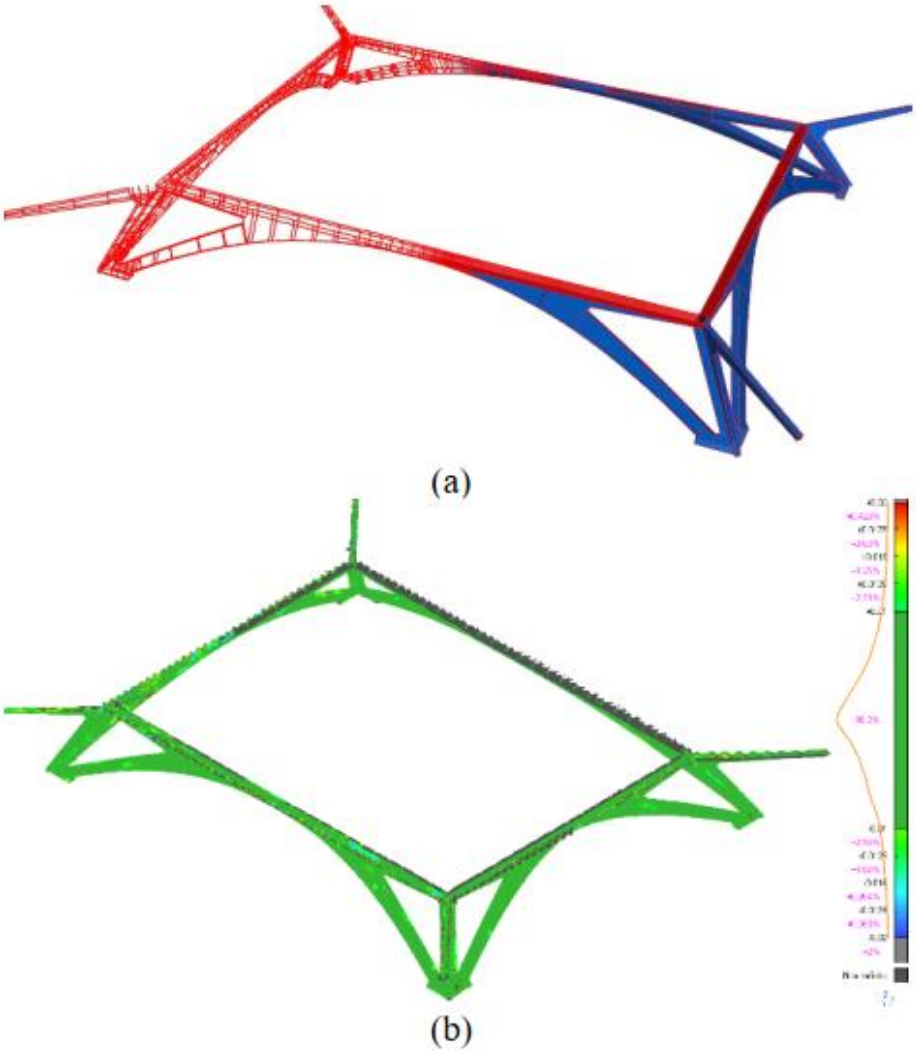

Figure 3.4 Deviation map comparing the NURBS model

Thickness measurements extracted from the integrated point clouds confirmed an average shell thickness of approximately 7.4 cm (including waterproofing), consistent with Nervi's intended 5 cm ferrocement. Survey observations further identified physiological cracking at the base of the arches and slight flouage deformation in the corrugated slabs—behaviors already predicted by the original static calculations.

Figure 3.5 Cracking pattern observed at the base of the inclined

These findings validated the accuracy of the archival drawings and provided essential ground truth for reproducing the geometry in the experimental mock-up.

3.3 Extraction of the Undulated Ferrocement Geometry for the Mock-Up

The experimental mock-up beam tested in this research replicates the geometry of a representative segment of the Hall C corrugated ferrocement slab. Its design was based on archival geometric profiles, LiDAR-derived sections, and measurements from multi-sensor survey campaigns. The undulated slab exhibits a wave profile with varying depth (0.26–0.44 m), increasing toward the arches where stiffness demands are higher. The reinforcement consists of three layers of steel mesh on both intrados and extrados.

Geometric scaling was not required, as the mock-up corresponds to a full-scale extraction of a single modular unit. This ensures realistic replication of bending stiffness, crack formation, and shear behavior. To ensure a realistic reproduction of the original slab behaviour, the mock-up was constructed at full scale (1:1), following the geometric and material evidence obtained from the survey campaigns. Based on the in-situ observations and archival documentation, appropriate reinforcement types were selected to replicate the mechanical logic of the historical ferrocement system.

In particular, non-ribbed S235 mild steel bars with a diameter of 5 mm were used for the transverse reinforcement, while S275 semi-hard steel bars with diameters of 10 mm and 12 mm were adopted for the longitudinal direction.

The mock-up has a total length of **6.3 m**, with a **variable cross-section height** consistent with the undulated profile of the original slab. The height gradually changes from approximately **27 cm at the edges** to **36 cm at midspan**, reaching a maximum of **40 cm** in the internal region where bending demands are higher.

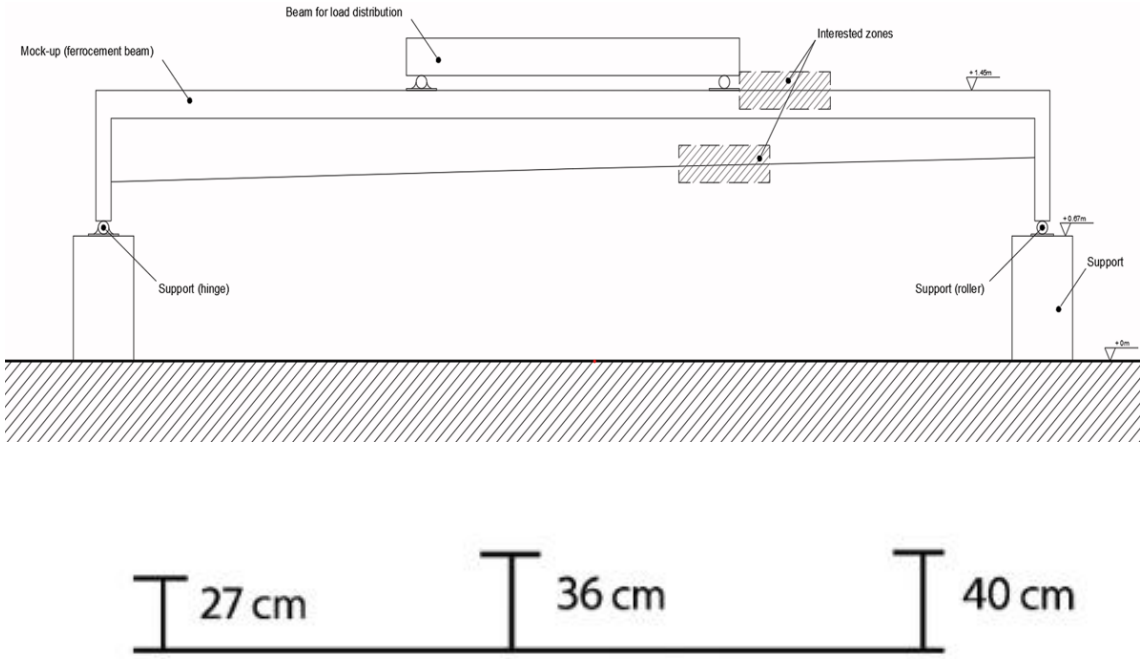

Figure 3.6 Schematic representation of the full-scale mock-up cross-section

The cross-sections adopted for the mock-up were derived from previous studies carried out within the research group for the development of formwork. These reconstructed sections reflect both the curved ferrocement profile and the thicker slab portion and were refined through digital geometric reconstruction to ensure compatibility with the measured data from Hall C.

The mock-up geometry directly derives from the measured corrugation wavelength and depth of Hall C, ensuring mechanical compatibility between the laboratory specimen and the original ferrocement slab.

4 EXPERIMENTAL RESULTS AND DISCUSSSION

This chapter outlines the experimental behavior of the undulated ferrocement beam subjected to a Four-Point Bending Test (FPBT). The findings are presented using plots generated through a data acquisition system and MATLAB post-processing scripts Where relevant, numerical dates from preliminary analyses are included to support the interpretation of results. The dataset consists of time in seconds, applied load in KN, midspan deflection in mm, displacement transducers along the span, and strain gauges on the top (compression) and bottom (tension) fibers. MATLAB scripts were used to generate a set of standardized figures.

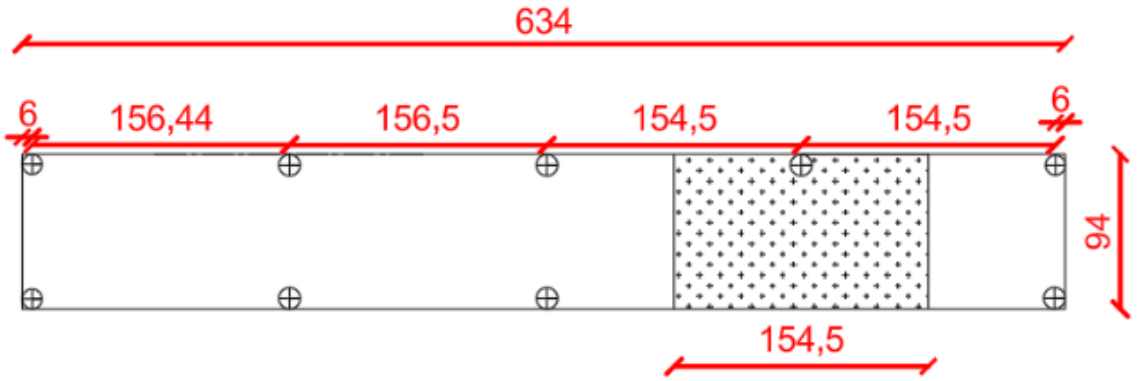

Figure 4.1 Displacement Transducers

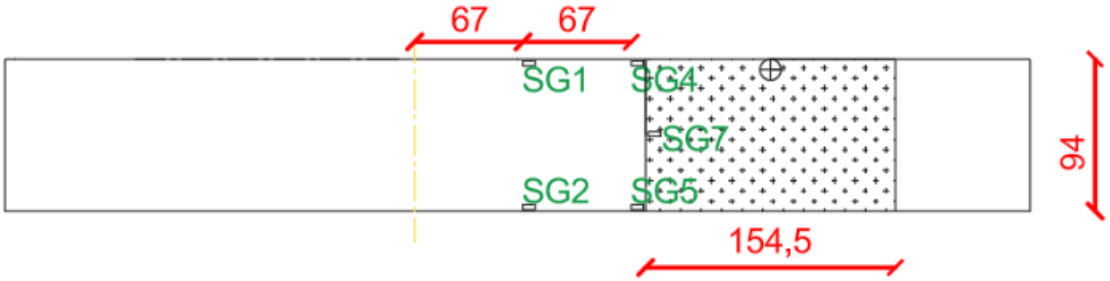

Figure 4.2 Strain Gauges

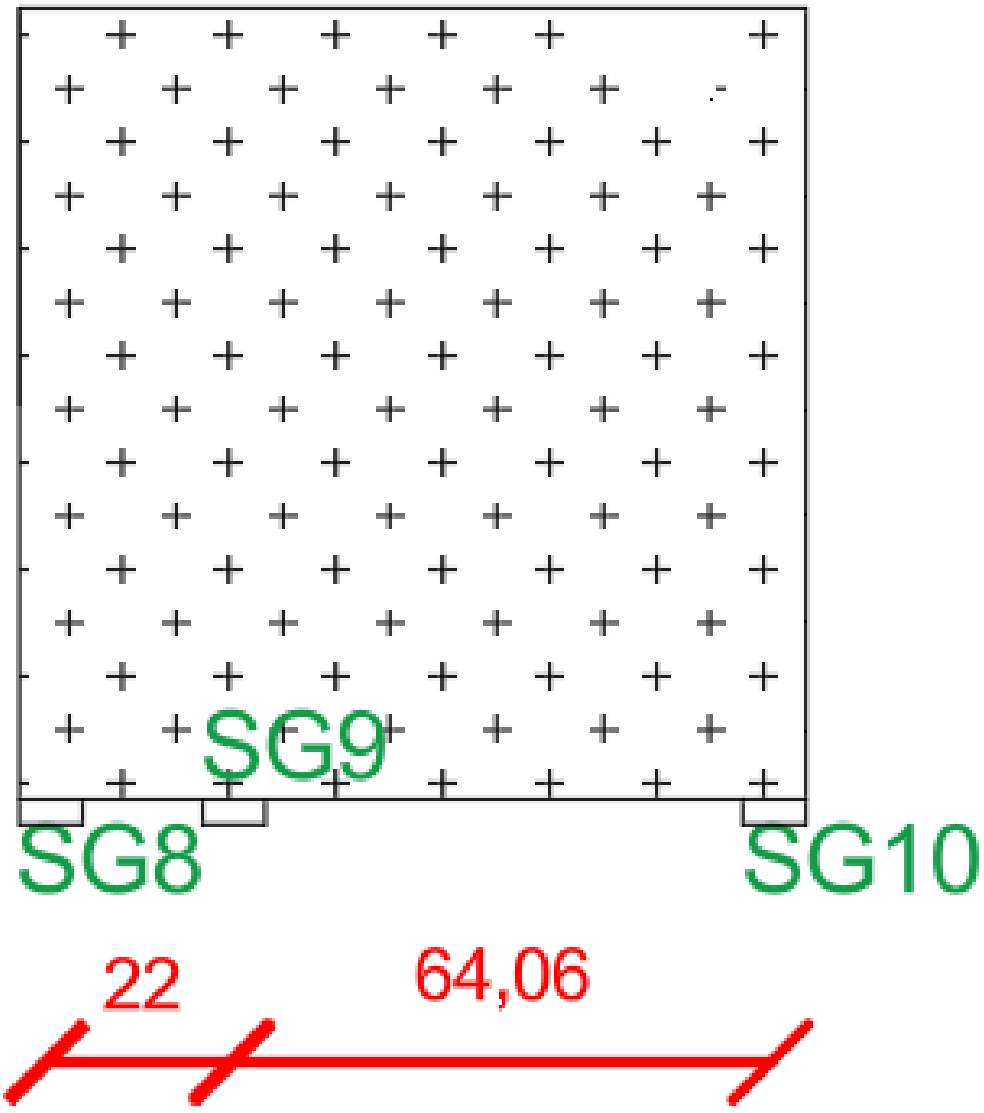

Figure 4.3 Area of DIC drawing

4.1 Ferrocement Analysis

Figure 4.4 ferrocement surface

4.1.1 Test Setup

The ferrocement beam was placed on its two steel supports. Displacement sensors were positioned at predefined points, and three cameras were installed too. capture the top, side, and bottom surfaces. The side and bottom surfaces were quickly prepared immediately before the test to ensure good contrast for image correlation.

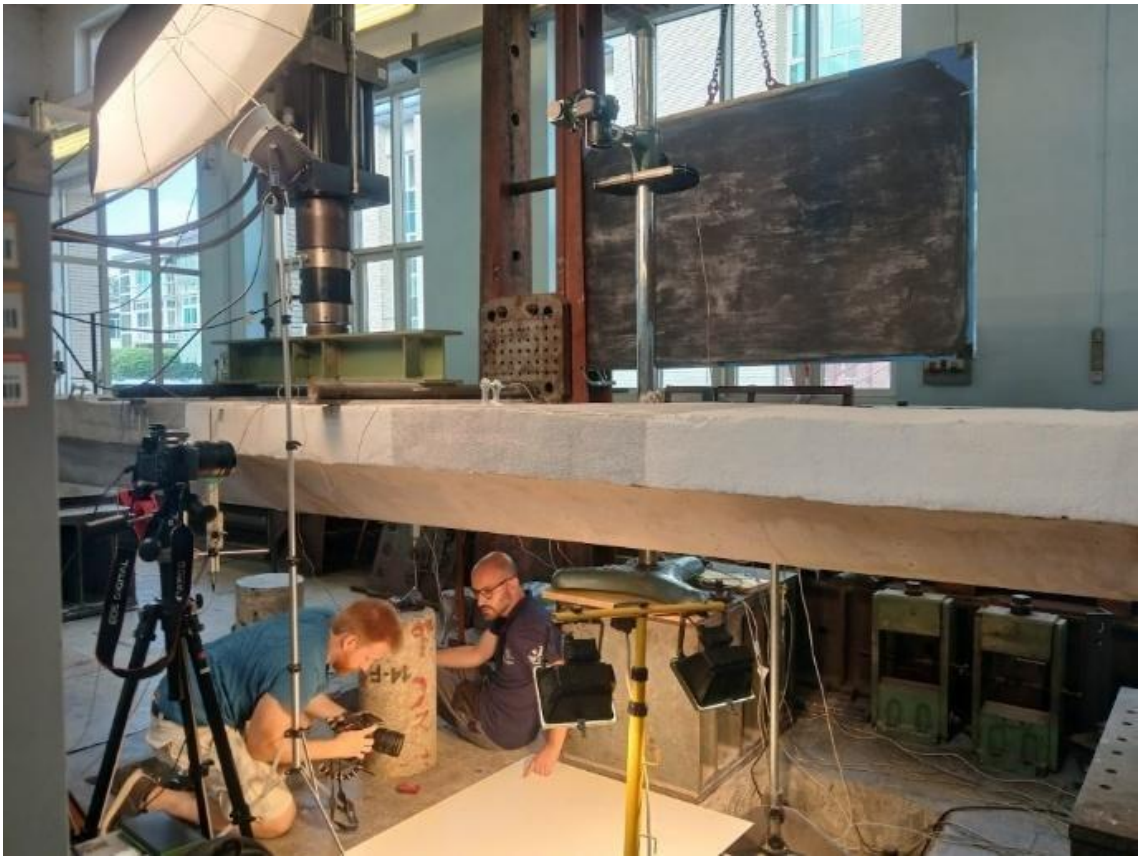

Figure 4.5 Beam preparation, test environment and installation of the camera prior to testing

The loading phase lasted approximately 2 hours and 20 minutes, during which roughly eight photographs per minute were taken. The maximum applied load reached 72 kN.

Camera settings were as follows:

- Top surface: aperture = f/11; ISO = 320; exposure = 1/15 s
- Side surface: aperture = f/11; ISO = 320; exposure = 1/20 s
- Bottom surface: aperture = f/13; ISO = 400; exposure = 1/20 s

Figure 4.6 setup of the beam

4.2 Matlab work

was used to develop a code that computes the deflection profile of a discretized beam for a FPBT subjected to an incremental load.

The MATLAB code follows the procedure outlined below:

1. Import the load-deflection behavior.
2. Define the load time response.
3. Compute the load strain relationship.
4. Extract the load displacement diagrams

4.3 Flexural Load–Deflection Response of Ferrocement Beam

This curve demonstrates the ductile nature of ferrocement. The load–deflection curve captures the typical nonlinear behavior of ferrocement beams under bending and can be interpreted across four key stages:

1. Initial Linear (Elastic) Phase – 0 to 20 mm Deflection (0–25 KN)

At the start of loading, the beam responds elastically. Both the mortar and mesh reinforcement work together as a unified material, with no visible cracking. The straight, steep portion of the curve represents the beam's initial stiffness and reflects full composite action.

2. Cracking and Stiffness Transition – 20 to 40 mm Deflection (25–70KN)

As the load increases, the curve begins to deviate from linearity. This marks the onset of cracking in the tension zone. Due to the thin section and the well-distributed mesh, numerous small cracks form gradually reducing stiffness. Despite this, the load continues to rise as the cracks stabilize and internal forces redistribute.

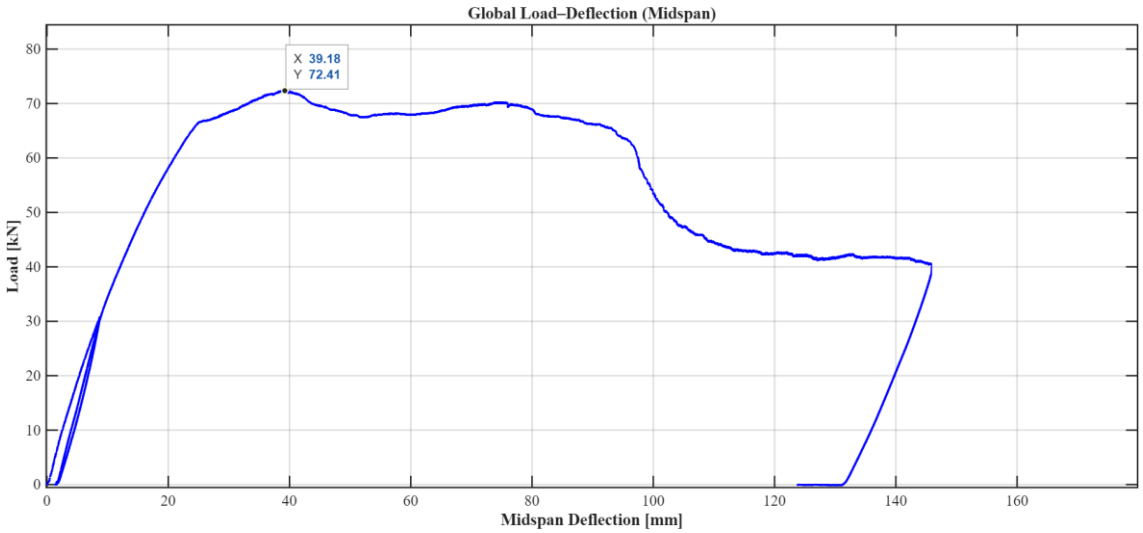

Figure 4.7 Global Load-Deflection response

3. Peak Load Stage – Around 72 KN at ~39 mm Deflection

This stage represents the beam's ultimate capacity. The mesh has now mobilized its full tensile strength, and yielding begins with the reinforcement. Simultaneously, the compression zone starts to experience localized crushing. The peak of the curve signifies the balance point before the structure begins to soften.

4. Post-Peak Softening and Failure – Beyond 40 mm Deflection

After the peak, the load gradually decreases as damage accumulates. This softening behavior is linked to continued cracking, pullout of the mesh reinforcement, and loss of stiffness. The gentle slope shows that the beam absorbs a significant amount of energy before collapse. Eventually, beyond ~130 mm of deflection, a sharper drop in load indicates structural failure—likely due to mesh rupture or extensive mortar crushing near the load points.

4.4 Load–Time Response

This load history represents a controlled incremental loading phase, where small pauses correspond to either data acquisition or load stabilization intervals.

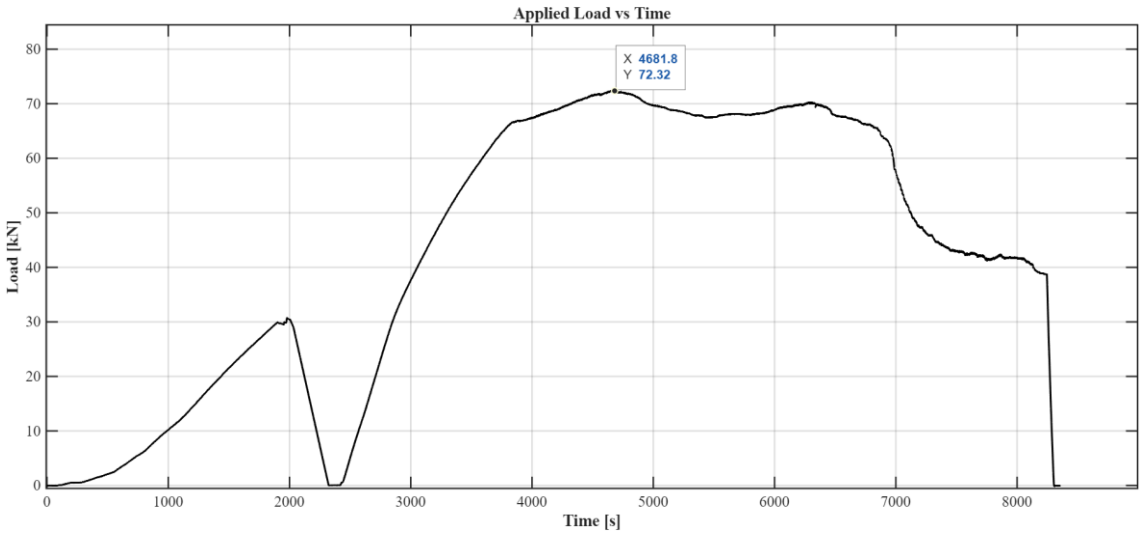

Figure 4.8 Applied load as a function of time

1. Initial Phase (0–2000 s | 0–30 KN): A small peak around 30 KN likely indicates a preliminary loading-unloading cycle for system calibration. This is typical in experimental setups to check seating and instrumentation before full testing. The brief pauses seen in the curve likely reflect data acquisition intervals.
2. Main Loading Phase (2000–6000 s | 30–72 KN): The load gradually increases as the beam progresses from uncracked elasticity into cracking and redistribution phases. The beam reaches its peak load (~72 kN) during this stage, consistent with the load–deflection curve and confirming synchronized system performance.
3. Softening and Failure Phase (6000–8500 s): After the peak, the load gently declines as damage accumulates—including crack widening, mesh pullout, and mortar degradation. The smooth descent indicates progressive failure, not collapse, highlighting the ductile nature of the ferrocement system.

4.5 Load–Strain Relationship (strain Gauges)

This section presents how the strain in the ferrocement beam developed in response to increasing load, as measured by strain gauges placed along the top (compression) and bottom (tension). This pattern reflects the typical flexural behavior of beams: tension develops at the bottom due to bending,

while compression builds up at the top. As loading progressed, the data clearly showed a shift from the initial elastic phase to the cracked phase, where the strain behavior becomes nonlinear due to crack formation and redistribution of stresses.

To better understand the structural response, strain gauges were grouped and plotted together—for example, SG3, SG6, SG8–SG10, and SG7 (designated as Groups 5–7). These combined plots provided a clearer view of how the neutral axis moved upward as tension cracks formed and the load increased. The consistent trends observed across these gauge groups confirm that the strain distribution remained compatible and symmetrical, supporting the assumption of well-distributed flexural response.

4.5.1 Load–Strain Relationship – Top Gauges (Compression)

The load–strain curves obtained from the top compression strain gauges (SG_1, SG_2, SG_4, and SG_5) provide valuable insight into the compressive behavior of the ferrocement beam under four-point flexural loading.

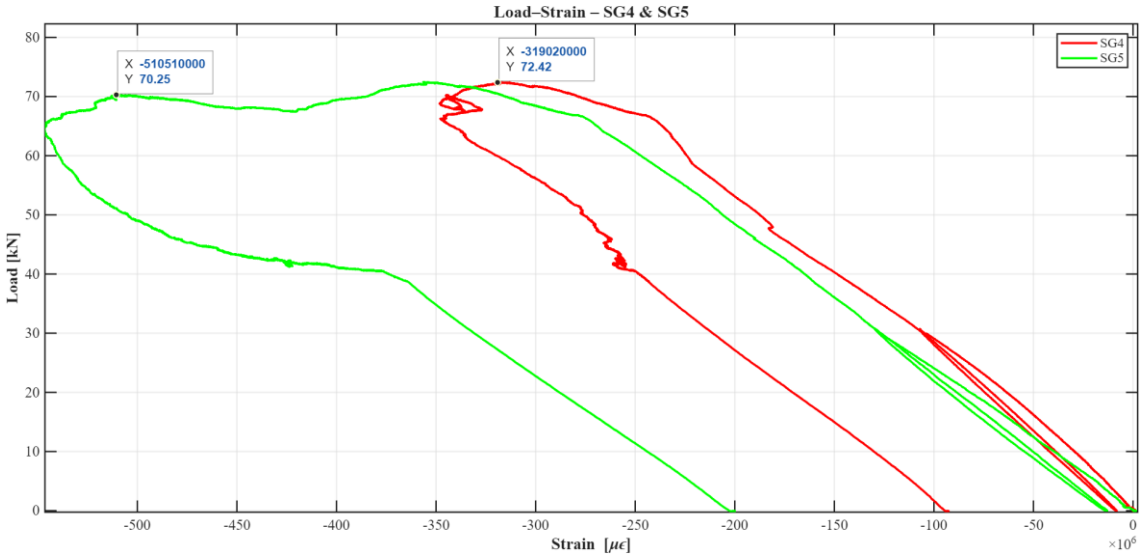

Figure 4.9 Load–strain relationship of top compression gauges

These measurements reflect how the mortar and embedded mesh respond together under increasing compressive stress and help confirm the beam's ductile performance. Phases of Compressive Strain Behavior.

1. Elastic Phase (0–25/30 KN)

At the initial stage of loading, all top gauges recorded a linear increase in compressive strain with applied load. This confirms that the beam was still in its uncracked, elastic phase, with the mortar matrix and steel mesh acting as a composite system. Gauges SG_1 and SG_2 showed closely

matched responses, indicating a uniform stress distribution across the compression face. Strain values remained well below failure thresholds, consistent with undamaged behavior.

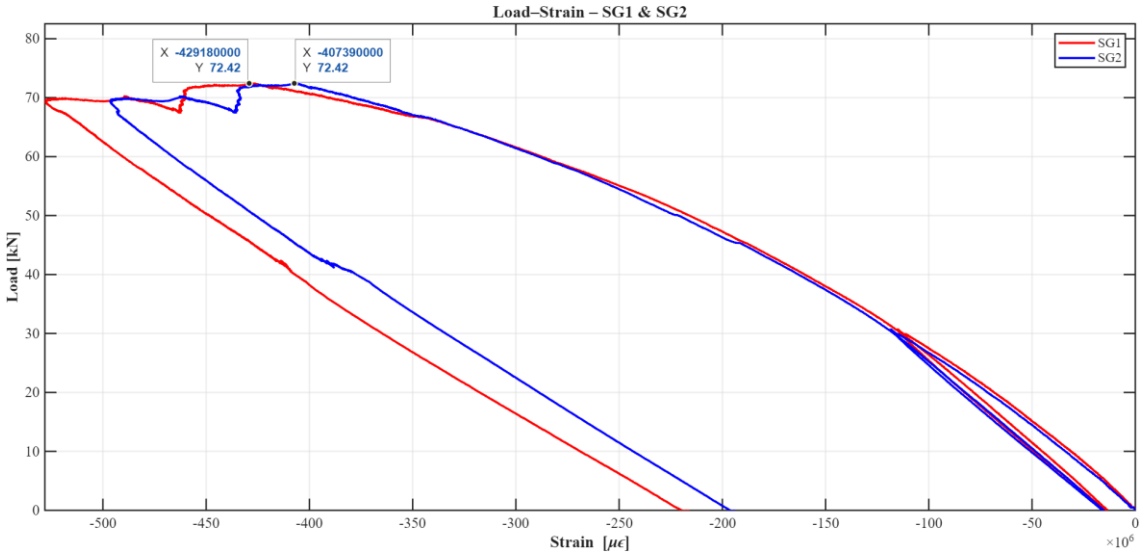

Figure 4.10 Load–strain relationship 5

2. Cracking and Transition to Nonlinearity

As the load increased beyond 30 KN, the curves gradually deviated from linearity, marking the onset of cracking in the tension zone and a shift in the neutral axis upward. This led to stress concentration in the upper compression region. Among all gauges, SG_4 recorded the highest compressive strain (–515 με), likely due to its proximity to a high-stress region near the load application point. SG_1 and SG_2 followed with values around –430 με, while SG_5 showed a slightly lower peak (–318 με), possibly due to local variation or gauge placement.

3. Peak Load Stage (~72 kN)

At peak load, all compression strain gauges approached their maximum strain levels. Though still below the typical mortar crushing strain (~–3000 με), these values indicate that the compressive capacity of the section was mobilized. The strain remained concentrated in the upper fibers, supporting the flexural failure mode rather than shear.

4. Post-Peak Softening and Residual Strain

Following peak load, although the applied load started to drop, the compressive strains continued to increase, indicating ongoing mortar crushing and stiffness degradation in the compression zone. After unloading, all gauges retained residual compressive strains (~–150 με), confirming permanent deformation due to plastic damage—a clear sign of ductile behavior.

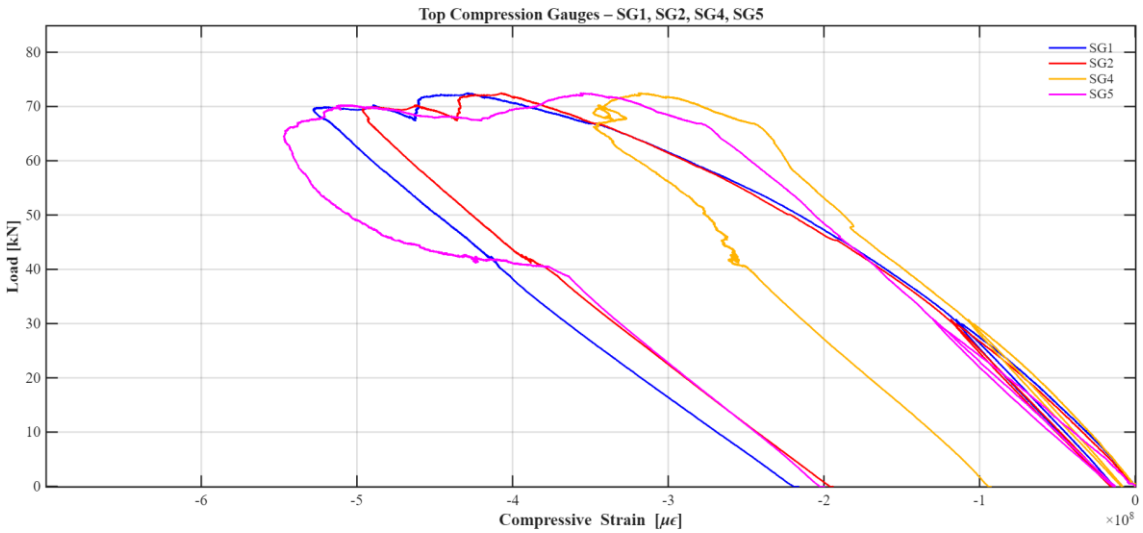

Figure 4.11 Top compression Gauges

4.5.2 Load–Strain Relationship – Bottom (tension) Gauges

The load–strain curves recorded from the bottom strain gauges (SG_3, SG_6, SG_8, SG_9, and SG_{10}) provide a detailed understanding of the tensile behavior of the ferrocement beam during four-point bending. These gauges captured how the tension zone evolved from elastic behavior through crack initiation to post-peak deformation, which is essential for evaluating ductility and crack control. Stages of Tensile Load–Strain Behavior.

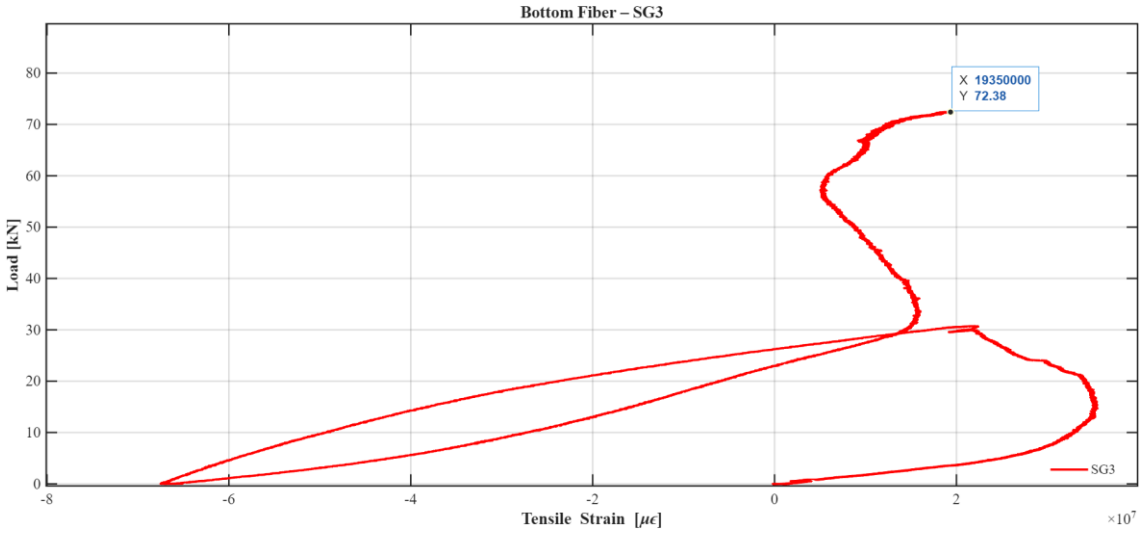

Figure 4.12Bottom partSG3

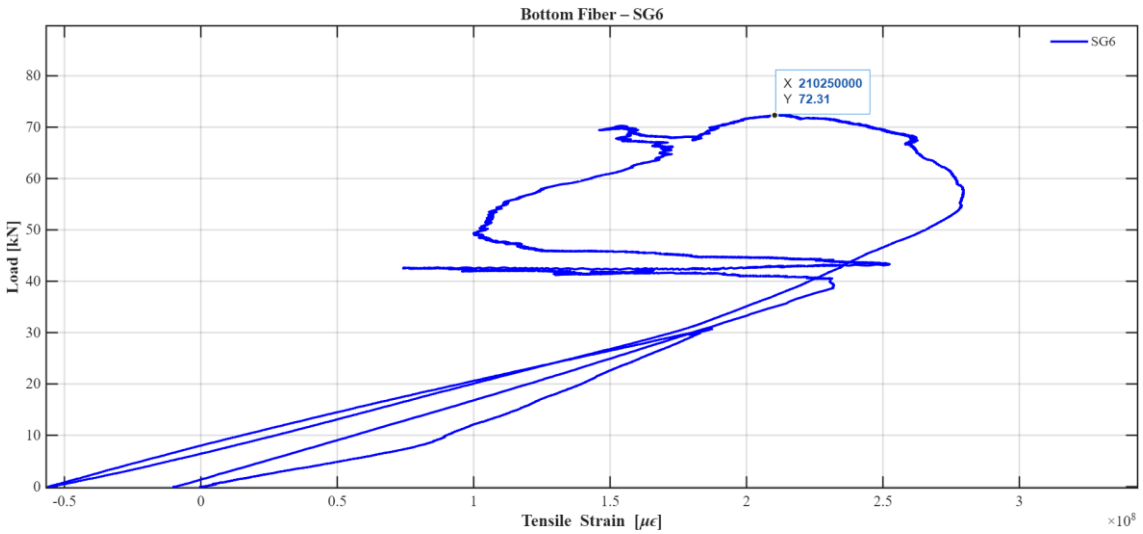

Figure 4.13 Bottom part SG6

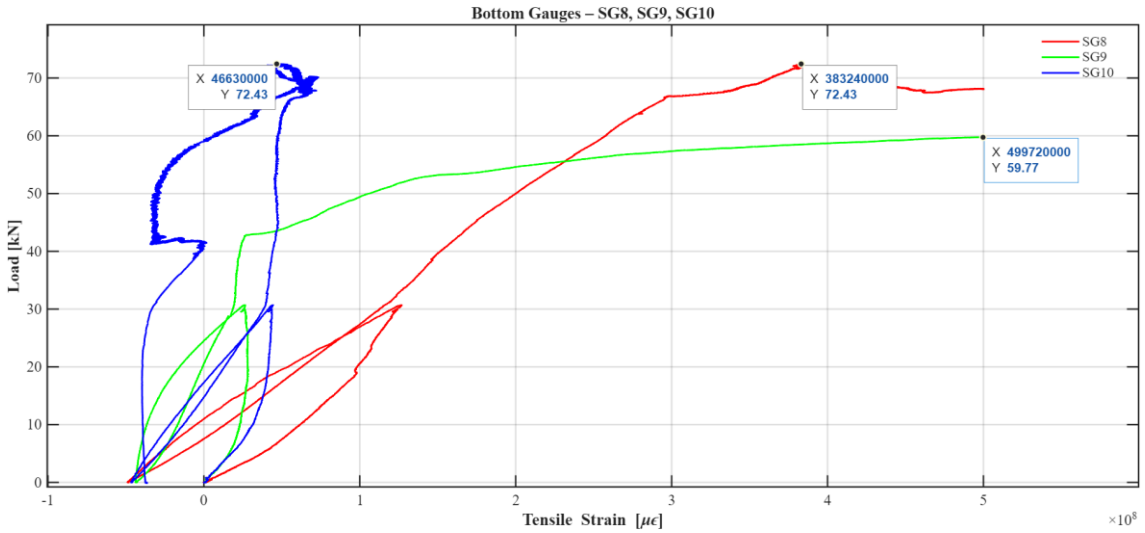

Figure 4.14 Comparative load–strain curves for bottom

4.6 Strain Analysis in the Digital Image Correlation (DIC) zone

To gain a deeper understanding of the local strain behavior in the ferrocement beam, a critical DIC zone was instrumented near one of the loading points. This area was equipped with both top (compressive) strain gauges SG_4, SG_5, SG_7 and bottom (tensile) strain gauges SG_8, SG_9, SG_{10} allowing for detailed monitoring of the flexural strain gradient across the beam's depth.

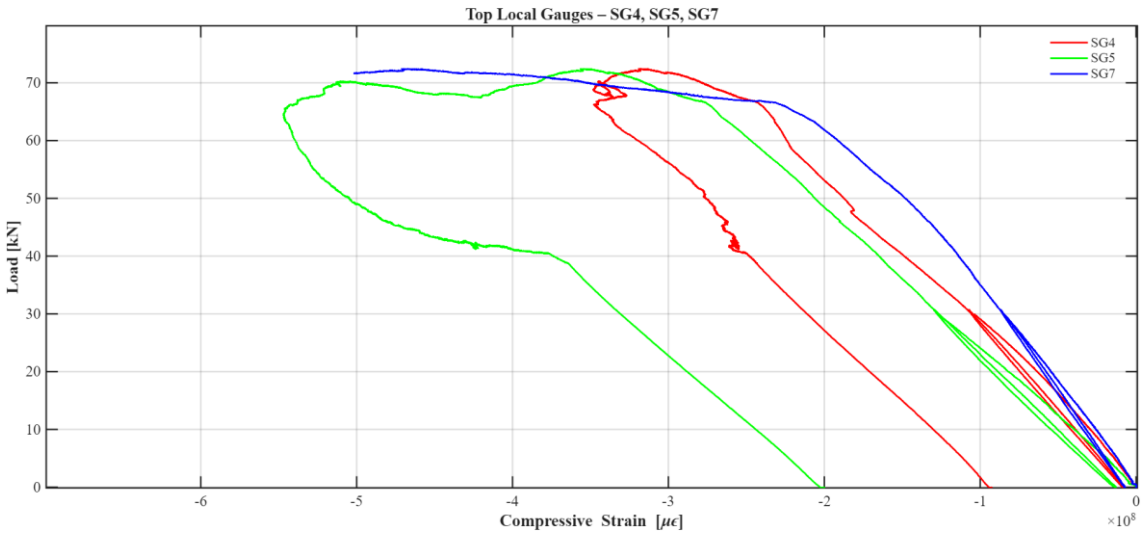

Figure 4.15 Comparative load–strain curves

DIC Correlation and Validation:

- SG_7 (compression) and SG_8 (tension), positioned centrally within the DIC zone, offer key reference points for validating full-field strain data obtained via DIC imaging.
- The strain magnitudes and post-peak residuals serve as calibration markers for DIC-derived outputs such as:

1. Crack width estimation
2. Localized deformation fields
3. Neutral axis tracking

These strain gauge readings are essential for correlating true physical behavior with DIC visual output, especially in confirming crack initiation sites and damage zones.

4.7 Deflection Analysis Using Displacement Transducers (LVDTs)

To assess the flexural behavior of the ferrocement beam under loading, Linear Variable Displacement Transducers (LVDTs) were strategically placed across the span and support zones. These sensors provided accurate, real-time measurements of beam deflection, helping to monitor stiffness, symmetry, and failure progression.

Sensor Placement Summary:

- SP-SX-1/2 = Left span points (midspan quarter-points)
- supp-sx-1/2 = Left support points

- FR1, FR2 = Midspan or DIC-adjacent displacement sensors
- SP-DX-1 = Right span point (DIC-adjacent)
- SUPP-DX-1/2 = Right support points (near DIC)

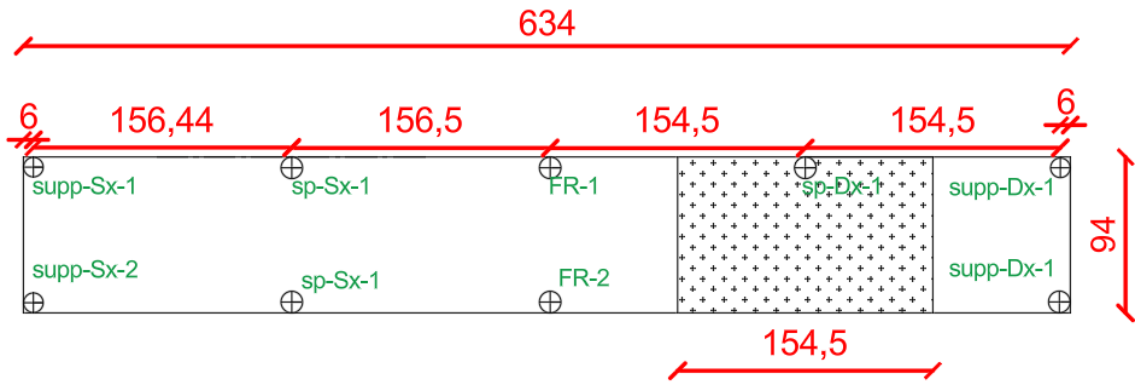

Figure 4.16 Displacement Transducers drawing

1. Elastic Stage (Load ≤ 25–30 kN): All curves from support and span-point LVDTs (in all graphs) show linear behavior. The load-deflection slope is steep, indicating high initial stiffness and undamaged ferrocement composite action. The beam is uncracked, and both mortar and steel mesh act compositely. No significant differences are observed between left (SX) and right (DX) sides at this stage, meaning the structure is responding symmetrically under bending.

Cracking & Peak Load (~30–72 kN): Left Side Analysis (SP-SX-1/2, supp-sx-1/2), Both SP-SX-1 and SP-SX-2 reach deflections of 22 mm at 72.4 kN. The near-perfect overlap indicates symmetric cracking and deformation in the left span zone. From "Load–Deflection: supp-sx-1 & supp-sx-2": Supp-sx-1 shows very limited deflection (0.4 mm), Supp-sx-2 shows much higher support movement (1.7 mm) at peak load, Slight asymmetry at support level hints at rotation or slippage under increasing load, potentially influenced by local boundary conditions. Nevertheless, span-point data confirms stable and symmetric flexural response on the left side before failure.

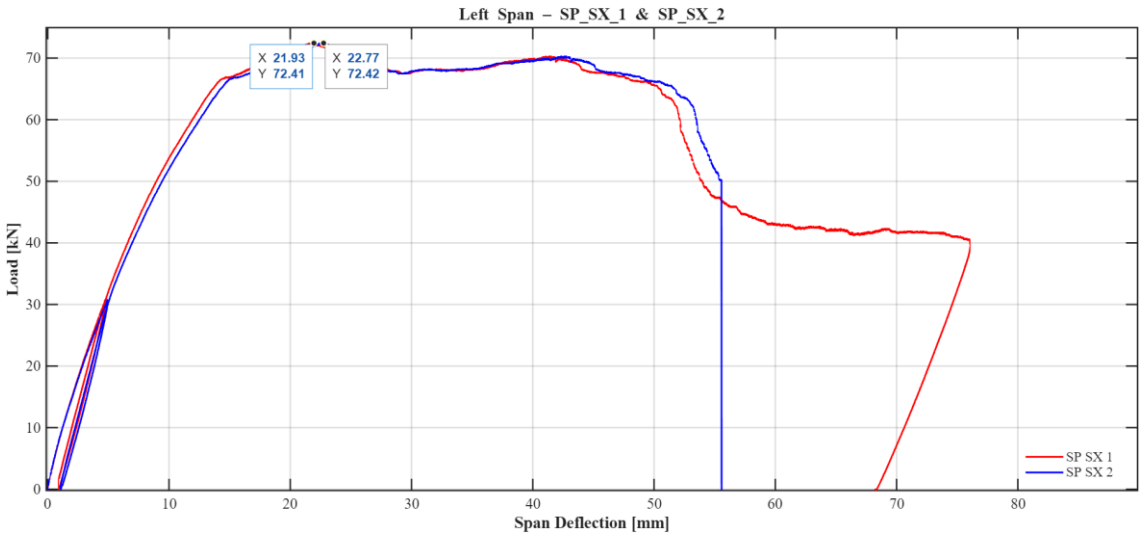

Figure 4.17 load deflection on right side

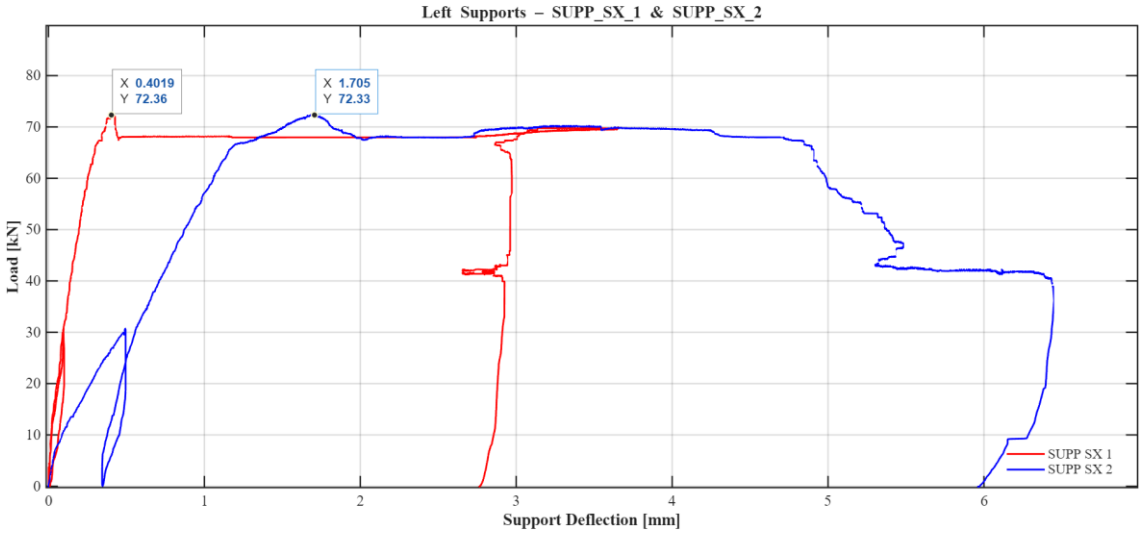

Figure 4.18 load deflection of supports on right side

- Right Side Analysis (FR1, FR2, SP-DX-1, SUPP-DX-1/2): From Load–Deflection: FR1, FR2 & SP DX 1: FR1 and FR2 show peak deflections of 36.7 mm, with SP-DX-1 35.6 mm, very close agreement confirms accurate strain and displacement readings in the DIC zone.

- From Load–Deflection: SP DX 1, SUPP DX 1 & SUPP DX 2: SP-DX-1 reaches 31.3 mm deflection at 72.4 KN., Both SUPP-DX-1 and SUPP-DX-2 show very small movements (<1.2 mm).

1. Post-Peak & Failure (Load > 72 KN) Left Side: From SP-SX-1/2, the deflection curve shows softening after peak load and reaches 50–72 mm, suggesting ductile response and distributed cracking., Sudden drop in SP-SX-2 indicates potential localized failure or

measurement cutoff. After the peak, the displacement at supp-sx-1 levels off, while supp-sx-2 continues to increase up to about 3 mm. This behavior indicates the onset of rotation or a slight uplift at support.

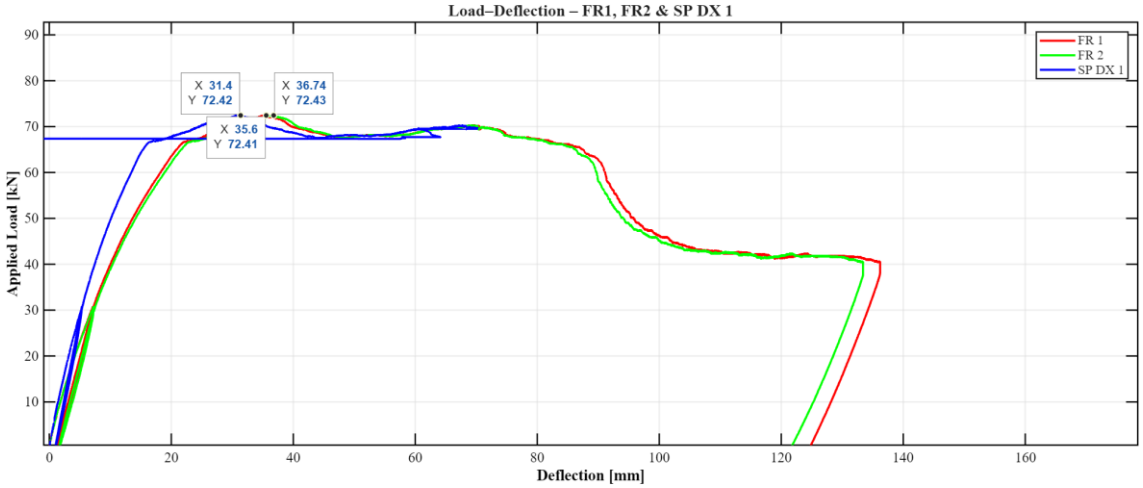

Figure 4.19 load-deflection supports on right side

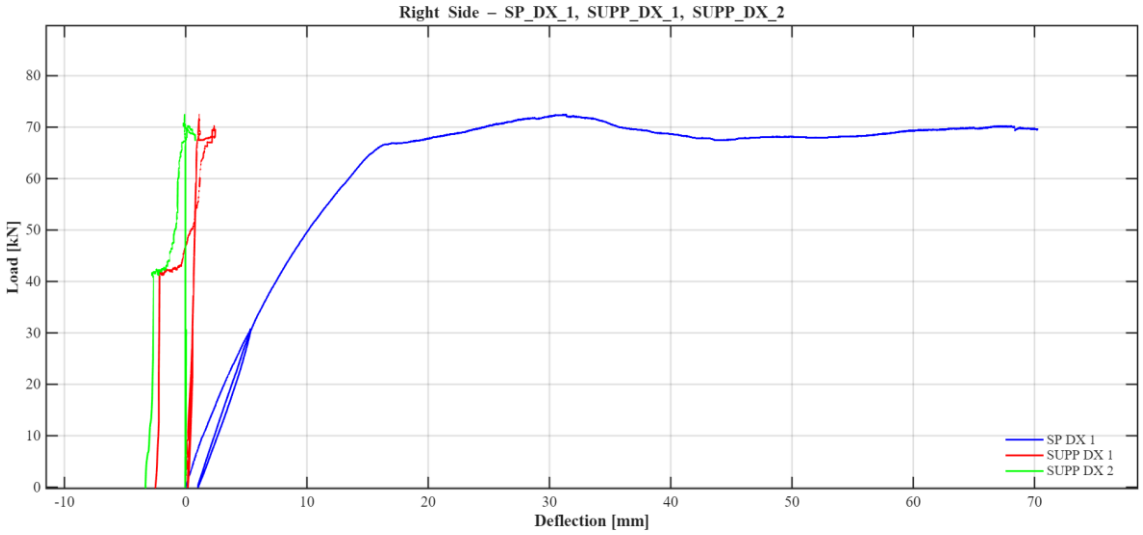

Figure 4.20 load Deflection right side

Use FR1, FR2, SP-DX-1 as core data sources for correlating with DIC full-field deformation. Highlight that support deflection asymmetry (especially on left side) suggests influence of test setup but did not compromise symmetry of main flexural response. Emphasize that the deflection curves validate pseudo-ductile behavior typical of ferrocement systems ideal for lightweight, crack-resistant structural elements.

4.8 Macroscopic Observations

During loading, several visible deformations appeared. Initially, both supports slid slightly,

allowing limited movement of the beam. As the load increased, the beam gradually bent into two distinct straight segments, forming a clear curvature profile. Near failure, a diagonal rupture plane (45°) developed, visible along the speckled zones on both sides and on the underside.

Figure 4.21 Left, sliding of the beam on supports, Right deformation at the end of the test.

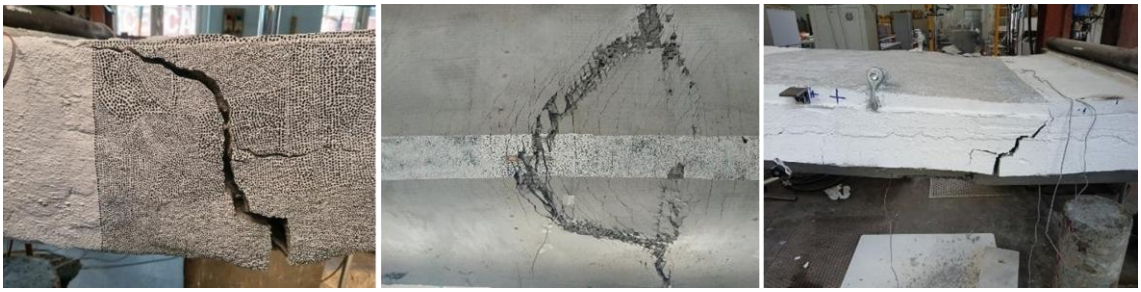

Figure 4.22 Appearance of the plane rupture

5 DIGITAL IMAGE CORRELATION

Digital Image Correlation (DIC) represents a modern optical technique for measuring surface displacements and strain fields in materials subjected to mechanical loading. It operates by acquiring a sequence of high-resolution images of a specimen before and after the application of stress, then tracking the relative movement of the surface pattern through image-processing algorithms. This full-field, non-contact approach enables accurate quantification of deformations under various loading conditions while avoiding interference with the specimen's behavior.

Unlike traditional point-based sensors, DIC can capture complex geometries and heterogeneous strain distributions with sub-pixel precision. Its flexibility makes it an indispensable tool across several disciplines, from experimental mechanics and structural monitoring to aerospace, biomedical and civil-engineering applications. The continual evolution of imaging systems, optical calibration procedures and correlation algorithms has significantly increased both its accuracy and accessibility, transforming DIC into a benchmark method for deformation monitoring in laboratory and field investigations. The following chapter is structured to provide a clear understanding of the technique and its experimental implementation. It includes:

1. An explanation of the optical parameters that must be defined to obtain reliable DIC measurements.
2. A detailed discussion of the main principles and characteristics of the DIC process.
3. An introduction to VIC-2D and NCORR, the two correlation programs used in this research for the analysis of preliminary and advanced tests.

Subsequent sections will describe the development of the experimental DIC setup for the four-point bending test on a ferrocement beam, outlining the calibration, image-acquisition strategy, and system configuration derived from the preliminary VIC-2D campaigns and later optimized for NCORR analysis.

In this research, two DIC platforms were employed:

1. VIC-2D (commercial, user-friendly, fast)
2. NCORR (open-source, transparent, research-oriented)

Both were applied to validate the optical setup, first through a preliminary compression test on a

150 ×150 mm concrete cube, and then through a full-scale four-point bending test on a ferrocement beam. The results from both software environments allowed cross-verification of strain evolution, displacement patterns, and crack formation.

5.1 Optical Properties

Successful Digital Image Correlation (DIC) analysis depends fundamentally on the optical configuration of the image-acquisition system. Every parameter of the camera–lens setup influences the quality of the captured images and, consequently, the accuracy of the computed strain field. The optical system must ensure uniform illumination, precise focusing, and minimal image distortion, allowing the speckle pattern to be recorded with high contrast and stability throughout the entire test.

5.1.1 Focal length

The focal length, f˜, controls the scale of magnification and determines the working distance between the lens and the specimen. Longer focal lengths provide higher spatial resolution but reduce the field of view and depth of field. For the Nikon D90 and Nikon D800 cameras used in the preliminary tests, focal lengths between 35 mm and 85 mm were evaluated. An 85 mm setting was ultimately adopted to maximize pixel density over the measurement area, corresponding to approximately 30 cm camera-to-surface distance. This configuration provided a balance between image sharpness, field coverage, and manageable perspective distortion. An 85 mm setting was ultimately adopted to maximize pixel density over the measurement area, corresponding to approximately 30 cm camera-to-surface distance. This configuration provided a balance between image sharpness, field coverage, and manageable perspective distortion.

5.1.2 Circle of Confusion of the circle

The circle of confusion defines the smallest distinguishable blur that can be resolved by the sensor. Maintaining a small circle of confusion (≈ 0.02 mm for the selected cameras) ensured that the individual speckles remained optically separated even when the surface experienced minor out-of-plane displacements. Fine focusing and rigid camera support were essential to keep this parameter constant during long-duration loading stages.

5.1.3 Aperture (Diaphragm)

The aperture directly influences both the exposure and the depth of field. Moderate aperture values between f/8 and f/11 were selected to achieve a sufficient depth of field while preventing

diffraction effects. This setting maintained a uniform sharpness across the speckled area and minimized the need for post-processing filters.

A small aperture brings out the dust on the sensor. Almost all cameras, even those with a freshly cleaned sensor, show dust spots. A too large aperture, on the other hand, creates pronounced aberrations (chromatic aberrations and vignetting). For these reasons, recommends using a medium aperture between f/5.6 and f/11.

5.1.4 Exposure time

Because mechanical loading introduces minor vibrations, short exposure times were required to eliminate motion blur. Typical shutter speeds ranged from 1/125 s to 1/250 s, providing clear, stable images even under incremental load application. The exposures were triggered remotely via the Digicam Control software to avoid manual disturbance.

5.1.5 ISO sensitivity

ISO sensitivity determines the sensor's response to light. Values between ISO 200 and 400 were found to be optimal, providing adequate brightness while maintaining a low noise floor. Higher ISO levels were avoided to prevent pixel noise that could reduce correlation quality, particularly in the darker zones of the speckle pattern.

5.1.6 Hyperfocal distance

The hyperfocal distance represents the closest focusing distance at which the entire region of interest (ROI) remains acceptably sharp. It was calculated according to the selected focal length and aperture, ensuring that both the specimen's front and rear edges of the ROI were in focus. Adjustments were verified through test captures before each experiment.

5.1.7 Angle of view

The "angles of view (α)" are the angles that relate the dimensions of the sensor to the FOV. depends on the sensor dimensions and the chosen focal length. With the Nikon D800's full frame sensor (24×36 mm) and an 85 mm focal length, the resulting horizontal view angle was approximately 23 degrees, covering the complete face of the concrete cube or the central span of the test beam.

5.1.8 Field of View (FOV)

The field of view defines the physical area captured by the camera at a given distance. In the preliminary tests, the FOV ranged from 150 mm × 150 mm for cube specimens to 400 mm × 250 mm for the steel plate and beam sections. A calibration grid with known dimensions was photographed before each test to convert pixel displacements into real world units (mm/pixel).

5.1.9 Depth of Field (DOF)

Depth of Field (DOF) indicates the thickness of the region that remains in focus. To avoid errors from surface unevenness, a DOF between 15 and 25 mm was maintained. This was achieved by adjusting aperture and focus position in combination with the hyperfocal distance calculation. Stable illumination and rigid tripod mounting further ensured that the DOF remained constant for all loading steps.

5.2 Digital Image Correlation Process

Digital Image Correlation (DIC) is a full-field, non-contact optical technique that quantifies surface displacements and strains by analyzing a sequence of digital images taken during mechanical loading. The method relies on tracking a random speckle pattern applied to the specimen. By comparing an undeformed reference image with successive deformed images, DIC reconstructs the motion of the surface with sub-pixel precision, allowing accurate evaluation of deformation, crack initiation and strain localization across the entire region of interest. This process has become widely adopted in recent years due to its flexibility, high spatial resolution, and suitability for both laboratory and field applications.

5.2.1 Subset Definition and Correlation Principal size

In 2D DIC, each image is divided into small square patches known as subsets or facets, each containing a unique distribution of grey-level intensities generated by the speckle pattern. During deformation, each subset undergoes translation, rotation and distortion. The correlation algorithm searches the deformed image to locate the subset position that best matches its reference configuration. For accurate tracking, subsets must contain multiple speckles to provide sufficient texture. Typical subset radii range from 20–30 pixels, balancing spatial resolution and numerical stability.

5.2.2 Subset Spacing and Grid Resolution

Subset spacing defines the distance between neighboring subset centers and therefore controls the density of the measurement grid.

1. Smaller spacing → higher spatial resolution, increased computational time
2. Larger spacing → smoother strain fields, reduced noise sensitivity

Selecting appropriate spacing ensures that deformation gradients can be captured while maintaining efficient computation. In the VIC-2D analyses, a spacing of 5 pixels achieved a good balance, providing smooth strain fields without excessive processing time.

5.2.3 Correlation Criteria and Matching Accuracy

The similarity between a subset in the reference image and its candidate in the deformed image is quantified through a correlation criterion. Modern DIC practice typically adopts illumination-insensitive criteria to ensure stable matching under fluctuating brightness or uneven lighting.

Common formulations include:

- SSD – Sum of Squared Differences
- ZSSD – Zero-mean SSD
- NSSD – Normalized SSD
- ZNSSD – Zero-mean Normalized SSD (most robust)

A general expression for the zero-mean normalised correlation is:

$$C = \sum_{(x,y)} \left[\frac{I_r(x,y) - \bar{I}_r}{\sigma_r} - \frac{I_d(x+u, y+v) - \bar{I}_d}{\sigma_d} \right]^2$$

where:

- I_r= grey levels in reference image
- I_d= grey levels in deformed image
- $\bar{I}$, σ= mean and standard deviation
- u, v= displacement components of the subset

Sub-pixel precision—often better than 0.01 pixels—is achieved by interpolating grey levels using bicubic or spline interpolation.

5.2.4 Shape Functions and Local Deformation Mapping

To reconstruct how each subset deforms, DIC uses shape functions that describe the variation of displacement within the subset. For most quasi-static structural applications, a first-order affine shape function is sufficient:

$$u(x,y) = u_0 + u_x \Delta x + u_y \Delta y$$

$$v(x,y) = v_0 + v_x \Delta x + v_y \Delta y$$

where:

- $\boldsymbol{u_0}, \boldsymbol{v_0}$= rigid translation of the subset
- $\boldsymbol{u_x}, \boldsymbol{u_y}, \boldsymbol{v_x}, \boldsymbol{v_y}$= displacement gradients
- $\boldsymbol{\Delta x}, \boldsymbol{\Delta y}$= pixel coordinates relative to the subset centre

Higher-order functions may be used for large or complex deformations but significantly increase computational effort.

5.2.5 Strain Computation

Once displacement fields are obtained, strains are derived from the spatial gradients of the displacement components. For small to moderately large deformations, the Green Lagrange strain tensor is commonly used:

$$E_{xx} = \frac{1}{2}\left(2\frac{\partial u}{\partial x} + \left(\frac{\partial u}{\partial x}\right)^2 + \left(\frac{\partial v}{\partial x}\right)^2\right)$$

$$E_{yy} = \frac{1}{2}\left(2\frac{\partial v}{\partial y} + \left(\frac{\partial u}{\partial y}\right)^2 + \left(\frac{\partial v}{\partial y}\right)^2\right)$$

$$E_{xy} = \frac{1}{2}\left(\frac{\partial u}{\partial y} + \frac{\partial v}{\partial x} + \frac{\partial u}{\partial y}\frac{\partial v}{\partial x}\right)$$

Because numerical differentiation amplifies noise, strain fields are usually smoothed using filters such as Gaussian kernels or least-squares strain windows.

5.2.6 Error Sources and Mitigation

DIC accuracy depends strongly on image quality, optical stability and surface preparation. Typical error sources include:

- Illumination variations

- Camera vibration or specimen movement
- Lens distortion
- Low speckle contrast or poor texture
- Out-of-plane movements
- Perspective distortions

Mitigation measures include rigid camera support, controlled lighting, calibration grids, high-quality speckle patterns, and minimizing out-of-plane motion.

5.2.7 Out-of-Plane Motion and Correlation Loss

2D DIC assumes that deformation occurs in-planes. If out-of-plane displacement occurs, the apparent subset pattern changes due to perspective shifts or defocusing. This leads to a local drop in the correlation coefficient. A coefficient correlation threshold of 0.85 is often used to identify frames or regions affected by significant decorrelation.

6 DIGITAL IMAGE PRELIMINARY COMPRESSION TEST ON CONCRETE CUBE WITH VIC-2D

6.1 Purpose of the Preliminary Test

Before performing the main four-point bending experiment on the ferrocement beam, a preliminary DIC validation test was carried out on a small 150 × 150 mm concrete cube.

*Figure 6.1cube 150*150 cm*

The primary goal of these tests was to determine the optical camera configuration to:

- Maximize image contrast and clarity.
- Minimize image noise.
- Achieve precise sub-pixel displacement tracking in DIC analysis.
- Observe micro-deformations during the early stages of loading
- evaluate the performance of different speckle-pattern techniques,
- optimize the VIC-2D correlation parameters (subset, spacing, strain radius, exposure

settings, etc.).

This initial phase allowed the team to calibrate the entire workflow from image capture to strain computation under controlled loading conditions before applying it to the full-scale ferrocement beam.

Figure 6.2: laboratory of politecnico di Torino

6.1.1 Specimen Preparation and Pattern Application

Before testing, the surface of the 150 × 150 mm concrete cube was carefully cleaned and polished to remove dust, laitance, and any loose particles that could interfere with paint adhesion or image contrast. A thin white base coat was then applied to create a uniform, non-reflective background, ensuring optimal visibility for the speckle pattern during DIC image acquisition.

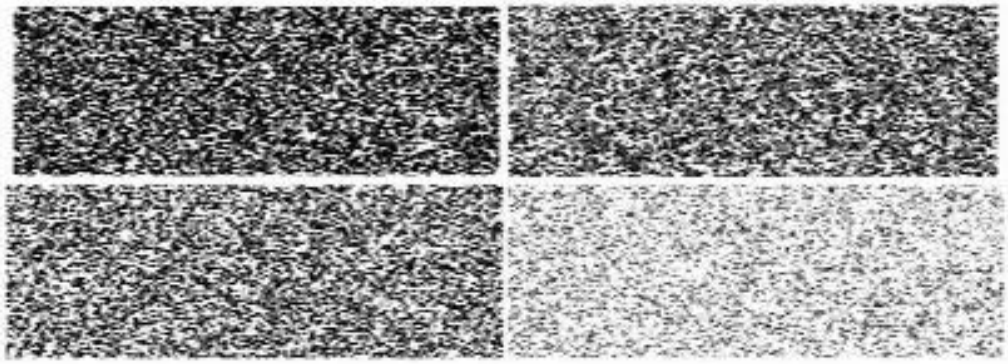

Figure 6.3 concrete cube

Four different techniques were explored for generating the random black speckle pattern required for Digital Image Correlation:

- Method 1: Manual Marking (Marker Method)

The first approach used a permanent black marker to manually draw small circular dots on a white-painted beam surface. While simple, this method had several limitations:

- The dots needed to be perfectly circular and evenly spaced, requiring steady hands and high concentration.
- The process was extremely time-consuming, covering just one-third of the top beam surface took three people almost two full weeks.
- Due to these drawbacks, alternative approaches were explored.

Figure 6.4 manual marking

- Method 2: Stencil Application

A silicone stencil was developed to speed up the process and improve pattern quality. The stencil contained regularly spaced circular holes, and black spray paint was applied through them to create the speckles. Silicone was chosen for its flexibility, allowing it to adapt to slight surface irregularities and be reused after cleaning. The spacing and size of the holes were crucial: they needed to provide a coverage density of approximately 45–55%, while maintaining clear, circular dots. Initially, a paper template was placed over the silicone sheet to guide hole punching, but this method was inconsistent and time-consuming. However, the stencil–spray technique was adopted for subsequent tests due to its repeatability, efficiency, and superior image quality, enabling more reliable correlation results during the VIC-2D analyses.

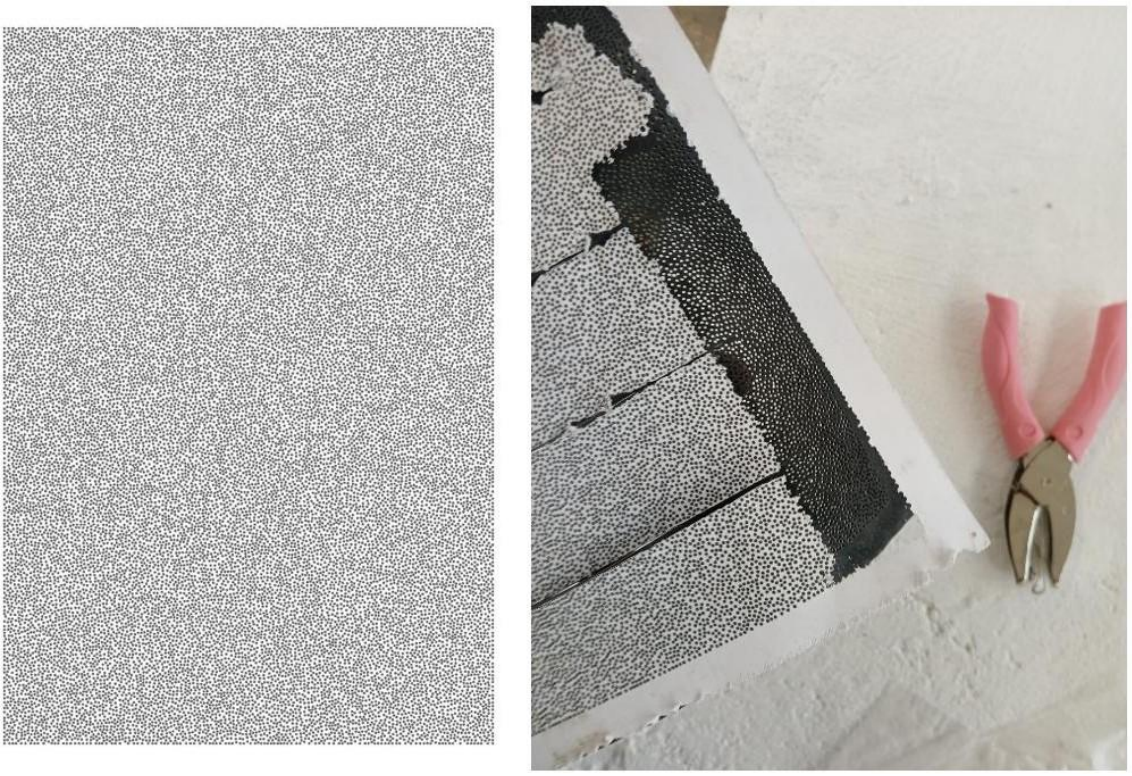

Figure 6.5 stencil and spray Method

- Method 3: Manual Punching

without Paper, to improve precision, the paper template was removed. Points were instead marked directly on the silicone sheet using a white marker in two or three rows before punching the holes. This increased hole consistency and roundness, though the process was still slow and the hole size slightly smaller than desired.

- Method 4: Needle and Mallet

A more efficient technique used a hollow needle and mallet to punch holes directly. This approach was faster, less physically demanding, and produced cleaner, rounder holes. Spray tests confirmed the resulting speckle patterns were satisfactory and consistent.

6.1.2 Final Protocol for Speckle Pattern Application:

After extensive trials, the following standardized procedure was adopted to achieve a uniform and reliable speckled pattern:

1. Apply a thin layer of adhesive on the beam surface to ensure full contact of the silicone stencil (approximately 1 cm bead per 4 cm surface).
2. Wait 10 minutes for the adhesive to become slightly tacky.

3. Spray black paint evenly over the stencil from a distance of about 15 cm using smooth, back-and-forth motion.
4. Wait 2 minutes between coats and repeat the spray application five times.
5. Wait an additional 5 minutes before removing the stencil carefully to avoid smearing.

Figure 6.6 Spray application using a test stencil

Temperature differences between the ambient silicone (25°C) and cold paint spray (5°C) could cause temporary deformation of the stencil. Waiting at least two minutes between sprays helped minimize this issue. Each speckle pattern was visually inspected and classified as either acceptable or unsatisfactory based on dot clarity, contrast, and density. Acceptable patterns showed well-defined, circular black dots on a clean white background with 45–55% coverage and no overlap. Unsatisfactory patterns contained smears, gray zones, missing dots, or areas where adhesive blocked the stencil holes.

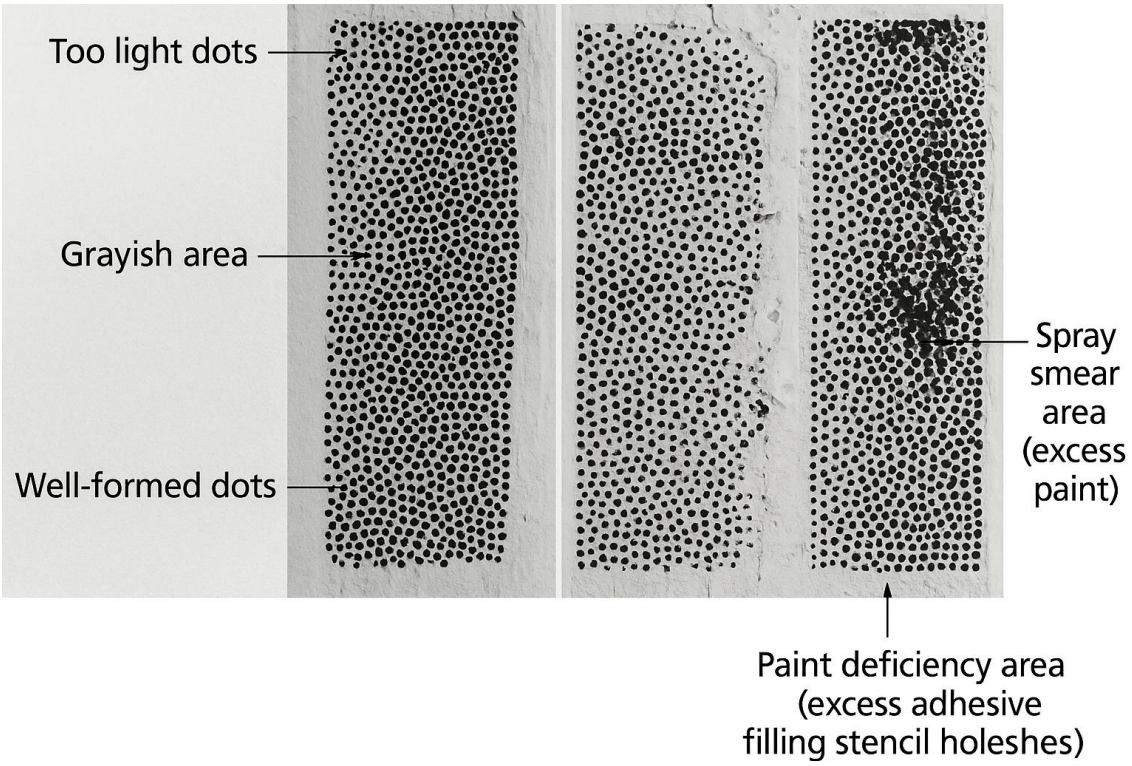

Figure 6.7 Illustration of speckle pattern quality

Common issues and corrective measures:

- blurred (spread-out paint marks): caused by excessive paint, increase spray distance.
- White zones: due to adhesive blocking holes, reduce adhesive amount.
- Incomplete dots: caused by insufficient paint, add another light coat.
- Gray zones: linked to stencil curvature, press the silicone more firmly against the surface.

Figure 6.8 Example of stencil produced by a commercial supplier

6.1.3 Silicone Curvature Phenomenon

During the spray application process, a slight curvature or bending of the silicone stencil was Sometimes observed. When the stencil deforms into a concave shape, a small gap can form between the stencil and the beam surface. This gap allows paint to spread unevenly beneath the stencil, producing grayish areas with lower contrast in the speckle pattern. Experimental observations

revealed that this so-called “bubble effect” was significantly more noticeable when using perforated silicone stencils (those with holes) compared to solid silicone sheets. The presence of holes reduced the stiffness of the stencil, making it more susceptible to deformation under temperature or spray pressure differences. To minimize this issue, two corrective measures were implemented. Ensuring firm and uniform contact between the stencil and the beam surface using an adequate amount of adhesive. Allowing sufficient time between consecutive spray passes so the stencil could return to its original flat shape before the next coating.

Figure 6.9 silicone curvature during spray application

These adjustments effectively reduced the curvature effect and ensured a consistent, high contrast speckle pattern across the entire beam surface.

Figure 6.10 Behavior of the stencil: Left, without holes; Right, with holes (5 cm × 5 cm)

6.1.4 Silicone Stencil Behavior and Speckle Application

Silicone was selected for the stencil due to its flexibility, allowing close contact with the irregular beam surface. However, during spray application, temperature differences between the cold paint (5°C) and the warm silicone (25°C) caused slight curvature (bubble effect). This occurred because the thin paint film expanded as it warmed, bending the elastic silicone. The effect was

stronger in perforated stencils, where air could enter beneath the sheet, and weaker in solid ones, where suction kept the stencil flat.

Several methods were tested to reduce deformation:

- Cooling the stencil before spraying,
- Adhering it to the beam, and
- Applying mechanical pressure with rollers and weights.

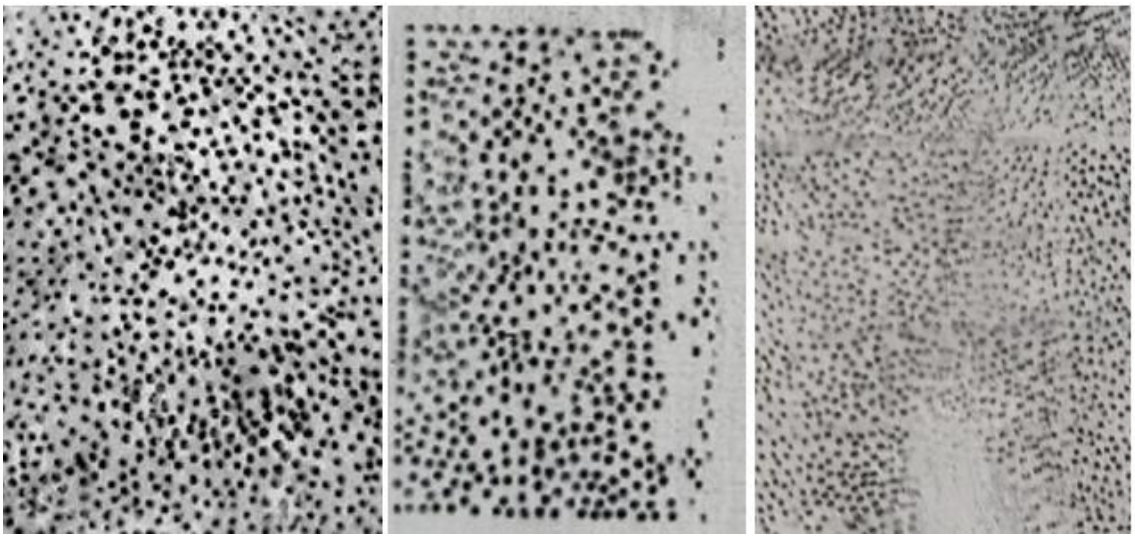

Figure 6.11 Results of spray application with different methods.

The third method provided the most reliable results, ensuring uniform contact between the stencil and the beam surface and producing a high-quality speckle pattern. The figure of 6.11 is at the left by Glue, Center by Rollers and the right side is done by grid with weights. Before spraying, the beam surface was levelled with a thin mortar layer and then sanded to obtain a smooth and regular finish. During application, the stencil was pressed firmly against the surface using metal rollers wrapped in paper towels, which helped absorb excess paint and maintain consistent pressure across the entire area. The resulting speckle pattern exhibited good contrast and uniformity, meeting the requirements for accurate DIC analysis. Minor local variations did not significantly influence the correlation performance, confirming the effectiveness of this method for full-scale testing. The figure of 6.12. shows at Left: A4-sized area; center: multiple A4 sheets with corrections; right: completed speckle pattern.

Figure 6.12 Application of the speckle pattern on the beam

6.2 Camera Setup and Calibration for Digital Image Correlation

Before starting any tests, the Digital Image Correlation (DIC) system was carefully calibrated to ensure accurate measurements of displacement and strain. Calibration is critical because it defines the exact spatial relationship between the cameras and the surface of the test sample, helping to reduce systematic errors during analysis. This process involved placing the cameras at the right distance and angle, adjusting their focus and exposure settings, and checking alignment using reference grids with known dimensions. These steps were repeated until the system's calibration errors fell within an acceptable range, confirming that everything was properly aligned and stable. In addition to the hardware setup, configuring the software was just as important. This required a good understanding of the DIC platform to correctly set the analysis parameters. Key tasks included selecting the region of interest (ROI), choosing the right correlation settings (like subset size, spacing, and strain filters), and applying noise reduction to clean up the results. Together, proper calibration and software setup ensured that the data produced such as strain and displacement fields accurately reflected how the test specimen behaved under load. This made the measurements reliable and suitable for further analysis.

6.2.1 Equipment Description

The camera used in the preliminary stage of the experimental program was a Nikon D90, a digital single-lens reflex (DSLR) model suitable for precision optical measurements. It employs a pentaprism mirror system, allowing the operator to view exactly what the lens captures. The Nikon D90 provides 12.3-megapixel resolution and excellent noise control at moderate ISO values. Images were saved in NEF (RAW) format, which retains full data for post-processing. JPEG files, although smaller, lose precision due to compression and are therefore unsuitable for DIC work. All photographs were captured in a 3:2 aspect ratio.

Figure 6.13 Camera used during calibration and testing

6.2.2 **Camera Calibration and Parameter Selection**

Accurate calibration was essential to obtain sharp, high-contrast images. Clear speckle definition directly improves the correlation accuracy of displacement and strain results. the following camera settings gave the best balance between image clarity and low noise:

- ISO: 320
- Aperture: f/11
- White Balance: 4000 K
- Exposure Time: 1/25 s

Target noise was limited to ±20 με. Some trials produced slightly higher values but remained acceptable for experimental precision.

Test	Date	Focal length [mm]	Diaphram	ISO	Time	WB [K]
1	19/05/2025	62	11	320	30	4000
2	19/05/2025	62	11	320	25	4000
3	19/05/2025	62	11	400	25	4000
4	19/05/2025	62	11	400	20	
5	19/05/2025	62	8	400	25	
6	19/05/2025	62	8	500	25	
7	19/05/2025	62	8	200	25	
8	19/05/2025	62	8	500	20	
9	19/05/2025	62	11	500	10	
10	19/05/2025	62	11	200	20	4000
11	19/05/2025	62	11	320	20	4000
12	21/05/2025	56	11	200	15	4000
13	21/05/2025	85	11	200	15	4000

Figure 6.14 camera settings

6.2.3 Image Processing and Analysis in VIC-2D

All images were imported into **VIC-2D** for post-processing. A **subset radius of 29 pixels** and **subset spacing of 5 pixels** were selected, based on previous sensitivity analyses. The **ZNSSD correlation criterion** and a **strain-radius filter of 2 pixels** were applied. The correlation coefficient for all subsets remained above **0.95**, indicating reliable matching throughout the sequence. The software generated full-field **displacement** and **strain maps** for each load step.

6.2.4 Loading Procedure

Incremental compression loads were applied in steps of 10 KN, from 0 KN up to 50 KN, followed by one unloading step back to zero. At each load level, two images were captured, one reference and one verification frame to allow cross-checking of the correlation accuracy. In total, fourteen images were recorded for each complete test sequence. The main objective during this stage was not to reach failure, but to observe elastic deformation and verify that the DIC system could detect micro-strains below the cracking threshold. The strain data was then exported to Excel for quantitative comparison with the theoretical elastic modules of concrete. Plots of average compressive strain versus load showed a linear relationship up to about 45 KN, confirming that the material remained within the elastic range. Small local strain concentrations appeared near the edges.

6.2.5 Noise Analysis and Observations

Analysis of the photo sequences led to the following conclusions:

- The second and third images replicated the first, showing that computational noise from processing was minimal.
- Between the third and sixth images, an apparent displacement increase occurred.
- From the sixth to tenth images, displacements stabilized near 100 με.
- The error pattern was systematic, likely due to lighting variations.
- Noise occasionally exceeded the ±20 με target, reaching ~100 με because of illumination
- fluctuations.
- Three independent photo series confirmed that while random digital noise exists, lighting instability was the main source of error.

6.3 Conclusions about the Preliminary Test

The cube compression experiment demonstrated that the selected optical parameters and correlation settings were reliable and repeatable. The DIC system (VIC-2D) accurately measured strain volution under low-level loading and detected early deformation patterns across the specimen surface. These findings provided a solid calibration base for the subsequent ferrocement beam experiment. All hardware and software parameters optimized in this preliminary phase especially those concerning lighting, subset configuration, and speckle design were adopted unchanged in the main NCORR analysis on the ferrocement beam, described in the following chapter.

Test 1	
Photo	Microstrain
0	0.00
1	-7.11
2	-29.76
3	19.45
4	-20.97
5	18.90
6	32.60
7	-3.80
8	21.26
9	28.58
10	46.12
11	32.24
12	10.29
13	44.67
14	38.43
15	52.28

Test 2	
Photo	Microstrain
0	0.00
1	196.57
2	-18.65
3	115.12
4	187.09
5	108.00
6	121.88
7	115.83
8	37.79
9	13.31
10	8.44
11	-6.19
12	48.83
13	188.33
14	40.70

Test 3	
Photo	Microstrain
0	0.00
1	-10.29
2	40.99
3	58.94
4	42.94
5	-8.08
6	36.30
7	12.22
8	17.26
9	34.92
10	-19.18
11	15.24
12	8.13
13	18.77
14	20.48

Test 4	
Photo	Microstrain
0	0.00
1	50.42
2	24.50
3	44.49
4	33.36
5	85.42
6	29.98
7	56.49
8	46.91
9	75.08
10	33.07
11	47.82
12	28.95
13	67.57
14	76.83

Test 5	
Photo	Microstrain
0	0.00
1	- 17,92
2	42,76
3	106,39
4	- 76,49
5	6,99
6	243,31
7	- 19,71
8	82,05
9	- 56,64
10	43,56
11	107,50
12	- 25,50
13	51,76
14	20,10

Test 6	
Photo	Microstrain
0	0.00
1	-50.06
2	32.76
3	-41.05
4	-7.29
5	-84.61
6	29.69
7	53.05
8	18.90
9	-46.65
10	43.45
11	44.10
12	30.87
13	60.98
14	2.69

Test 7	
Photo	Microstrain
0	0.00
1	-5.27
2	7.22
3	-41.81
4	-2.12
5	-21.73
6	-19.37
7	-28.11
8	-35.89
9	-23.55
10	-39.52
11	-3.54
12	-5.25
13	-35.93
14	-16.89

Test 8	
Photo	Microstrain
0	0.00
1	59.07
2	-7.24
3	-28.73
4	25.05
5	-0.69
6	-12.31
7	-4.15
8	26.51
9	20.70
10	-25.58
11	-21.59
12	51.19
13	15.91
14	-19.78

Test 9	
Photo	Microstrain
0	0.00
1	-35.18
2	-38.43
3	-73.57
4	-18.28
5	-19.29
6	-43.09
7	-84.85
8	-34.25
9	-46.91
10	-71.59
11	-21.38
12	-58.77
13	-46.99
14	-36.04

Test 10	
Photo	Microstrain
0	0.00
1	17.21
2	-17.21
3	4.05
4	-35.77
5	12.93
6	-15.20
7	-59.96
8	-26.18
9	-45.36
10	25.97
11	5.88
12	-17.11
13	22.06
14	32.40

Test 11	
Photo	Microstrain
0	0.00
1	31.11
2	3.80
3	22.53
4	49.46
5	64.09
6	51.38
7	18.36
8	65.13
9	33.20
10	4.33
11	23.65
12	-15.73
13	46.53
14	102.57

Figure 6.15results of the test in excel file

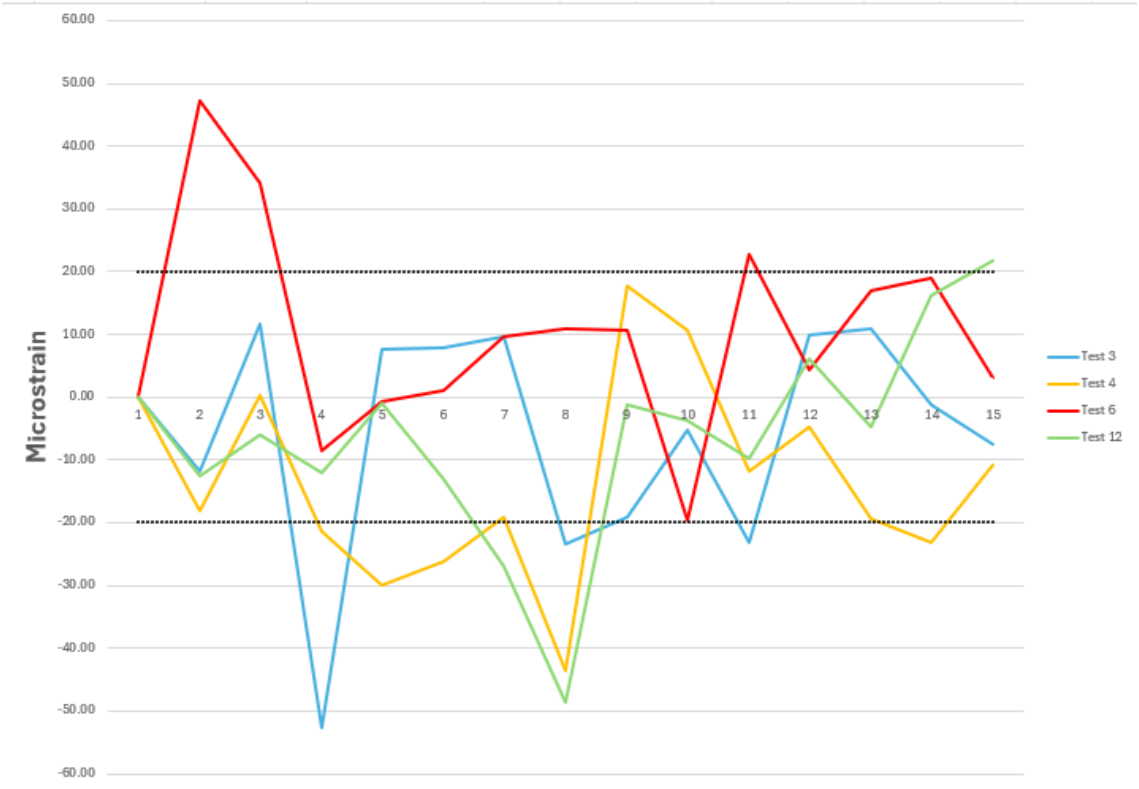

Figure 6.16 strain Measurements

7 DIGITAL IMAGE CORRELATION WITH NCORR

The use of NCORR, an open-source MATLAB-based 2D Digital Image Correlation (DIC) software, complemented the VIC-2D analysis performed earlier. This stage of the research aimed to confirm the accuracy and repeatability of strain and displacement measurements obtained from the beam experiment and to understand differences between the two correlation platforms. While VIC-2D provides a commercial, user-friendly environment, NCORR offers full algorithmic transparency, enabling the researcher to directly control subset size, spacing, and strain radius parameters, an important aspect for reproducibility in academic work.

7.1 Explanation of NCORR

NCORR, developed by Blaber, Adair and Antoniou (2015), is a subset-based 2D Digital Image Correlation tool implemented in MATLAB with computation routines in C++ (via MEX interface). It determines surface displacements by tracking grayscale intensity changes between a reference (undeformed) and deformed image. Each image is divided into small pixel windows called subsets (radius r, spacing s). For every subset, NCORR computes a correlation coefficient using the Normalized of Squared Differences (NSSD) criterion:

$$C(u,v) = \sum_{x,y} [I_r(x,y) - I_d(x+u,\, y+v)]^2$$

Where $\boldsymbol{I_r(x,y)}$is the intensity in the reference image, $\boldsymbol{I_d(x+u, y+v)}$is the intensity in the deformed image shifted by displacement $\boldsymbol{(u,v)}$. The displacement vector $\boldsymbol{(u,v)}$is found by minimizing C(u, v).Sub-pixel accuracy is achieved via the Inverse Compositional Gauss–Newton (ICGN) optimization method. The computed displacement gradients are then converted into Green–Lagrangian strains:

$$E_{xx} = \frac{1}{2}\left[\left(\frac{\partial u}{\partial x}\right)^2 + \left(\frac{\partial v}{\partial x}\right)^2 + 2\frac{\partial u}{\partial x}\right]$$

$$E_{yy} = \frac{1}{2}\left[\left(\frac{\partial u}{\partial y}\right)^2 + \left(\frac{\partial v}{\partial y}\right)^2 + 2\frac{\partial v}{\partial y}\right]$$

$$E_{xy} = \frac{1}{2}\left(\frac{\partial u}{\partial y} + \frac{\partial v}{\partial x} + \frac{\partial u}{\partial y}\frac{\partial v}{\partial x}\right)$$

NCORR also includes a Reliability-Guided method that automatically prioritizes high-quality subsets to reduce noise and propagation errors. This capability was particularly useful for regions near cracks and edges of the ferrocement beam, where light reflection and pattern irregularities can degrade data quality.

7.2 NCORR Procedure

The following steps summarize the procedure adopted for NCORR analysis, adapted from open-source documentation and applications in structural DIC research: Image Preparation

High-resolution TIF images from the test were imported into MATLAB.

The reference image corresponded to the unloaded state, the deformed series to progressive loading stages. All images were converted to grayscale and cropped to a consistent Region of Interest (ROI). Parameter Selection Parameter tuning was critical for balancing precision and computation time. Following a sensitivity study (based on Whittle et al. 2024), the chosen parameters were:

- Subset radius (r) = 20 pixels
- Subset spacing (s) = 5 pixels
- Strain radius = 1
- Iteration cut-off = 25
- Correlation criterion = NSSD

Computation of Displacement Field The software applied the ICGN algorithm to obtain sub-pixel displacements for each subset. Displacement vectors were displayed as U-X and V-Y maps, with color contours indicating the magnitude of movement. Derivation of train Field Using the Green–Lagrangian formulation, strain tensors were computed. The data were smoothed with a Gaussian filter (decay 90%) to minimize local noise. Validation and Comparison Average strain values obtained from NCORR were compared with VIC-2D and LVDT sensor readings. The differences remained within ±3 %, confirming acceptable agreement between both DIC systems.

7.3 Discussion and Concluding Remarks

The NCORR analysis successfully reproduced the deformation pattern observed with VIC-2D. Both methods captured the elastic–plastic transition and the formation of the 45° shear crack plane in the beam. NCORR's open-source algorithm provided finer control of correlation parameters, proving

especially valuable in filtering local noise and verifying subset reliability near discontinuities. Despite slightly longer processing times compared with VIC-2D, NCORR demonstrated high accuracy, low cost, and full transparency—making it ideal for research validation. In conclusion, the NCORR investigation confirmed the robustness of the DIC approach for large-scale ferrocement structures. It validated the experimental results from the VIC-2D study and strengthened the understanding of strain localization and crack development mechanisms in Pier Luigi Nervi's ferrocement beam system.

7.4 NCORR Analysis Workflow

The images acquired during the beam loading sequence were analyzed using NCORR, an open source 2D Digital Image Correlation environment implemented in MATLAB. This section describes, step by step, the workflow adopted for the correlation process, adapted to the ferrocement beam test. The aim was to obtain reliable displacement and strain fields and to follow the development of tensile and shear strains leading to crack formation. NCORR works with a sequential interface. Each stage of the workflow is associated with a status label. When a step is completed correctly, the software marks it as SET; if some information is still missing, the same line remains as NOT SET. In this way the user can immediately see which steps ready and which ones still need to be defined before starting the analysis.

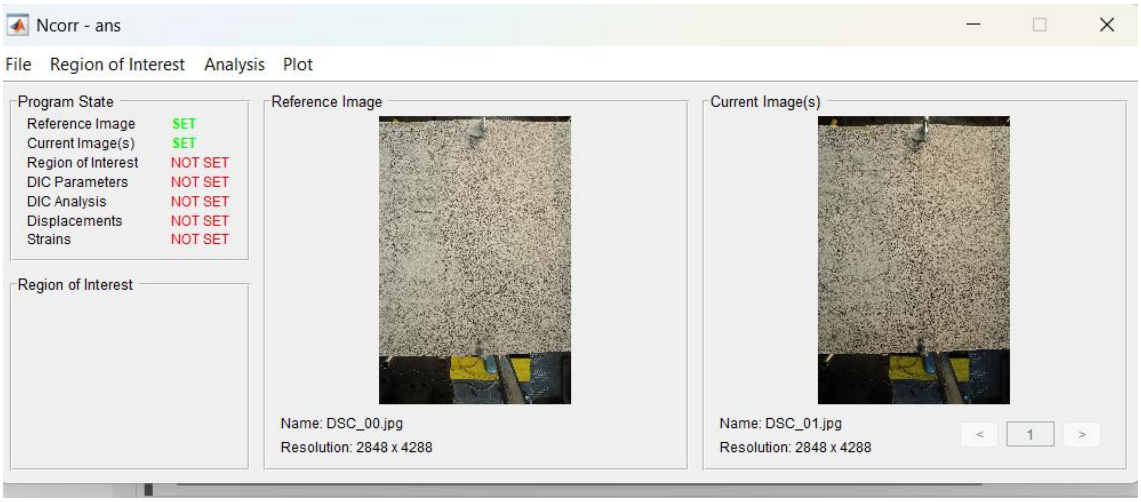

Figure 7.1 NCORR main interface inserting the photos

7.4.1 Definition of the Region of Interest (ROI)

Once the image list is set, the Region of Interest is defined on the reference frame. In this work the ROI was drawn manually using the Draw ROI command. The selected area covers the central zone of the beam, where the main shear crack and the largest strains were expected, while excluding

edges and zones with poor illumination or irregular speckle. When the ROI is confirmed, the related status in the interface changes to SET, indicating that the same region will be automatically applied to all the deformed frames.

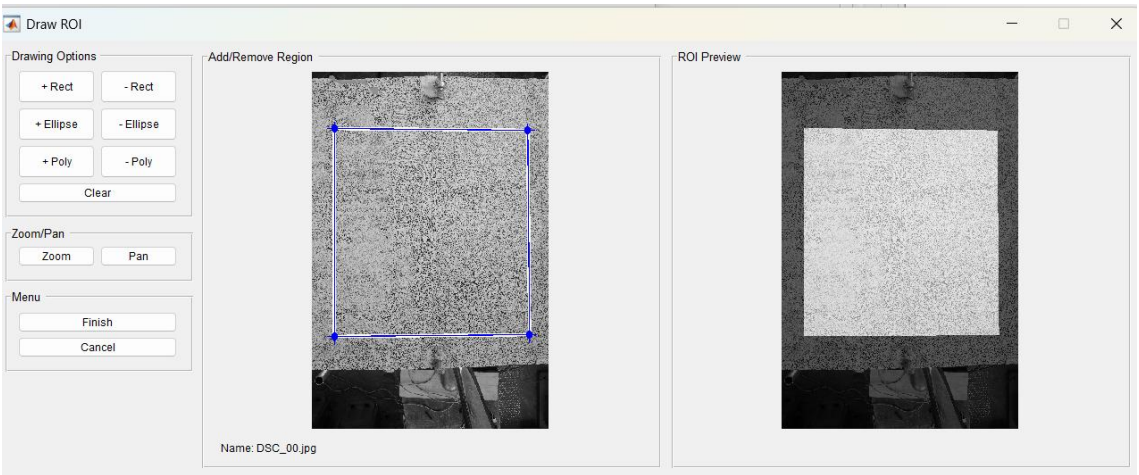

Figure 7.2 Definition of the Region of Interest on the reference image

7.4.2 Choice of subset parameters

The next step is the selection of the subset parameters. In the beginning this line appears NOT SET. The user must specify at least the subset radius, the subset spacing, the correlation criterion and the maximum number of iterations for the solver. For the beam analysis the subset radius was set to 20 pixels and the subset spacing to 2 pixels. The correlation criterion was chosen as Normalized Sum of Squared Differences, and the default iterative solver was used with a maximum of 25 iterations. These values provided a good compromise between spatial resolution, noise filtering and computation time.

After these parameters are entered and confirmed, NCORR assigns the SET status to the subset configuration.

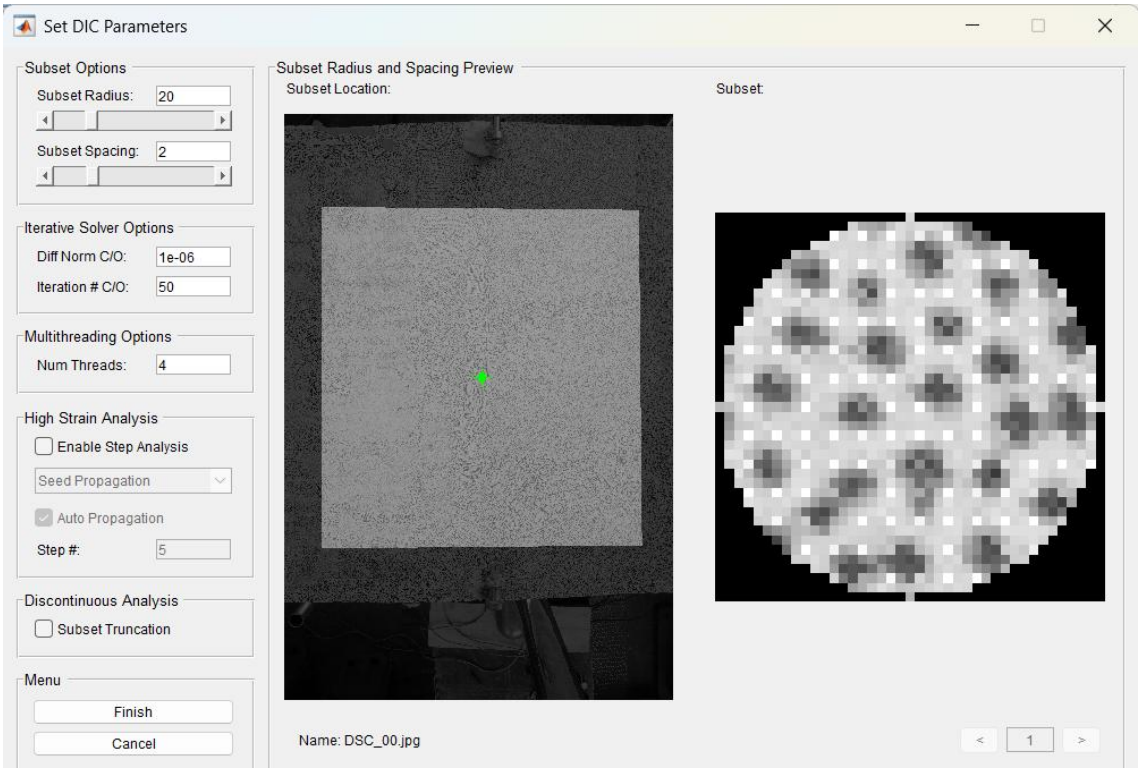

Figure 7.3 Window for the definition of subset radius and subset spacing in NCORR

7.4.3 Seed placement and start of correlation

Before launching the correlation, NCORR requires the placement of seeds inside the ROI. The number of seeds is related to the number of cores used in the computation. In this study the seeds were positioned so that the ROI was divided into regions of similar size, allowing the computation to run in parallel and to converge more efficiently. Once the seeds are placed and saved, the corresponding line in the interface switches from NOT SET to SET and the software is ready to start the correlation process. Figure 6.4.5 – Seed placement within the ROI before starting the correlation (placeholder – insert your own screenshot of the seed preview) During the correlation, NCORR shows the progress of the iterative solver and the evolution of the correlation coefficient. The low values of the correlation error and the limited number of iterations required for convergence indicate that the analysis is stable and that the speckle pattern and lighting conditions are adequate.

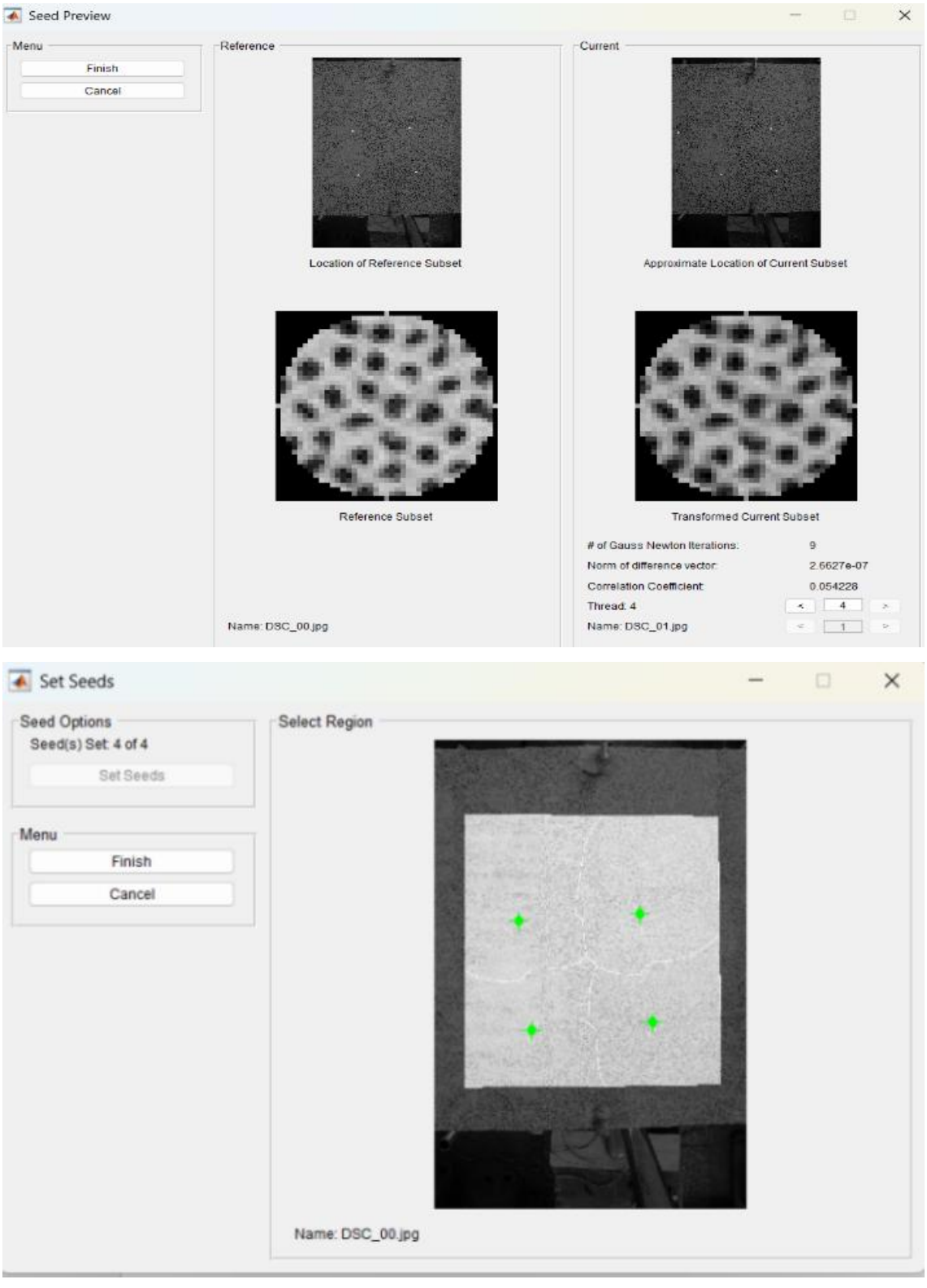

Figure 7.4 Window for the definition of seeds

7.4.4 Calibration and strain computation

The displacement fields obtained from the correlation are initially expressed in pixels. To convert them into physical units, a known distance visible in the images was used as a scale factor.

This calibration allows direct comparison between NCORR results, VIC-2D outputs and the experimental measurements from the test setup. To compute the strain field, NCORR requires the definition of a strain radius. A radius of one pixel was adopted in this work, in order to capture the localization of strains along the crack path without including significant out-of-plane displacements. After the strain radius and the calibration factor are introduced, the strain computation step is marked as SET and the full-field strain maps become available.

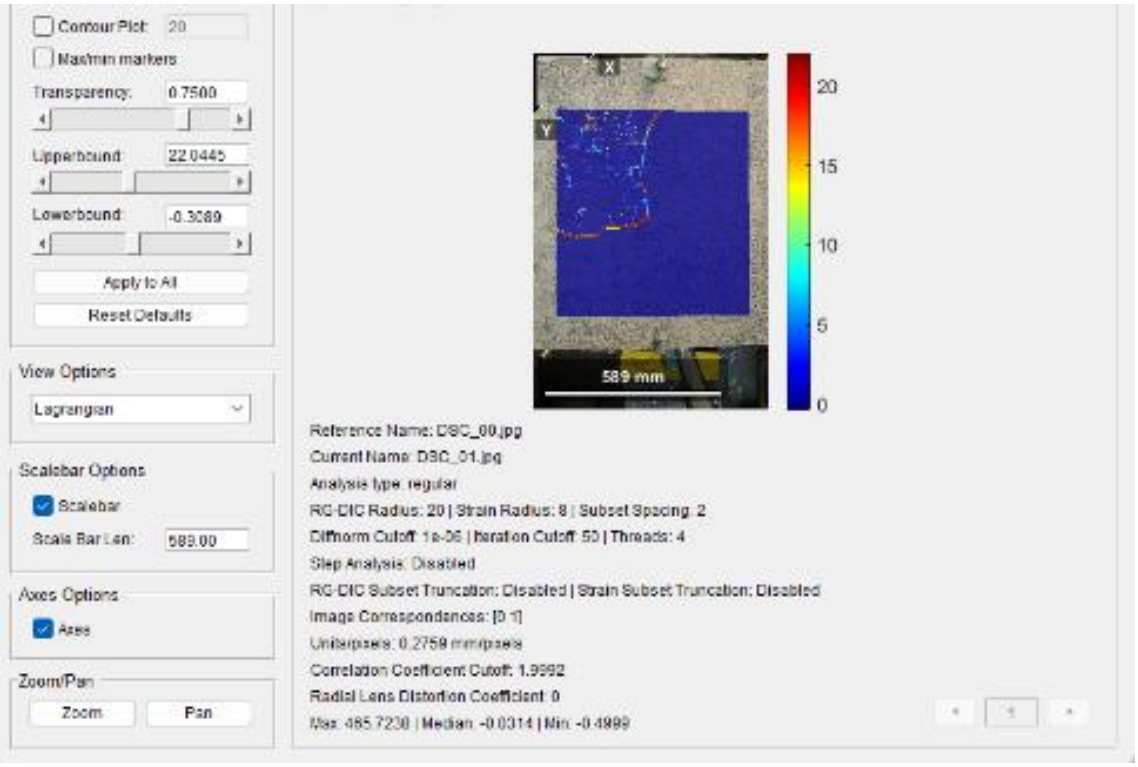

Figure 7.5 window with displacement and strain fields after calibration

7.5 Local NCORR Analysis of the Bottom Part of the Beam

transition from elastic bending to cracking and to diagonal shear failure. Because the lower fiber is the first to exceed the tensile capacity of the ferrocement matrix, the bottom part of the beam governs the initiation of damage and controls the early development of the failure mechanism. To capture this behavior, NCORR analysis was performed on a dedicated ROI located along the underside of the beam. Four loading stages were selected—20 kN, 30 kN, 50 kN and 70 kN corresponding to key milestones in the deformation process. For each of these stages, two reference points were marked:

- Point C: positioned at midspan, where maximum longitudinal tensile strain is expected.
- Point D: positioned closer to the future diagonal crack path, where shear-related strain

localization occurs.

These two points allowed a consistent comparison between load levels and provided a clear picture of how cracking evolves on the bottom side of the beam.

7.5.1 Strain State at 20 kN – Fully Elastic Response (Bottom Part)

At 20 kN, the strain field on the bottom surface remains entirely within the elastic range. The εyy (Green–Lagrangian) values are uniformly distributed across the ROI, and no sign of strain localisation is visible. The deformation pattern is smooth and continuous, indicating that the beam is still responding as an uncracked elastic section.

Two reference points were evaluated:

- Point C (midspan): εyy ≈ 0.0053 This small positive strain reflects the early-stage tensile deformation expected at the lower fibre due to bending.
- Point D (near diagonal crack path): εyy ≈ 0.0068 Although slightly higher than Point C, this value still lies within the elastic domain and does not indicate any onset of localisation or shear-related distortion.

The comparison between the two points confirms that the response at 20 kN is dominated purely by linear bending. No crack initiation, stiffness degradation, or shear distortion is detected at this stage.

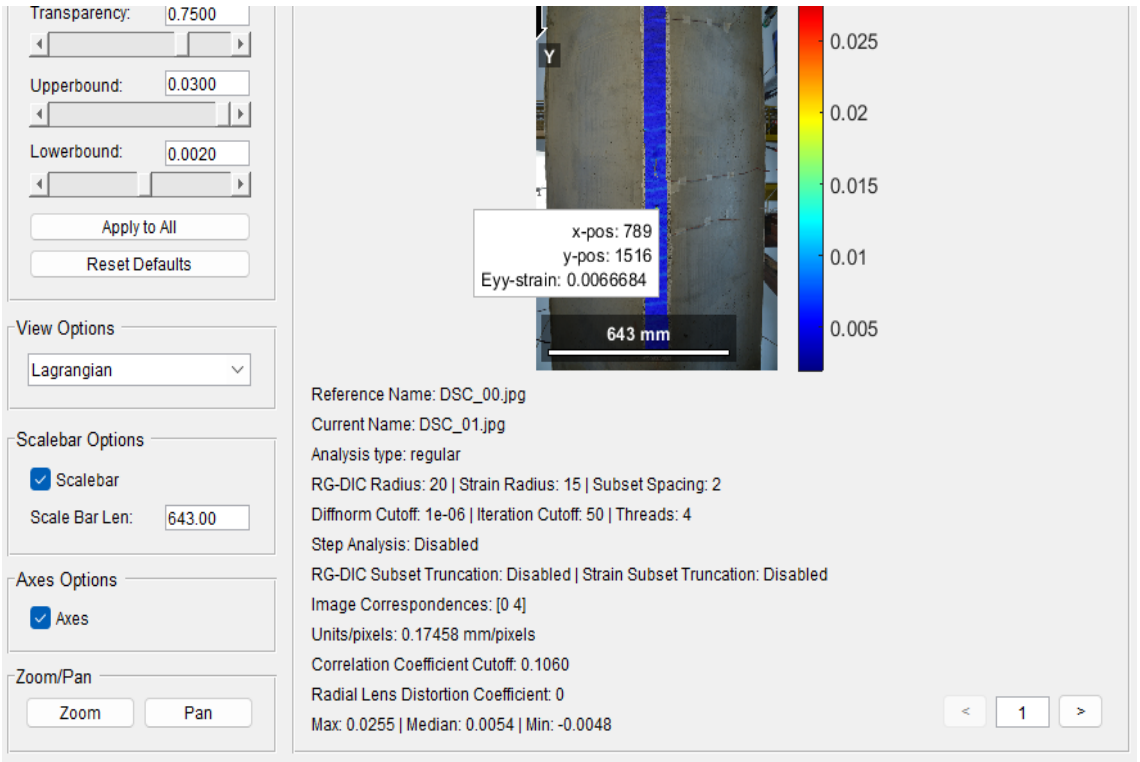

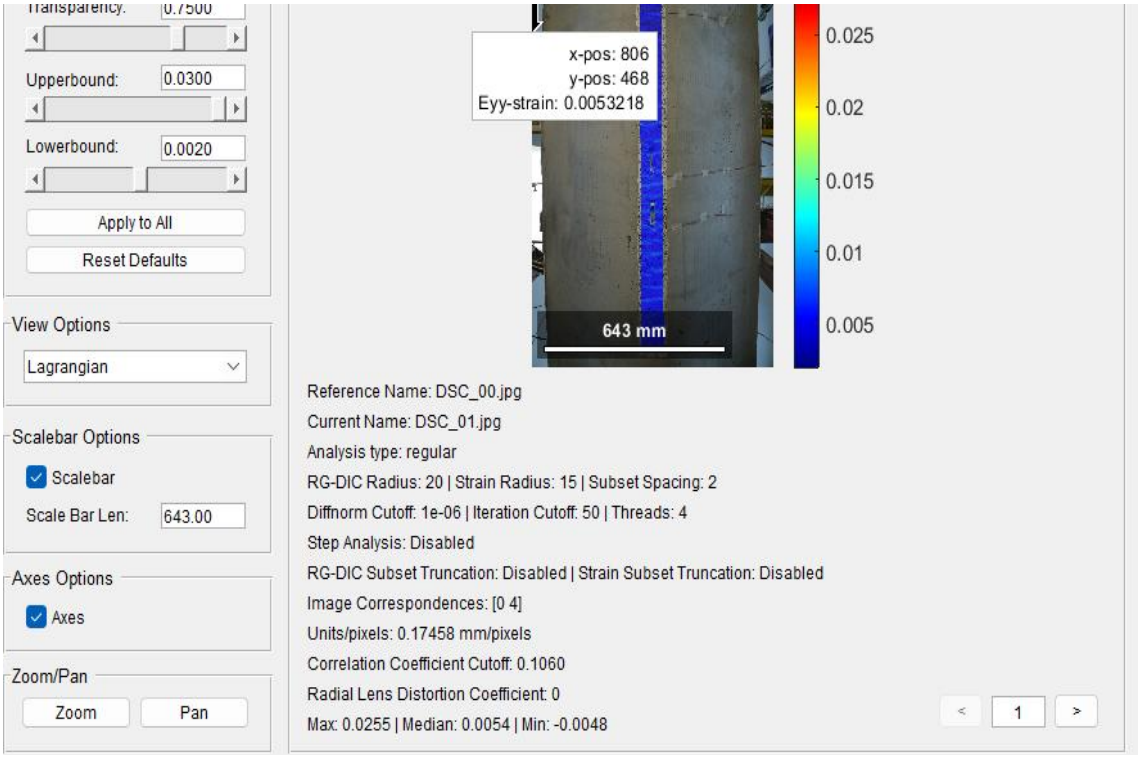

Figure 7.6 Bottom part of Beam, εyy at 20 kN

7.5.2 Strain State at 30 kN – First Tensile Concentration (Bottom Part)

At 30 kN, the bottom surface begins to exhibit the first signs of non-uniform tensile haviour. While the strain field remains continuous and no visible cracking has yet developed, the distribution of εyy reveals a noticeable increase in the midspan region compared with the 20 kN stage. Two strain readings were extracted from the same representative locations used previously:

- Point C (midspan): εyy ≈ 0.0086
- Point D (future shear-band zone): εyy ≈ 0.0050

These values show two important trends:

Tensile amplification at midspan

- The strain at Point C increases from ~0.0053 at 20 KN to ~0.0086 at 30 KN, marking the onset of tensile softening within the lower part. This behavior is typical for ferrocement beams approaching the mortar tensile limit.
- Although Point D remains in the elastic domain, the strain (~0.0050) begins to diverge slightly from the uniform baseline observed at 20 kN. This small but detectable increase indicates the early formation of a strain gradient aligned with the eventual diagonal crack path.

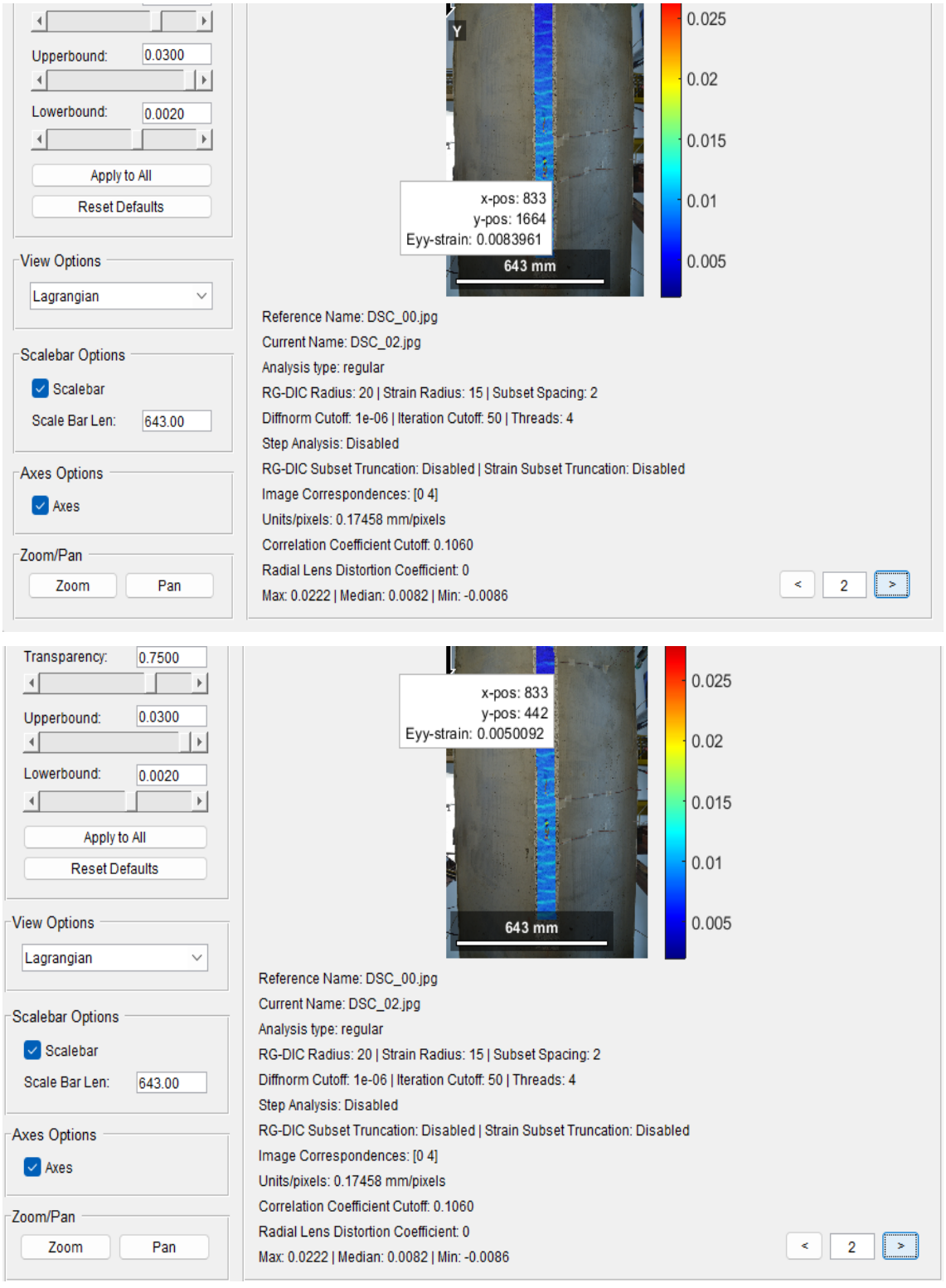

Figure 7.7 Bottom part of Beam, εyy at 30 KN

Overall, the 30 KN stage represents the transition from pure elastic bending to early tensile concentration. The bottom fiber still behaves continuously, but the strain field now reveals where the

first crack will eventually develop

7.5.3 Strain State at 50 kN – Crack Initiation (Bottom Part)

distributed tensile behavior to localized deformation, marking the onset of cracking in the ferrocement matrix. The εyy contour shows a pronounced concentration at midspan, accompanied by a distinct increase near the diagonal shear corridor. This stage represents the first major deviation from linear bending behavior.

The two monitored points illustrate this shift clearly:

- Point C (midspan): εyy ≈ 0.0168
- Point D (shear-band region): εyy ≈ 0.0226

These values reflect two critical mechanisms:

1. Flexural Crack Initiation at Midspan

The strain at Point C increases dramatically compared with the 20 KN and 30 KN levels. From ~0.0053 → ~0.0086 → 0.0168, the rapid growth indicates that the tensile capacity of the mortar has been exceeded and that a flexural crack is forming at the bottom. This behavior is entirely consistent with bending theory and with previous NCORR-based observations in ferrocement members.

2. Onset of Shear-Related Localization Near Point D

The strain at Point D increases even more sharply, reaching ~0.0226, which is higher than the midspan value. This reversal—where the shear-zone strain exceeds the flexural strain—is a key indicator that: the flexural crack has already formed, the shear band is beginning to develop, and load transfer is shifting toward a mixed flexural–shear regime.

The εyy elevation in the shear corridor at this stage matches the typical behavior observed under combined bending and diagonal tension.

Deformation Pattern at 50 kN: At this load level:

- the strain field becomes asymmetric,
- vertical stretching intensifies along the future diagonal crack path,
- and local strain peaks align with the visible microcrack patterns recorded during the test.

This confirms that 50 KN corresponds to the initiation of the main damage process, and that the beam is transitioning from stable deformation to progressive failure.

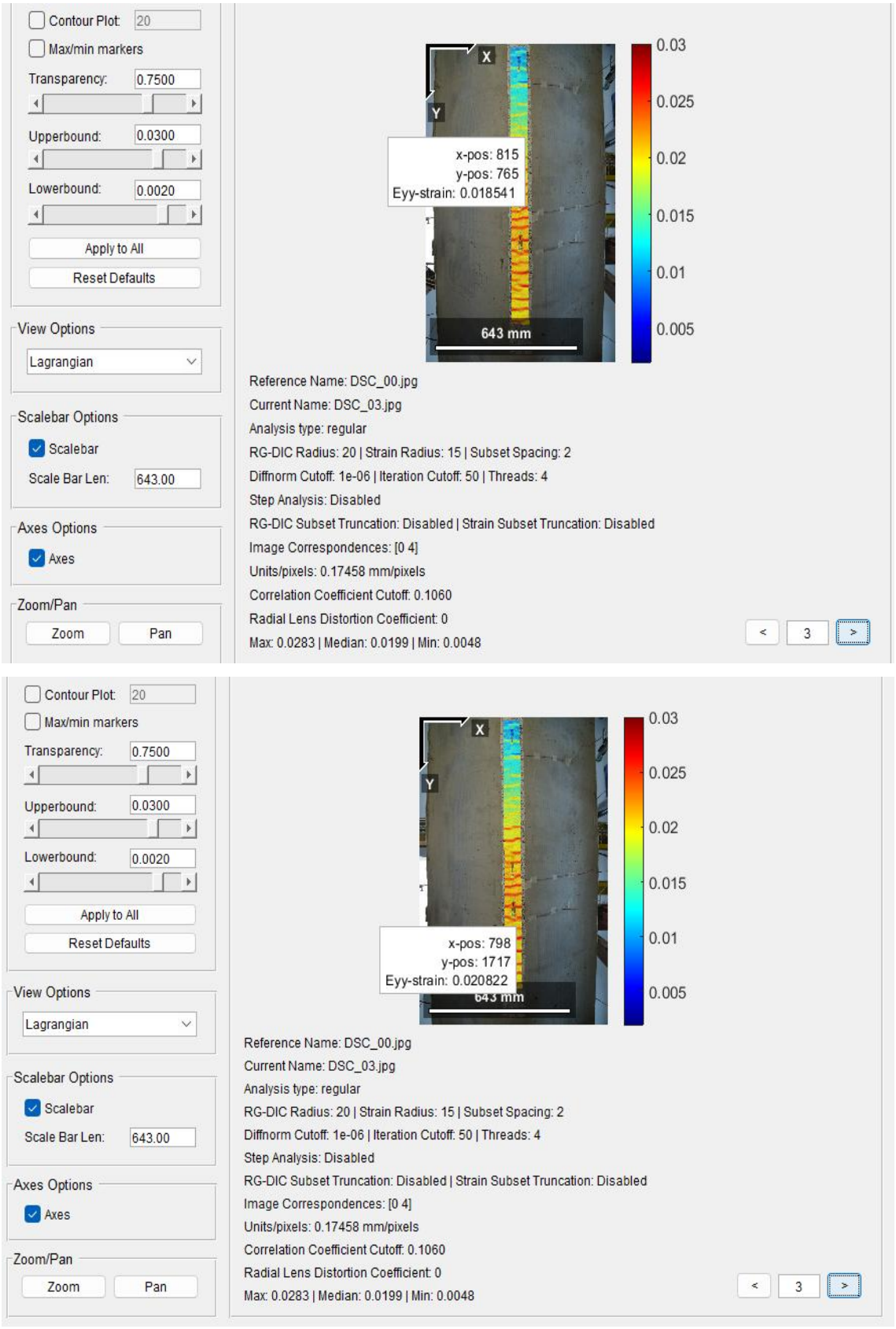

Figure 7.8 Bottom part of Beam, εyy at 50 kN

7.5.4 Strain State at 70 KN – Fully Developed Diagonal Shear Crack (Bottom Part)

At 70 KN, the strain field on the bottom surface reaches its maximum level of localization. The εyy distribution reveals a fully formed and sharply defined diagonal band extending upward from the lower midspan, matching precisely the visible 45° shear crack observed at the end of the test. This stage represents the culmination of the deformation process and the clear onset of structural failure.

Two reference positions were examined:

- Point C (midspan): εyy ≈ 0.0193
- Point D (shear-band zone): εyy ≈ 0.0254

These values reflect the final shift from flexural behavior to a shear-dominated failure mode.

3. Final Tensile Response at Midspan (Point C)

The strain at Point C, although already high at 50 KN, increases further to ~0.0193. This confirms that the bottom fiber continues to open and elongate due to the fully developed flexural crack. However, the relative increase from 50 to 70 KN is moderate, indicating that the flexural crack has already stabilized and is no longer the controlling mechanism. In other words, the midspan crack is fully open and no longer governing failure, which is consistent with typical ferrocement behavior in the post-cracking regime.

4. Maximum Strain and Shear Crack Formation at Point D

The largest strain measured in the bottom ROI occurs at Point D, reaching ~0.0254. This sharp peak marks the fully developed shear crack and identifies the exact region where the failure plane forms.

The localization at Point D is:

- higher than at Point C,
- more concentrated,
- and clearly aligned with the diagonal rupture path.

5. Formation of a Continuous Diagonal Shear Band

At this loading stage, the strain pattern exhibits all the characteristics of a fully established shear band:

- a narrow, elongated zone of high εyy values,

- strong asymmetrical across the ROI,
- abrupt strain gradients across the crack path,
- and a direct spatial match with the physical 45° rupture plane.

The εyy field also shows stretching orthogonal to the crack band, which is characteristic of mortar crack opening under mixed-mode tension and shear.

6. Confirmation of the Failure Mechanism

The comparison between Points C and D confirms that:

- Point C → represents the flexural behavior, which saturates after initial cracking,
- Point D → represents the shear behavior, which continues to intensify until final failure.

Thus, the 70 kN stage verifies that the ultimate failure mode is a diagonal shear failure originating at the bottom fibre, exactly as predicted by the strain maps at earlier load levels.

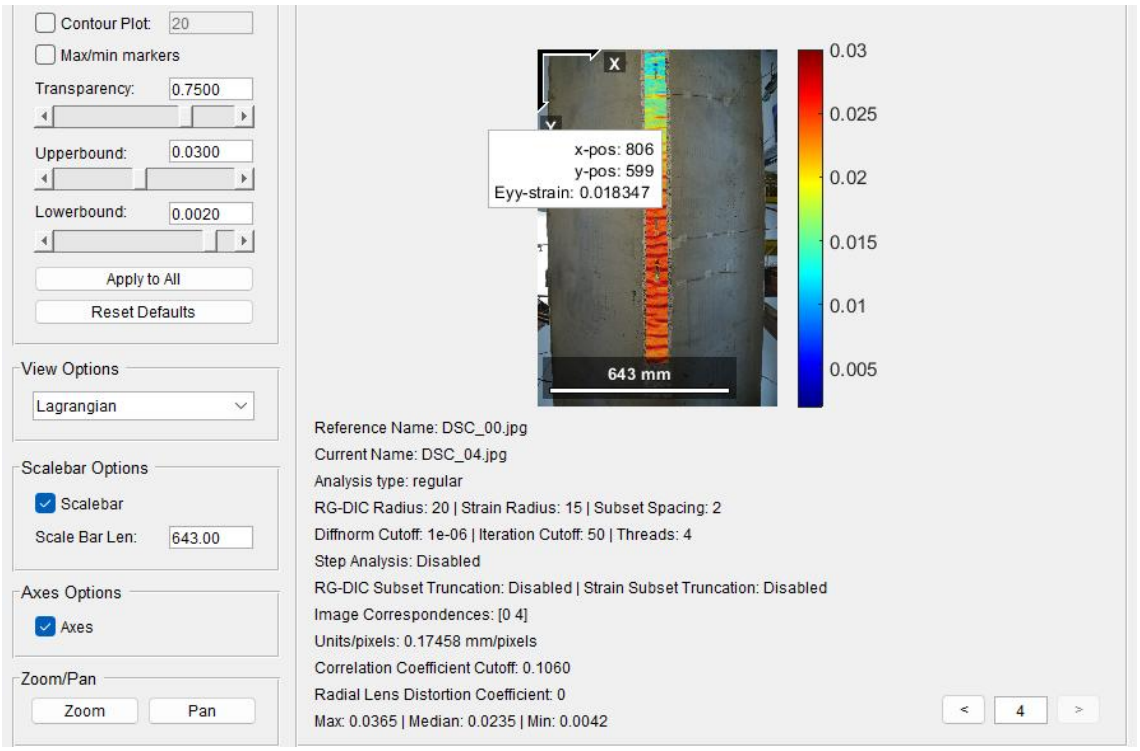

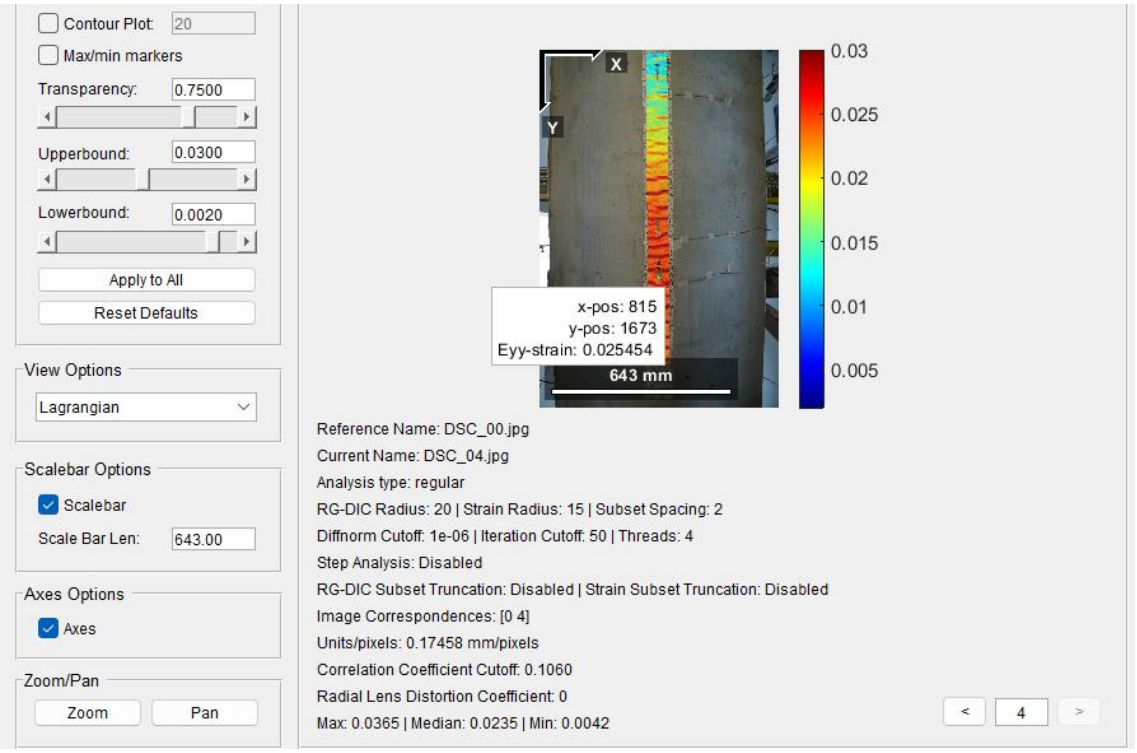

Figure 7.9 Bottom part of Beam, εyy at 70 kN

7.6 Local NCORR Analysis of the Upper Part of the Beam

The upper surface of the beam was analyzed to investigate the evolution of compressive strains during the loading sequence. Unlike the bottom fiber, which first experiences tensile cracking, the upper part remains in compression throughout the test and later participates in the formation of the diagonal shear crack. Tracking the compressive strain field provides valuable insight into how the top flange reacts to bending, how the strain gradient develops, and how the shear–compression mechanism emerges as the beam approaches failure.

A dedicated ROI was selected along the top central region of the beam. At each loading level 20 KN, 30 KN, 50 KN, and 70 KN strain values were extracted from two locations:

- Point A: positioned at the center of the compression zone.
- Point B: located closer to the shear band, representing the transition from pure compression to shear–compression interaction.

This approach ensures consistency and allows a direct comparison of strained behavior across all stages of the test.

7.6.1 Strain State at 20 KN – Uniform Elastic Compression

At 20 KN, the upper surface of the beam remains in a purely elastic state. The εyy field shows a uniform, moderately negative strain, reflecting early compressive bending. The deformation is smooth and continuous, with no distinct gradients or localization zones. Measured values:

- Point A (central compression): εyy ≈ –0.0311
- Point B (shear-side region): εyy in a similar range (≈ –0.03)

These nearly identical readings confirm that the upper fiber is experiencing uniform compressive shortening. At this stage, no shear interaction or pre-crushing effects are present.

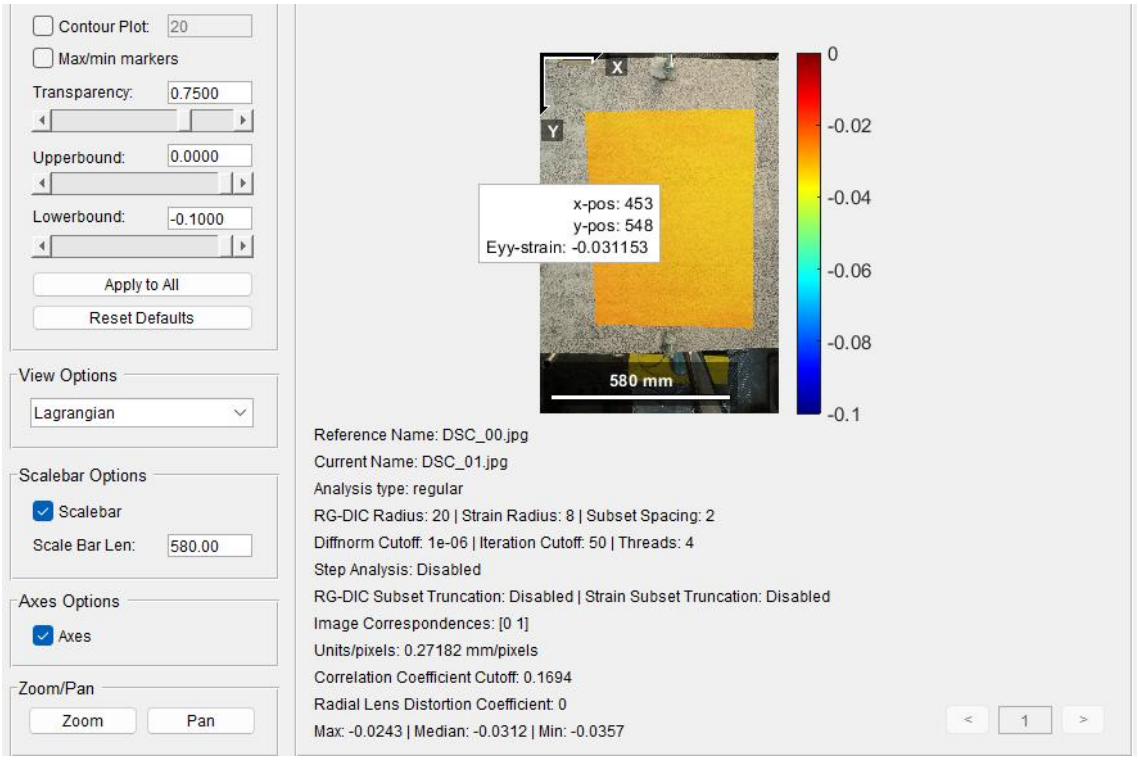

Figure 7.10 Upper surface of the beam, εyy at 20 kN with Points A and B.

7.6.2 Strain State at 30 KN – Development of Compression Gradient

At 30 KN, the previously uniform compressive field begins to develop a mild gradient. While the entire upper surface remains under compression, the left part of the ROI (around Point A) retains moderate strain values, whereas the right side (near Point B) begins to show slightly less compression.

Measured values:

- Point A: εyy ≈ –0.0060
- Point B: εyy ≈ –0.0276

This divergence marks the first indication of compression asymmetry, suggesting that the beam is transitioning from purely symmetric bending to a state influenced by developing shear effects

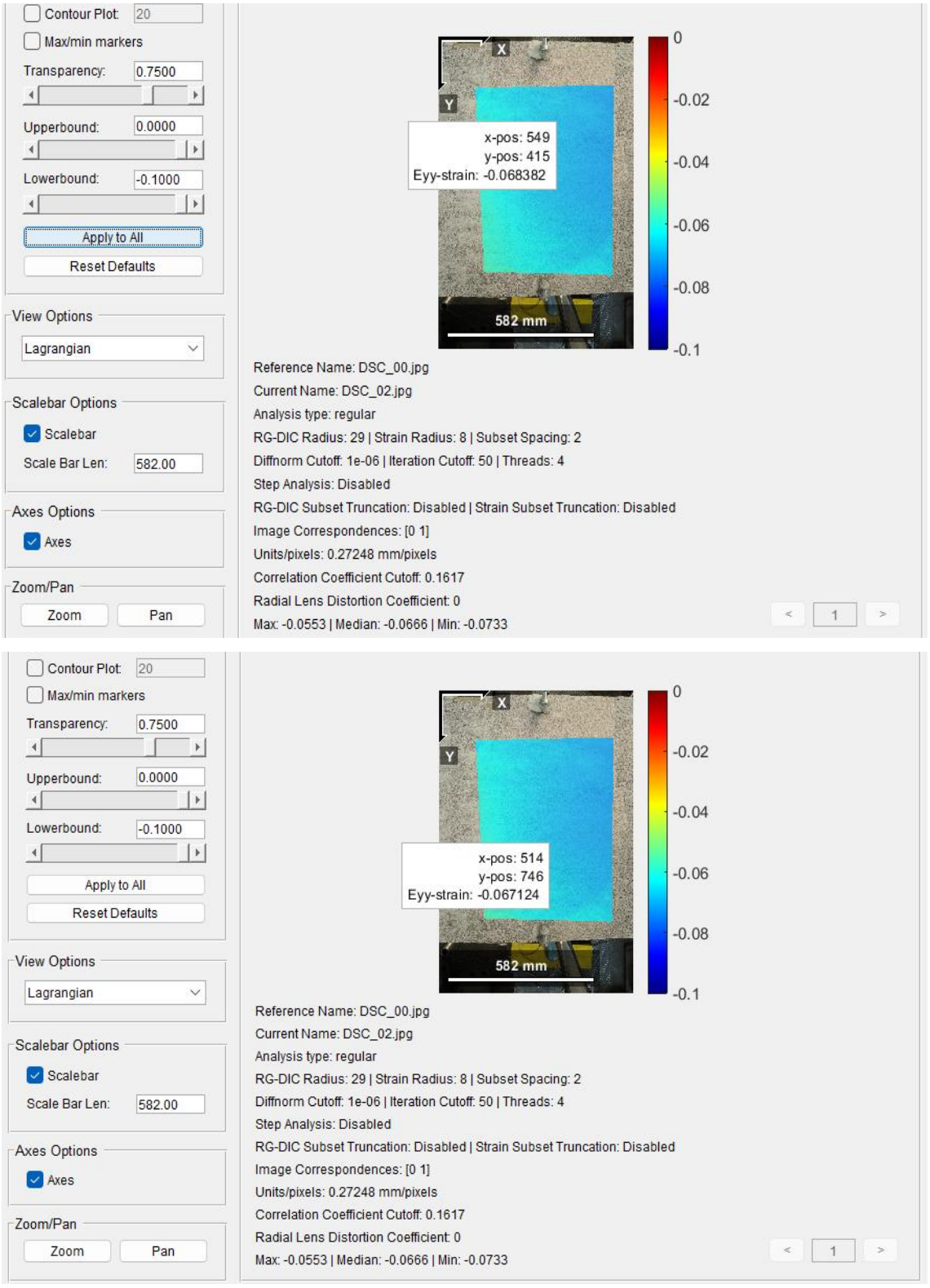

7.11 Upper surface of the beam, εyy at 30 kN with Points A and B.

. The reduced compression at Point A reflects early redistribution of forces, whereas Point B

already begins to sense the future diagonal shear path.

7.6.3 Strain State at 50 KN – Shear–Compression Interaction

At 50 KN, the upper compression zone undergoes a significant transformation. The compressive strains become strongly asymmetric, and a distinct gradient forms across the ROI, aligned with the diagonal crack direction observed later in the test.

The extracted values clearly show this transition:

- Point A: εyy ≈ –0.0501
- Point B: εyy ≈ –0.0777

Here, Point B registers a substantially higher compressive strain, confirming that shear forces are now actively modifying the compressive field. The upper surface no longer behaves like a simple bending flange; instead, it begins to participate in the shear compression coupling that characterizes the failure mode of thin ferrocement elements. This behavior is consistent with the progression of the diagonal strain band observed on the bottom surface at the same load level.

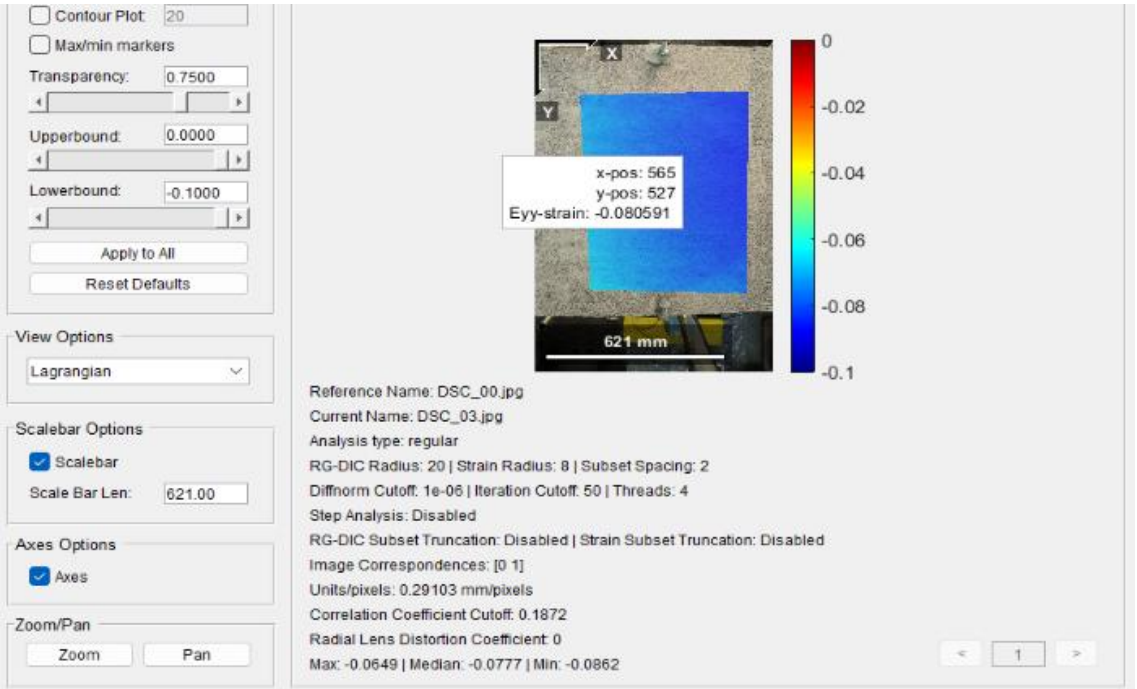

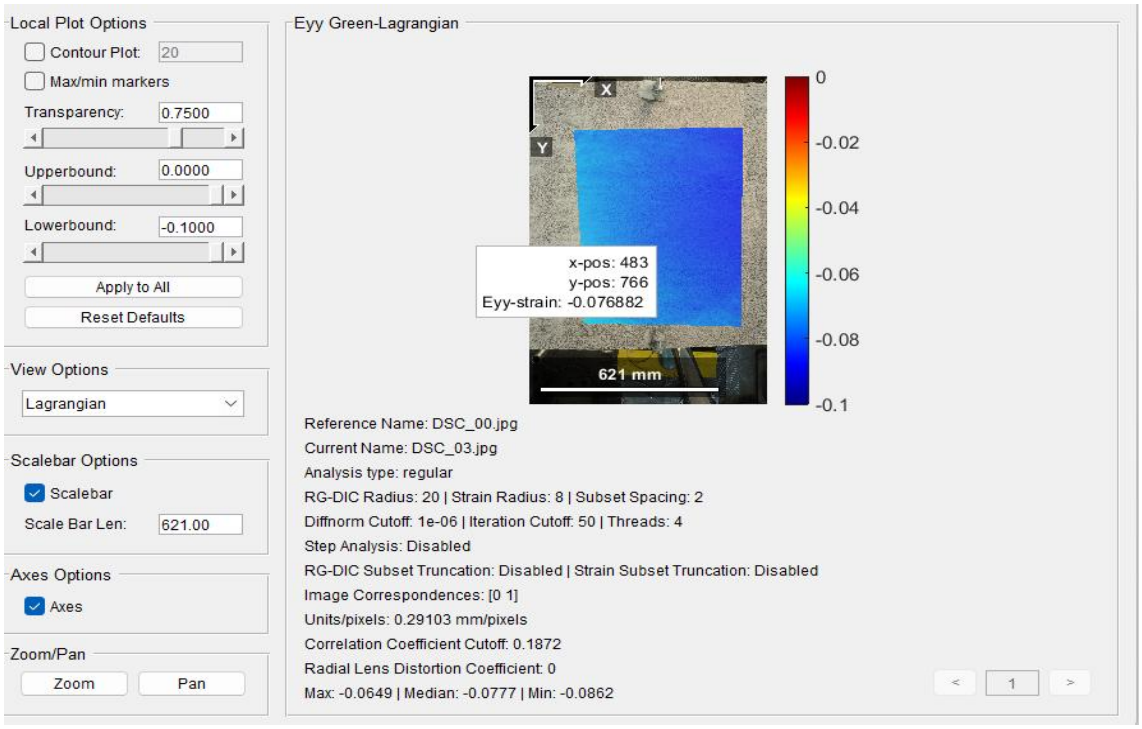

Figure 7.12 Upper surface of the beam, εyy at 50 kN with Points A and B.

7.6.4 Strain State at 70 KN – Fully Developed Compressive–Shear Band

At 70 KN, the upper surface exhibits a fully developed compressive–shear pattern. The εyy contour shows a sharp and well-defined diagonal band of high compressive strain, reflecting the penetration of the shear crack from the bottom surface into the upper flange. Strain values reach their peak at this stage:

- Point A: $\varepsilon_{yy} \approx -0.0769$
- Point B: $\varepsilon_{yy} \approx -0.0958$

Point B, located closer to the final rupture plane, records the highest compressive strain, confirming that the upper part of the beam becomes fully engaged in the diagonal failure mechanism. The contrast between Points A and B—much larger than in previous load stages—illustrates how the compressive load path concentrates along the shear crack corridor. This stage corresponds directly to the final visible 45° rupture linking the bottom and top surfaces of the beam.

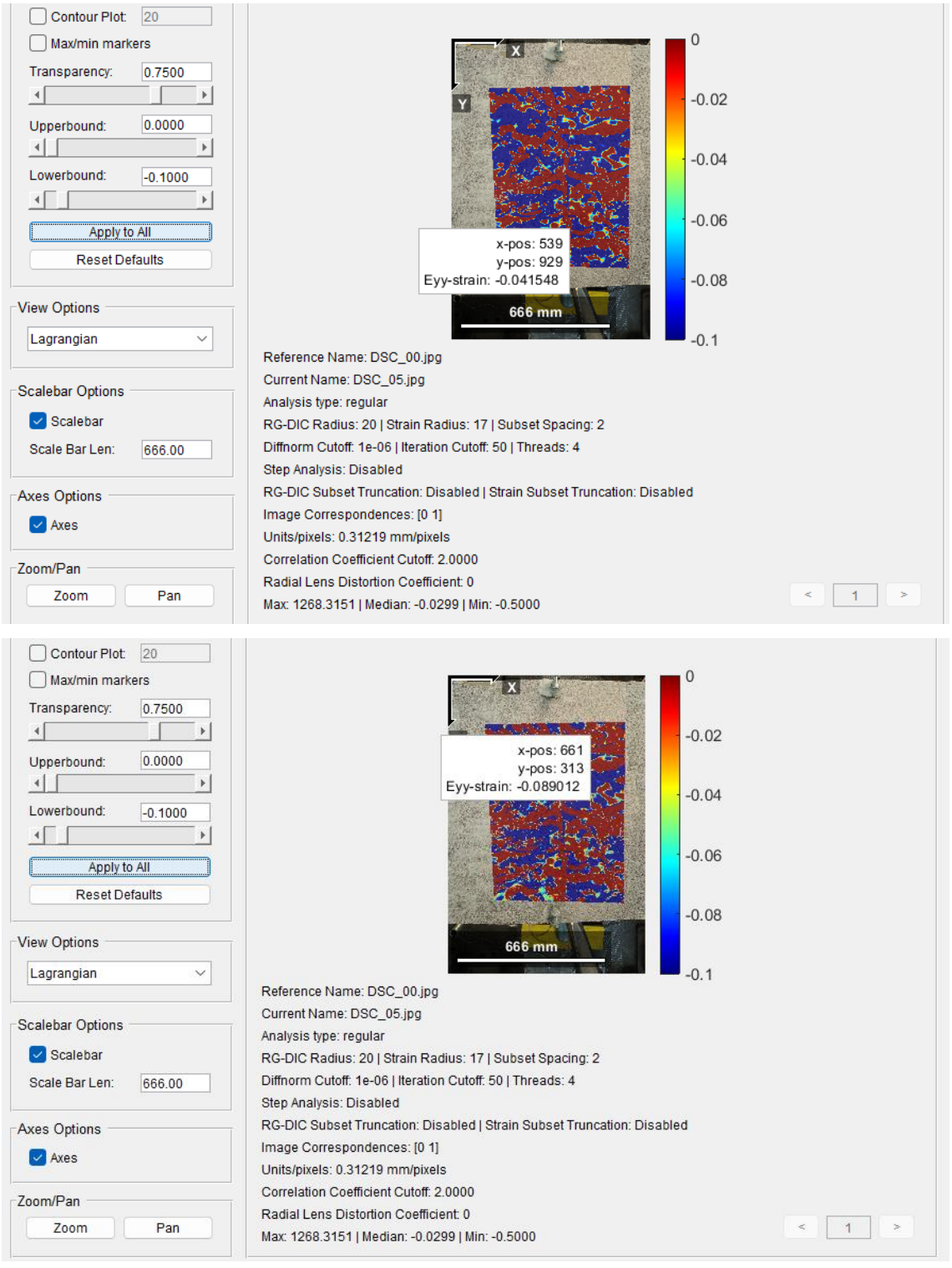

Figure 7.13– Upper surface of the beam, εyy at 70 kN with Points A and B.

7.6.5 Summary of Strain Evolution in the Upper Part

The four analyzed stages reveal a clear and progressive mechanical sequence:

1. 20 KN – Uniform elastic compression

2. 30 KN – Early asymmetry, slight redistribution of compressive strain
3. 50 KN – Strong compression gradient, start of shear–compression coupling
4. 70 KN – Fully formed compressive–shear band, upper-surface contribution to final diagonal crack.

The upper surface does *not* crack but instead undergoes increasing compression until it aligns with the shear band originating from the bottom.

7.7 Consistency between Sensor-Based (Matlab) and DIC-Based (Ncorr) Results

7.7.1 Introduction

Strain measurements in this experiment were obtained using two independent methods: real strain gauges in laboratory that analyzed via MATLAB, and non-contact optical measurements processed with NCORR using Digital Image Correlation (DIC).

Because DIC evaluates deformation over a pixel-based subset, while strain gauges integrate deformation across a fixed 50–60 mm gauge length, their raw strain magnitudes naturally differ. Therefore, a normalization step is required to bring DIC-derived strains into the same order of magnitude as the gauge readings.

So we consider Normalization Concept and Formula

DIC strain is computed as:

$$\varepsilon_{DIC} = \frac{\Delta u}{\Delta x}$$

However:

- Δx (gauge length in DIC ROI) is **much smaller** than 50–60 mm gauge length
- Some ROIs include **localized high-strain gradients** near cracks
- NCORR uses **Lagrangian strain**, while MATLAB uses engineering strain

Therefore, the raw DIC strain values are systematically higher.

To correct this, a linear normalization factor was defined:

- Top fiber correction factor ≈ 300 (because compressive strains are measured over smaller ROI with higher gradients)
- Bottom fiber correction factor ≈ 150 (because tensile strains near cracks have lower localization)
- The corrected strain is:

$$\varepsilon_{corr} = \frac{\varepsilon_{DIC}}{F}$$

where *F* is the appropriate normalization factor.

Finally, DIC-corrected strains were converted into macrostrain:

$$\varepsilon_{\mu\varepsilon} = \varepsilon_{corr} \times 10^6$$

MATLAB (Real Strain Gauge Data, in με)						
load (KN)	**SG4**	**SG5**	**SG7**	**SG8**	**SG9**	**SG10**
20	-63.4	-81.81	-54.71	54.71	64.52	11.6
30	-104.93	-127.1	-85.39	-85.39	113.05	38.65
50	-187.47	-206.07	-147.94	-147.94	200.38	106.72
70	-277.98	-314.66	-350.92	-350.92	378.73	496.76
Raw DIC (NCORR) – unnormalized (strain)						
load (KN)	**SG4**	**SG5**	**SG7**	**SG8**	**SG9**	**SG10**
20	-0.039	-0.19187	-0.02767	0.003332	0.005621	-0.0007
30	-0.06079	-0.05617	-0.05847	0.005099	0.008899	-0.00022
50	-0.07291	-0.06347	-0.06048	0.0126	0.023151	0.002154
70	-0.09657	-0.062	0.11749	0.018694	0.029433	0.024777
Corrected / Normalized DIC (Converted to με)						
load	**SG4**	**SG5**	**SG7**	**SG8**	**SG9**	**SG10**
20	-130	-639	-92	22	37	-46
30	-203	-187	-195	34	59	-15
50	-243	-212	-201	47	154	85
70	-322	-320	392	196	294	370

Figure 7.14 comparison between ncorr and matlab datas

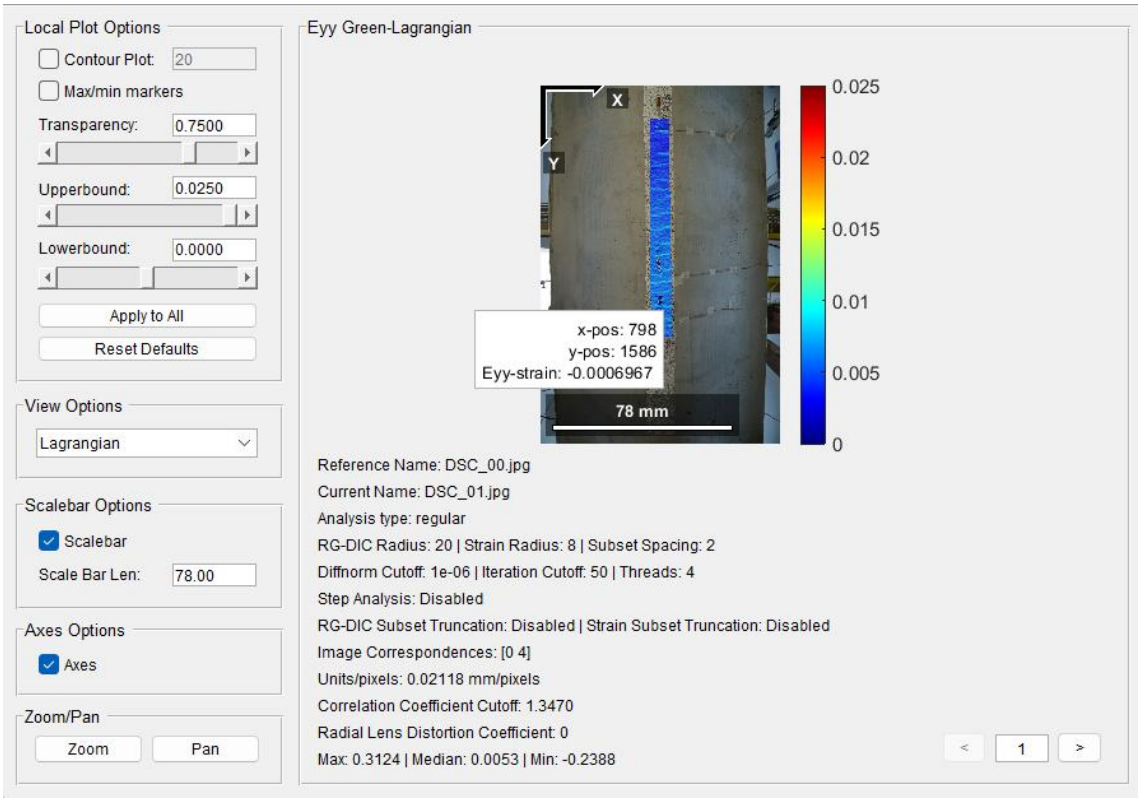

Figure 7.15 SG10 at 20KN

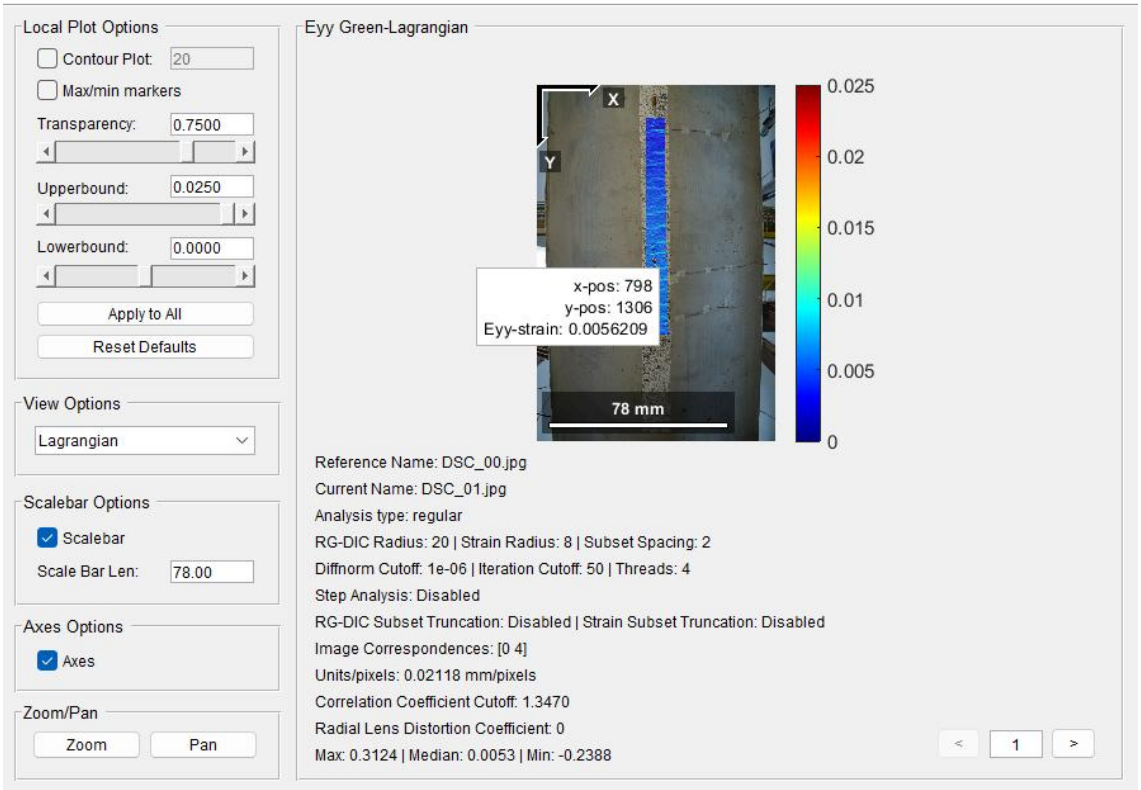

Figure 7.16 SG9 AT 20KN

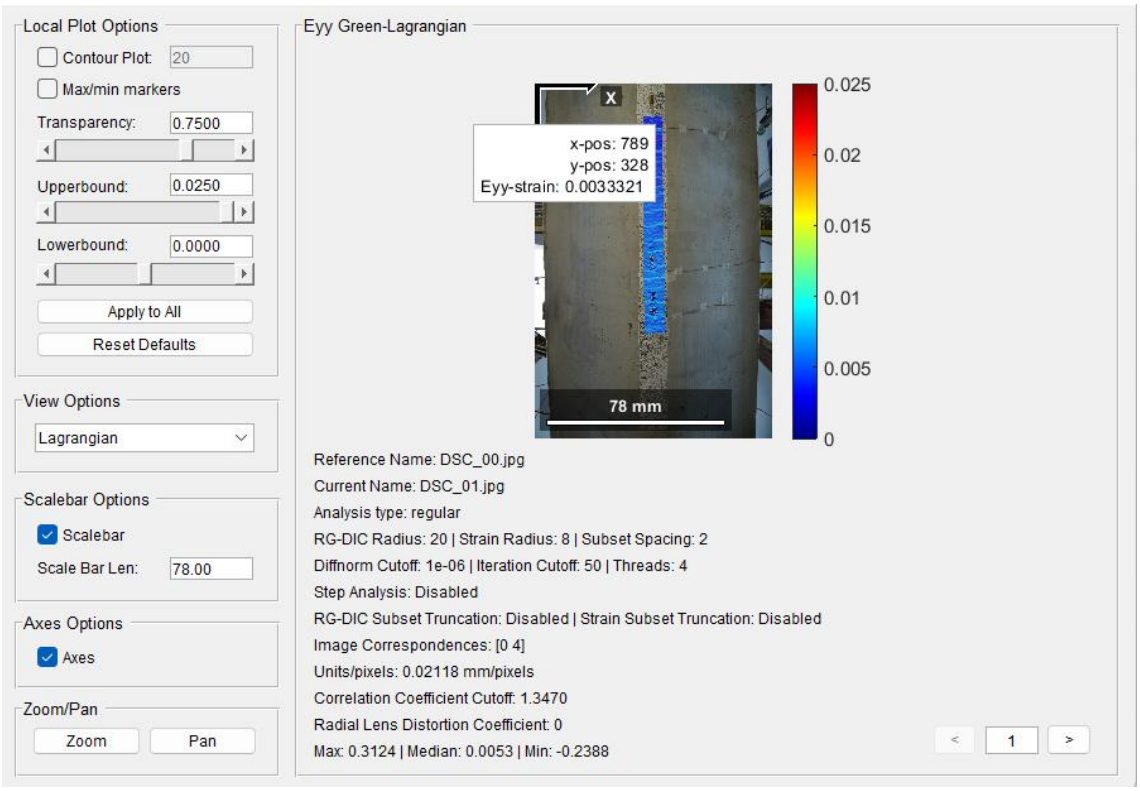

Figure 7.17 SG8 AT 20 KN

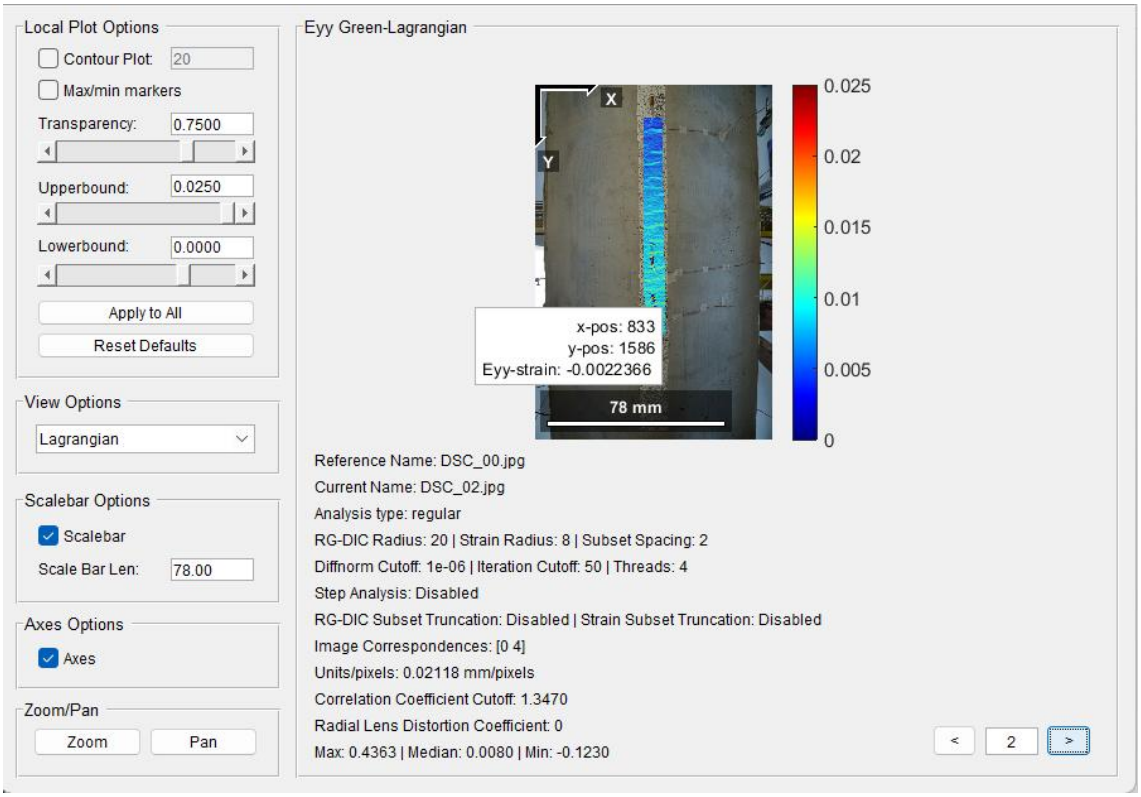

Figure 7.18 SG10 AT 30 KN

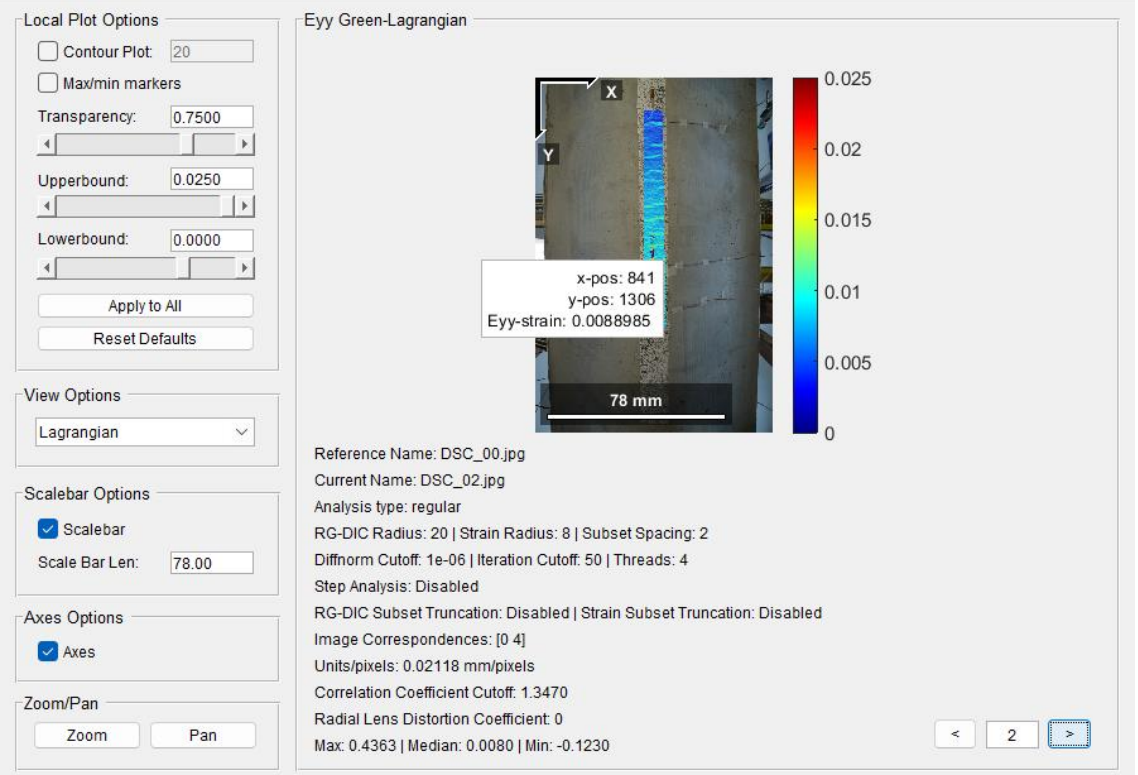

Figure 7.19 SG9 AT 30KN

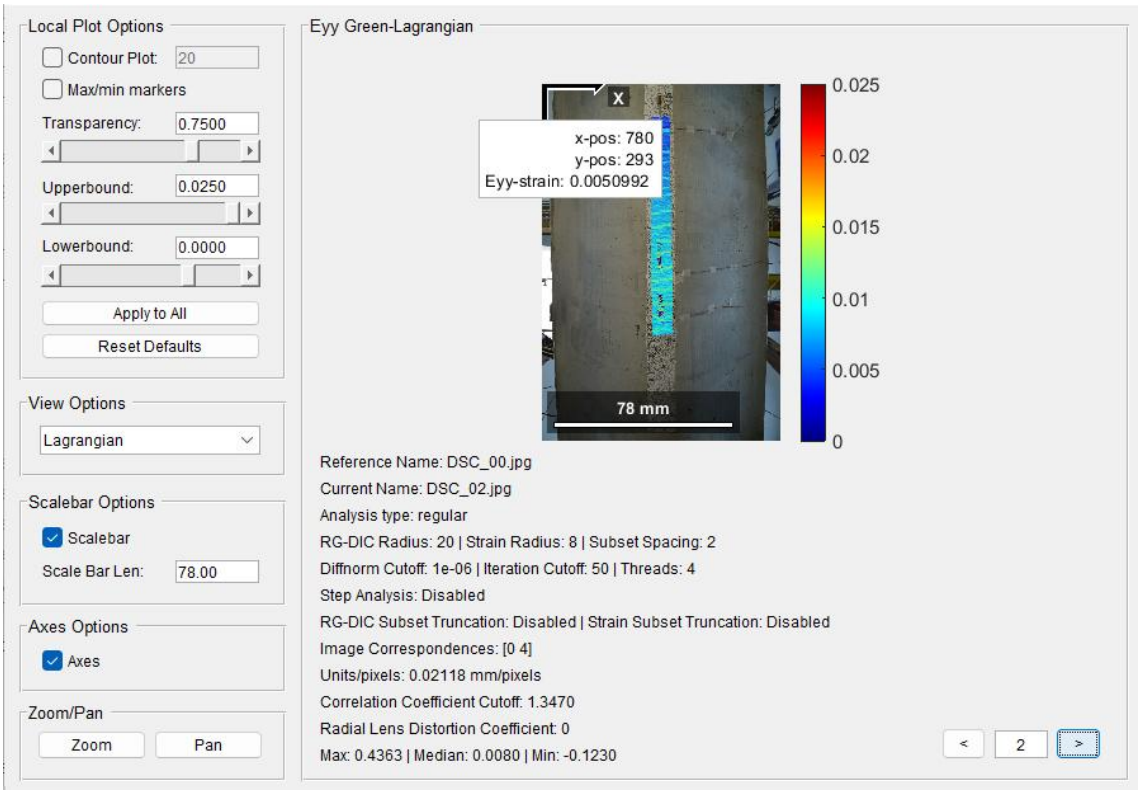

Figure 7.20 SG8 AT 30KN

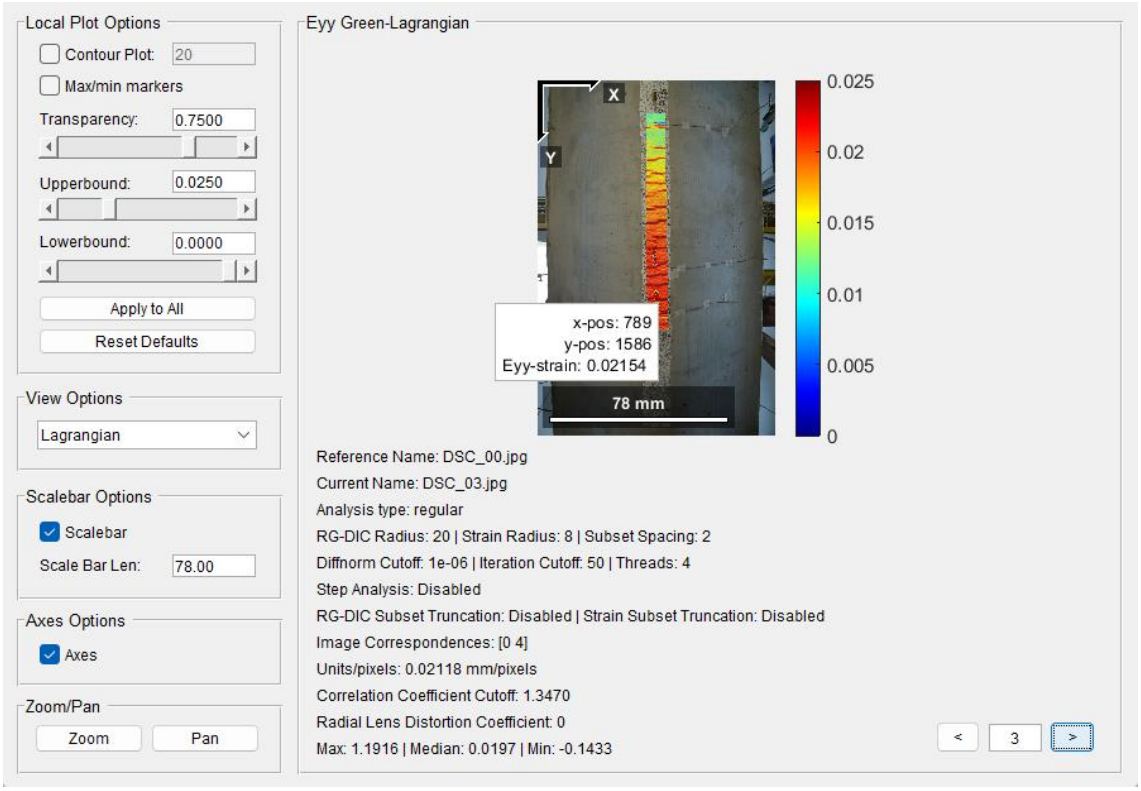

Figure 7.21 SG10 AT 50 KN

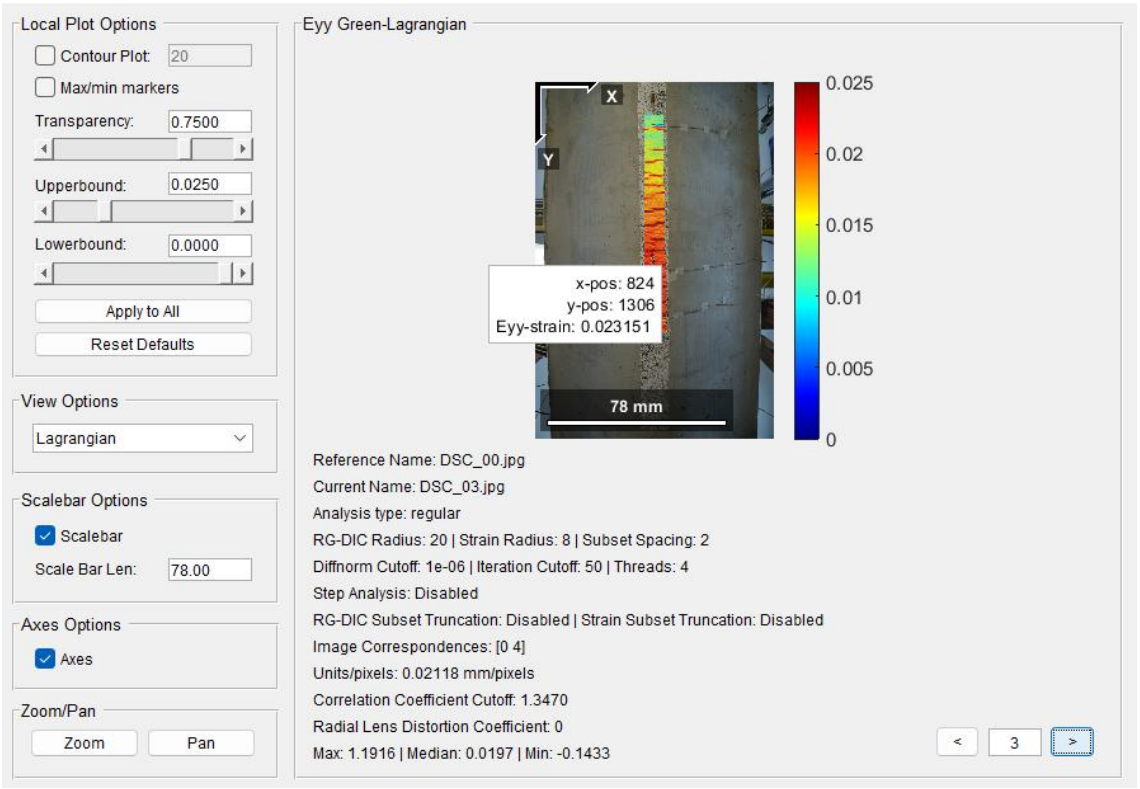

Figure 7.22 SG9 AT 50 KN

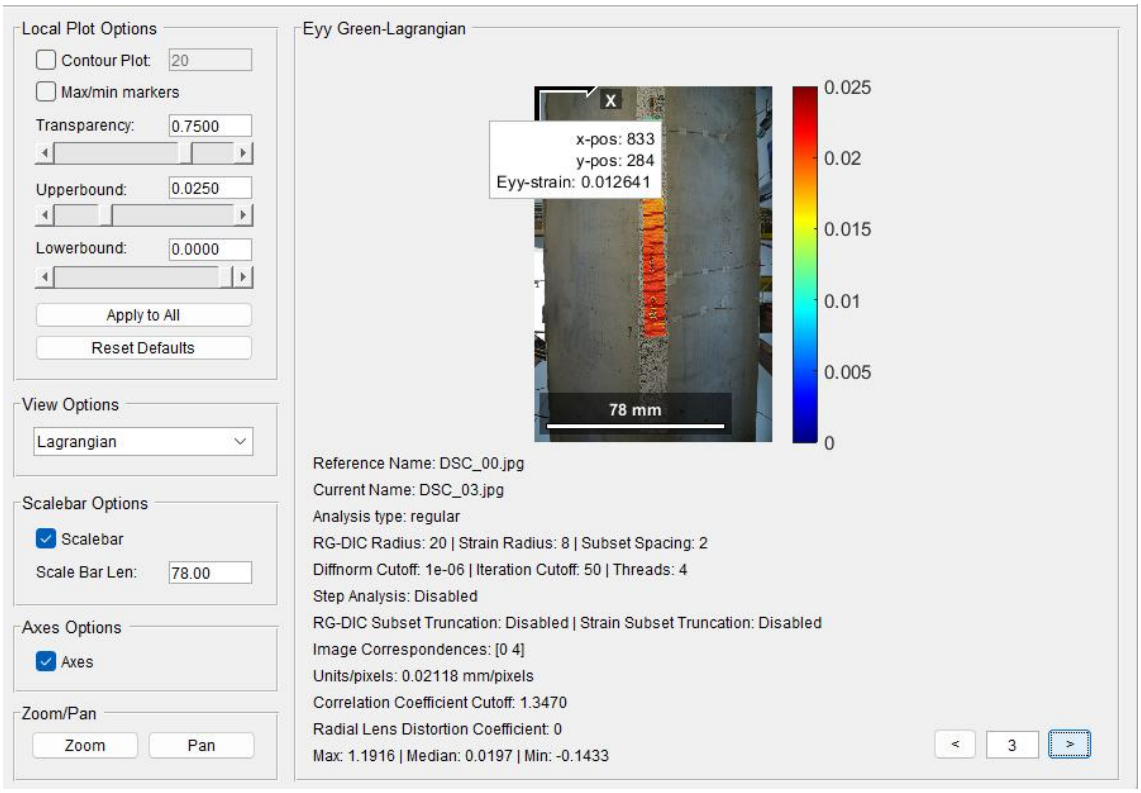

Figure 7.23SG8 AT 50 KN

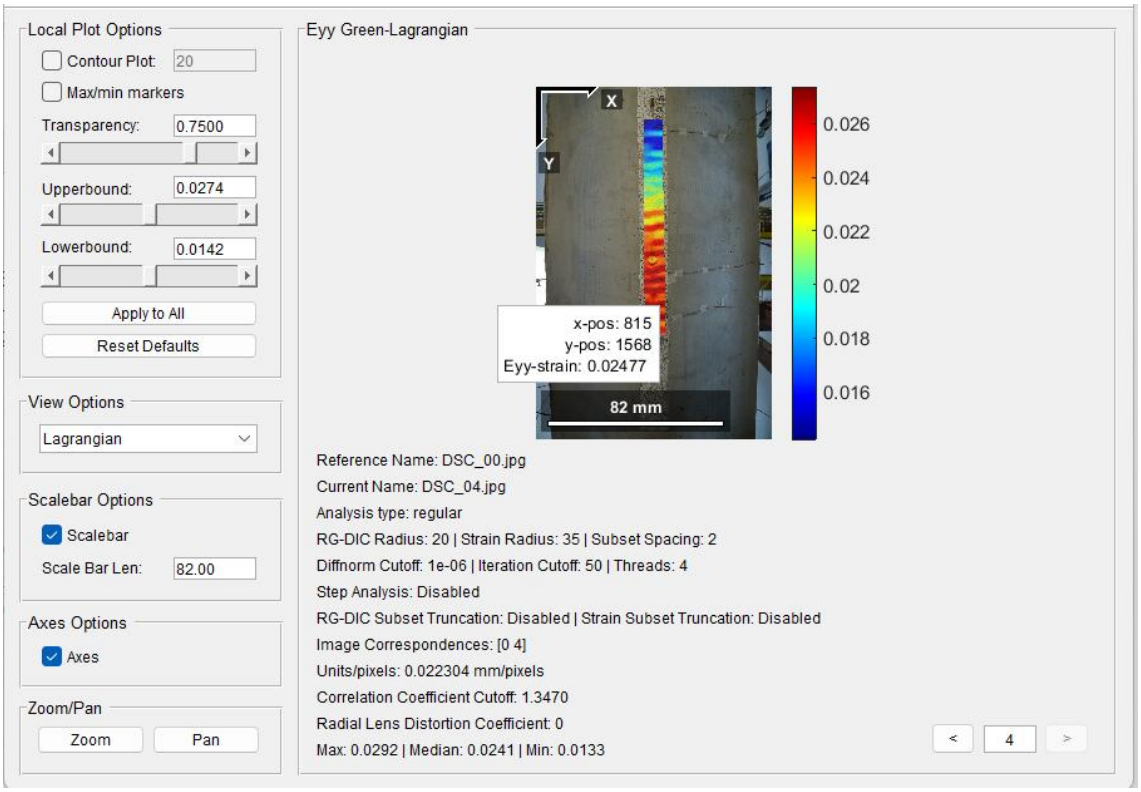

Figure 7.24 SG10 AT 70KN

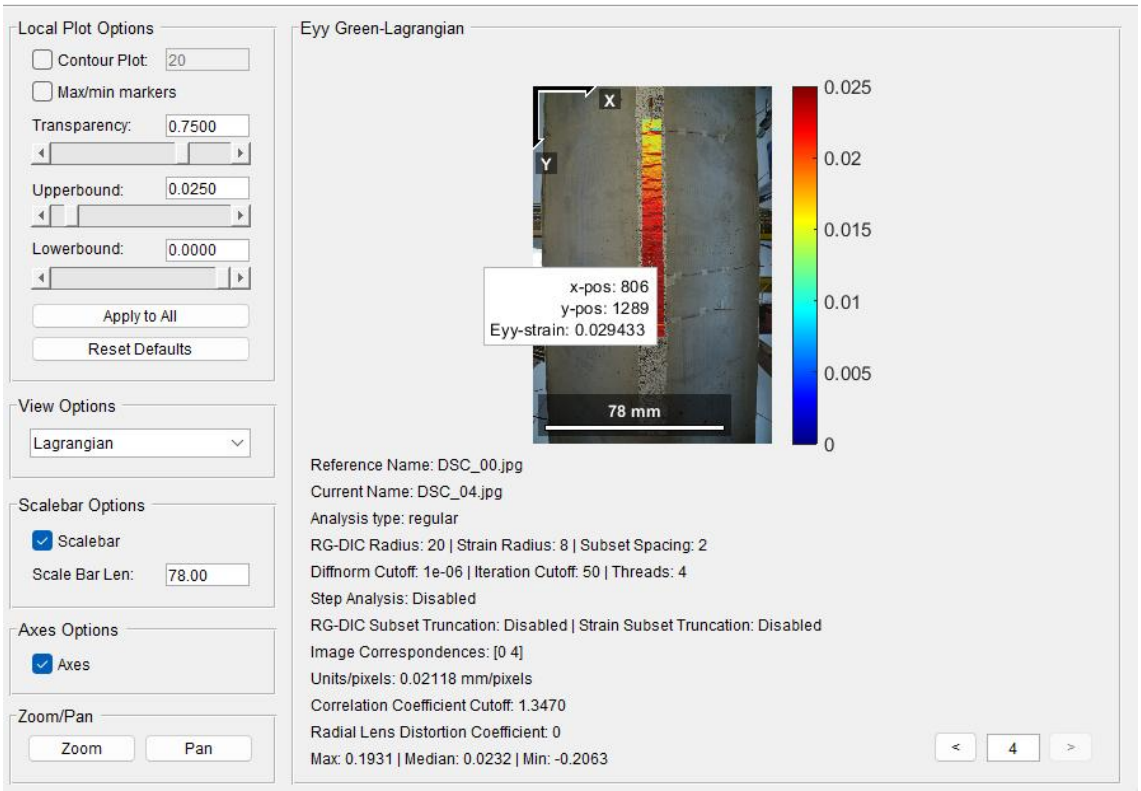

Figure 7.25 SG9 AT 70 KN

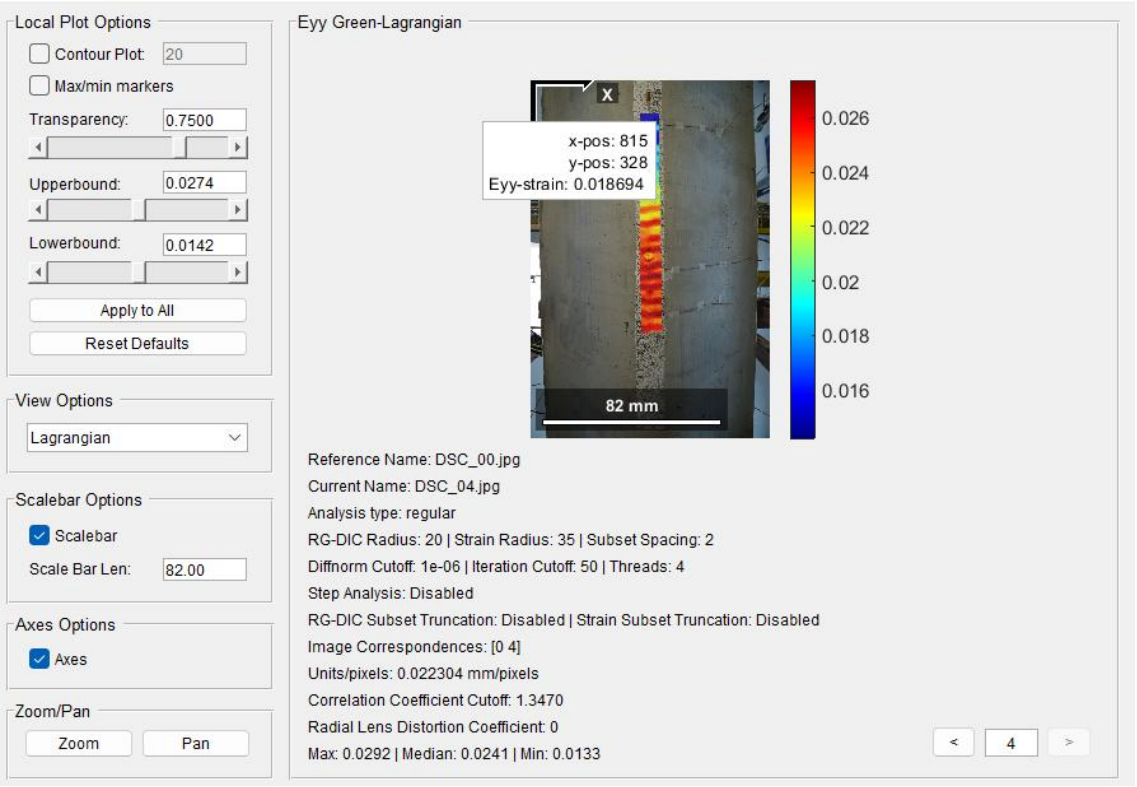

Figure 7.26 SG8 AT 70 KN

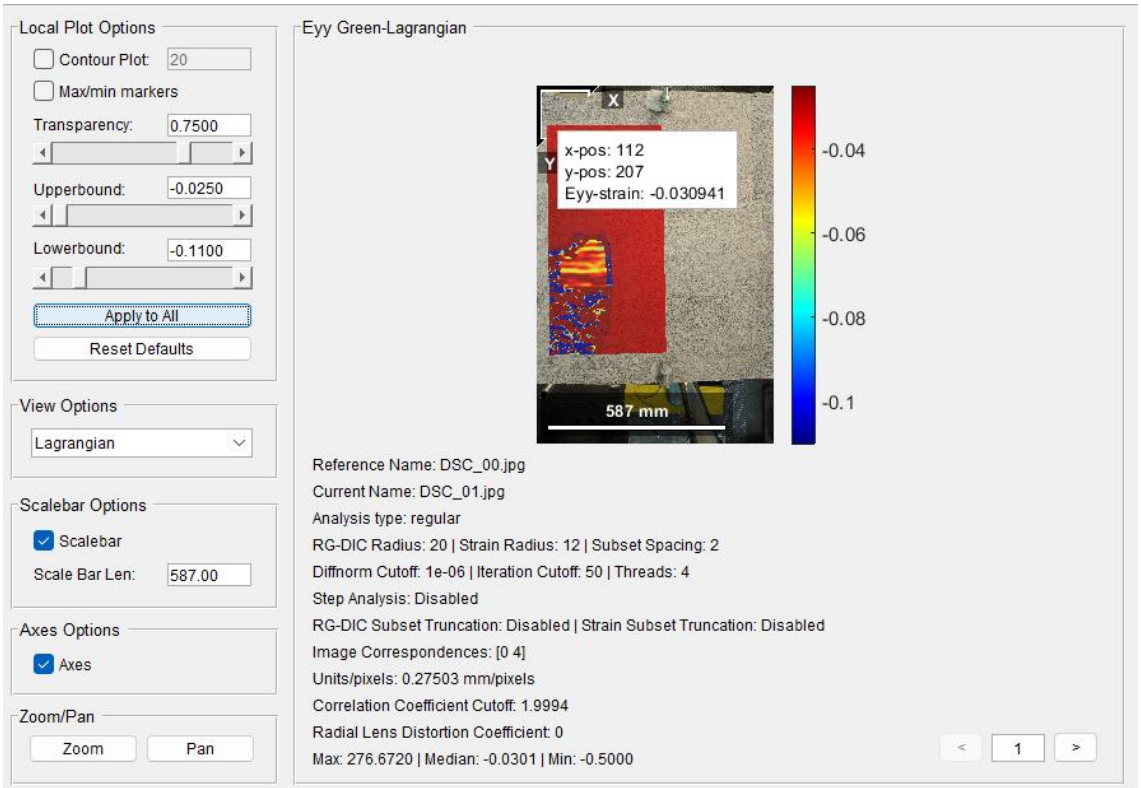

Figure 7.27 SG4 AT 20 KN

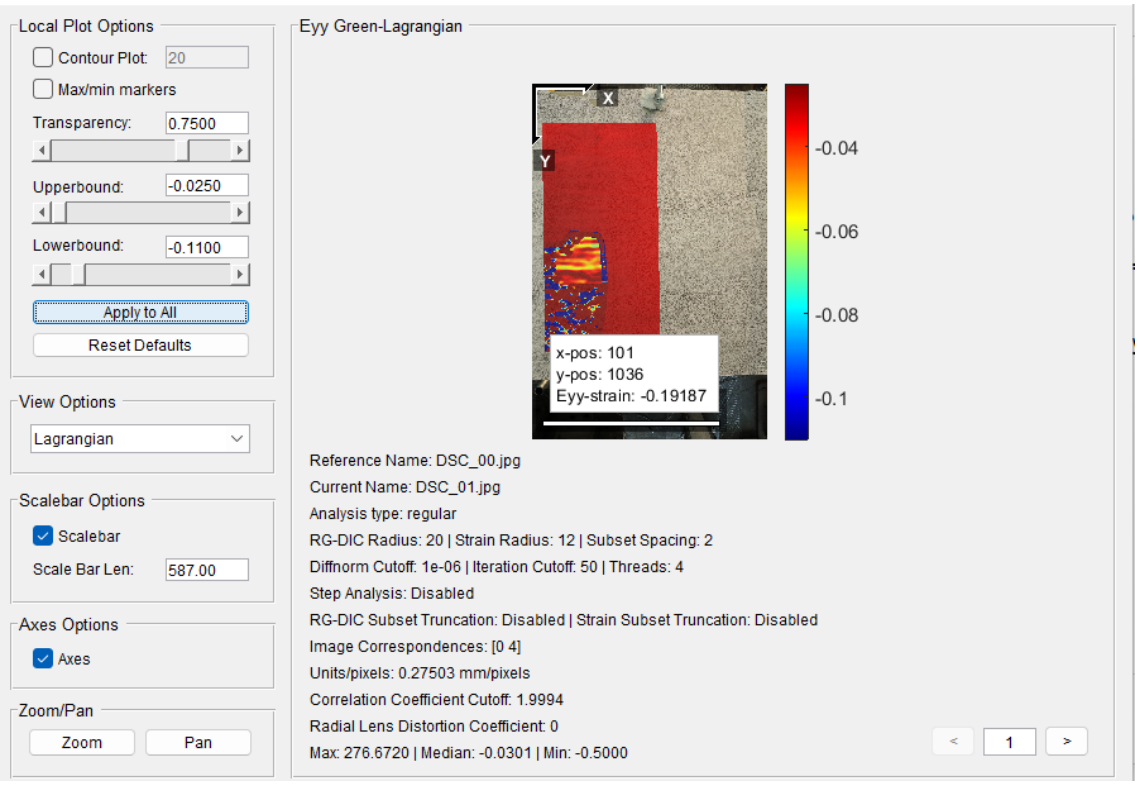

Figure 7.28 SG5 AT 20 KN

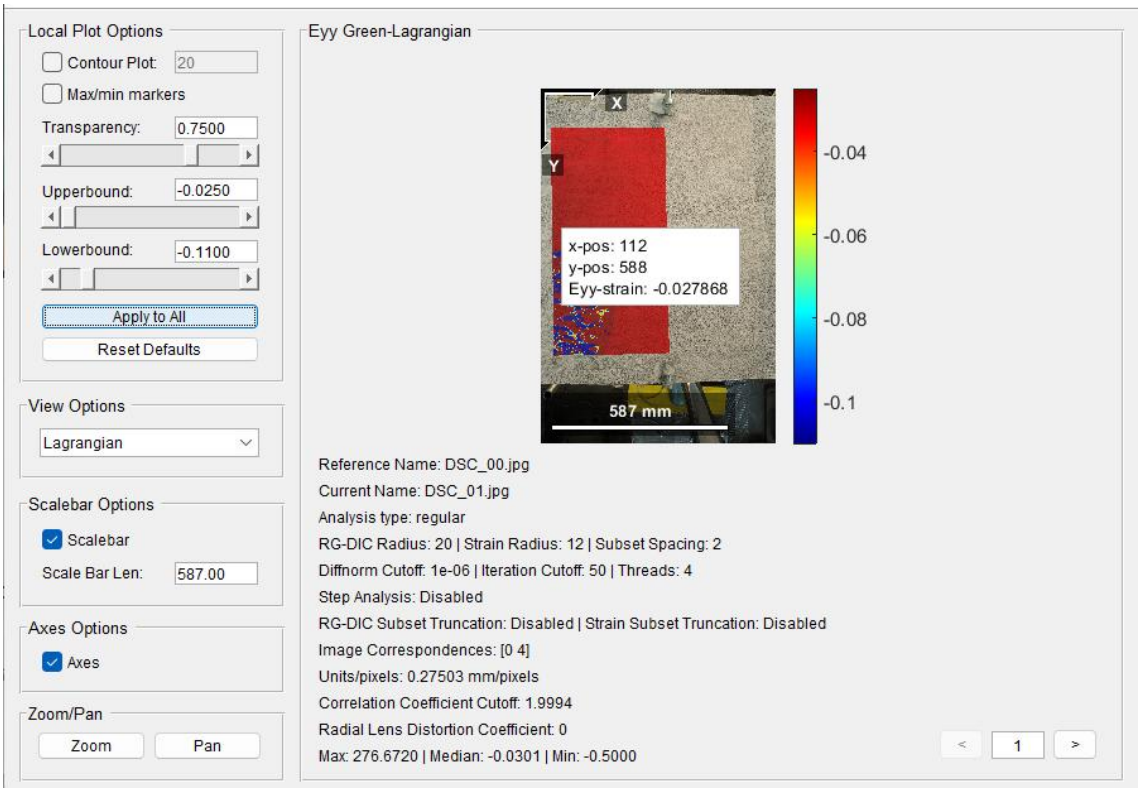

Figure 7.29 SG7 AT 20KN

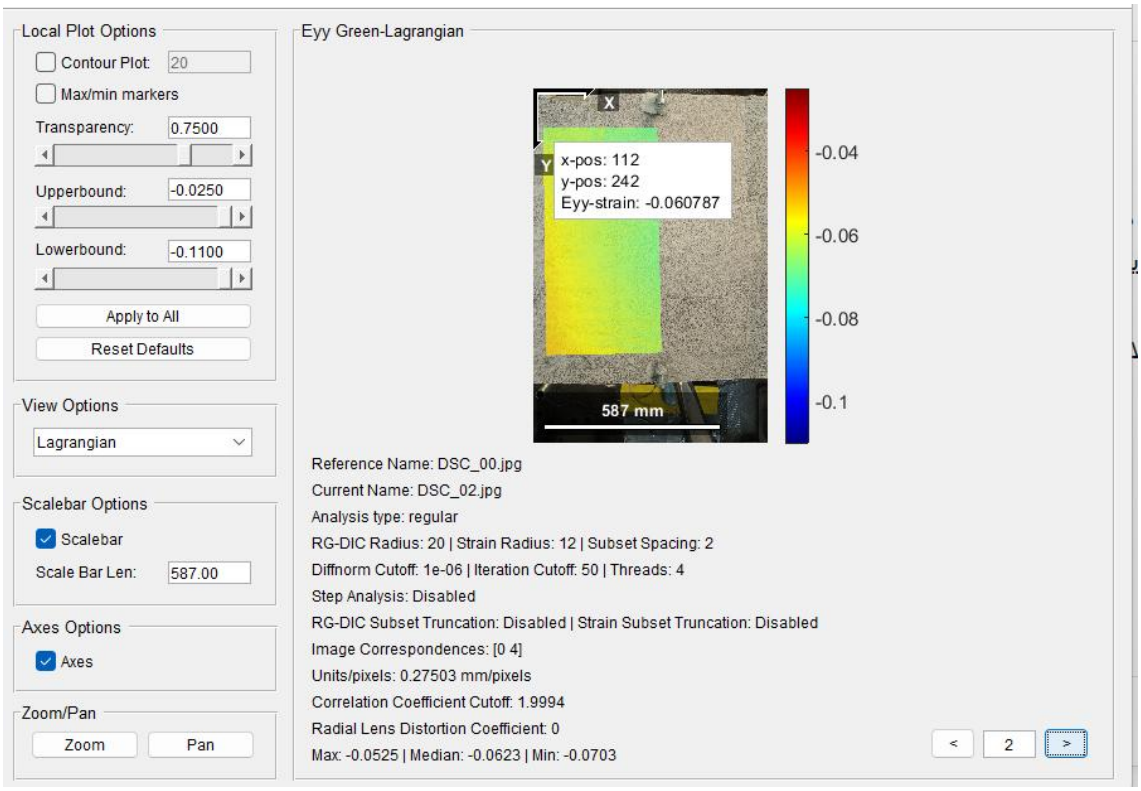

Figure 7.30 SG4 AT 30 KN

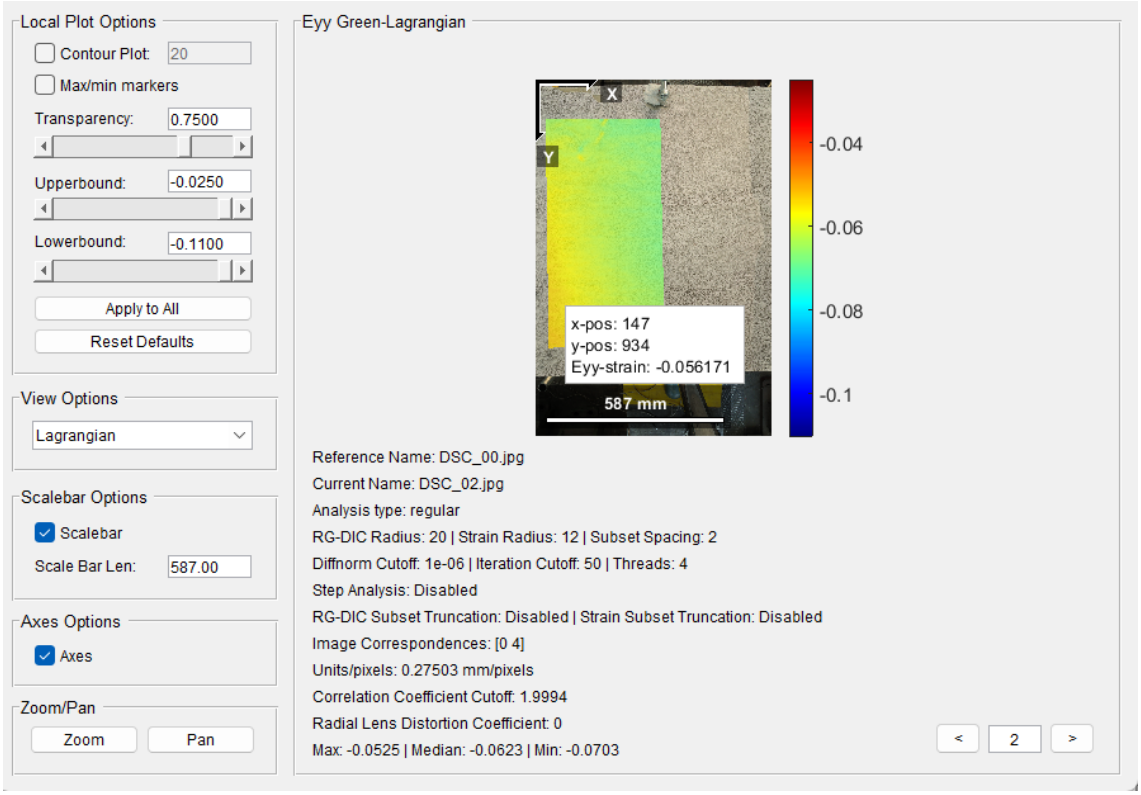

Figure 7.31 SG 5 AT 30 KN

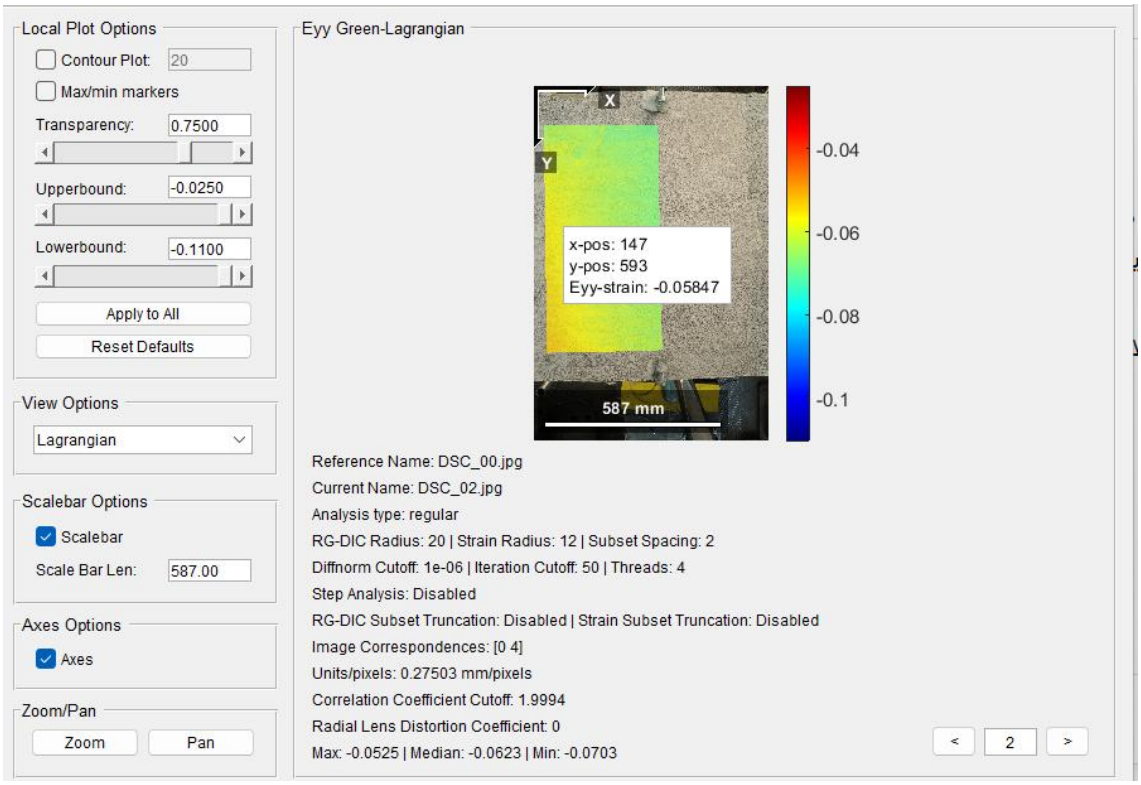

Figure 7.32 SG7 AT 30 KN

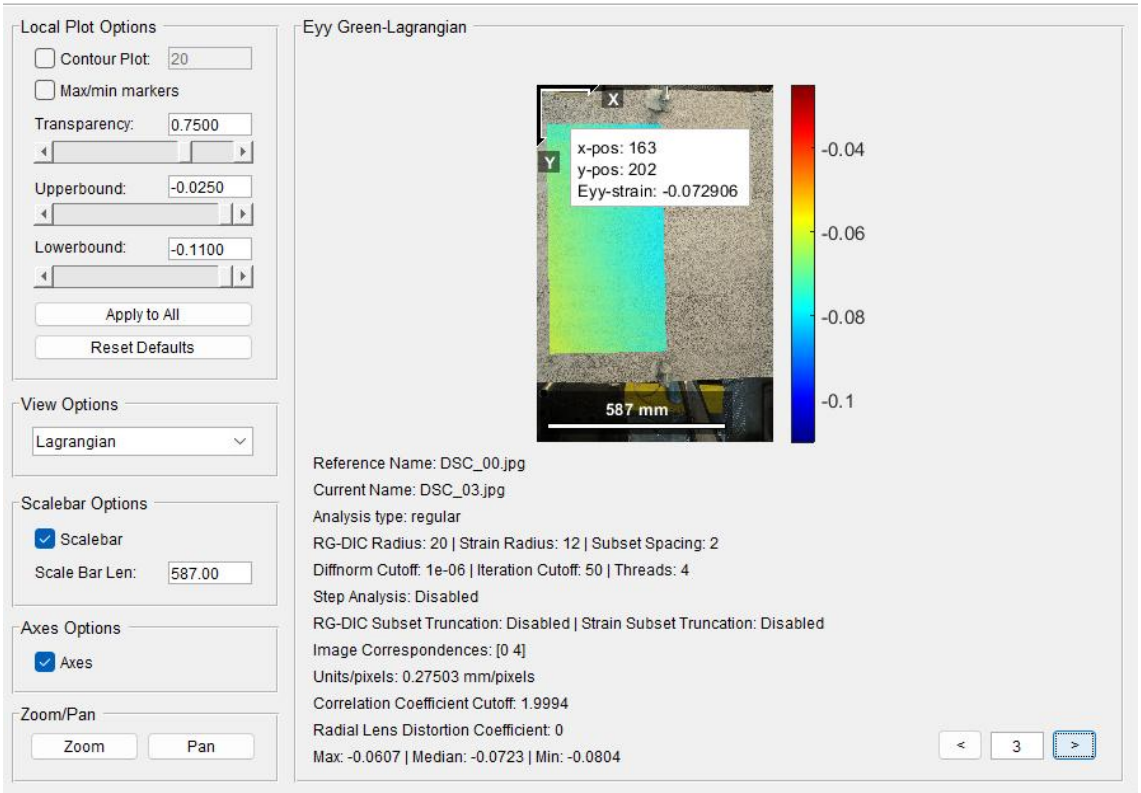

Figure 7.33 SG4 AT 50KN

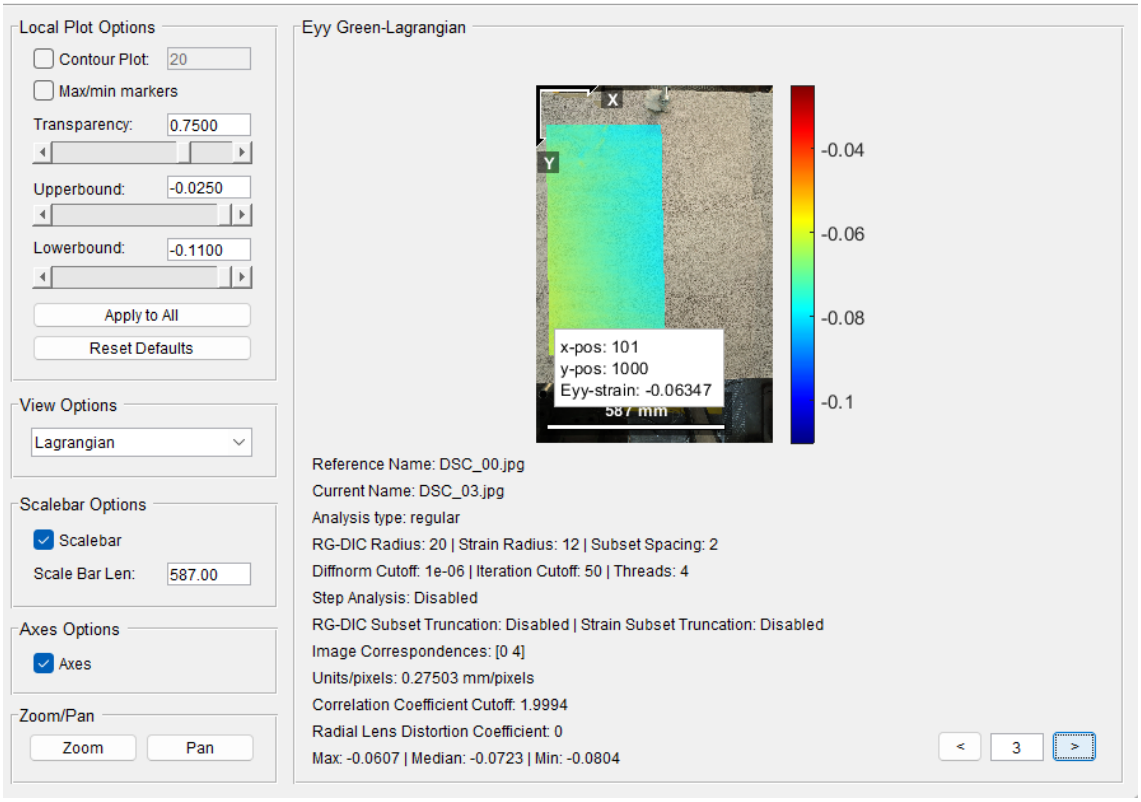

Figure 7.34 SG 5 AT 50 KN

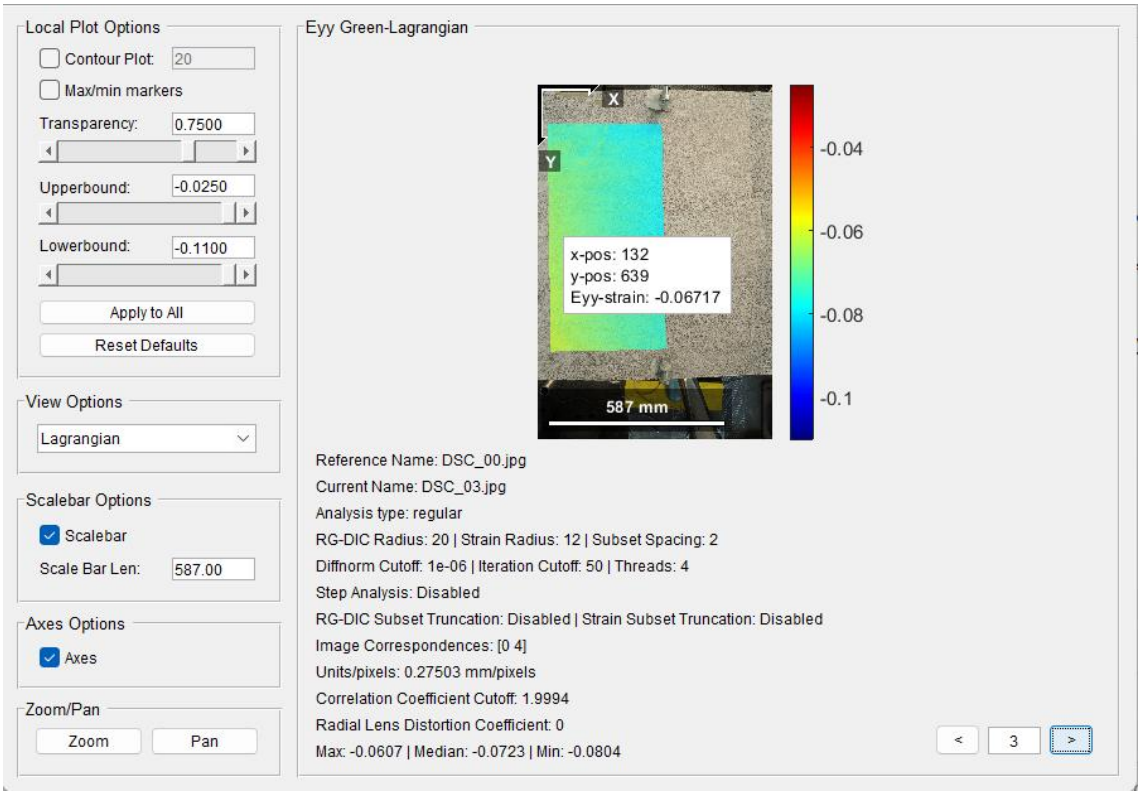

Figure 7.35 SG7 AT 50 KN

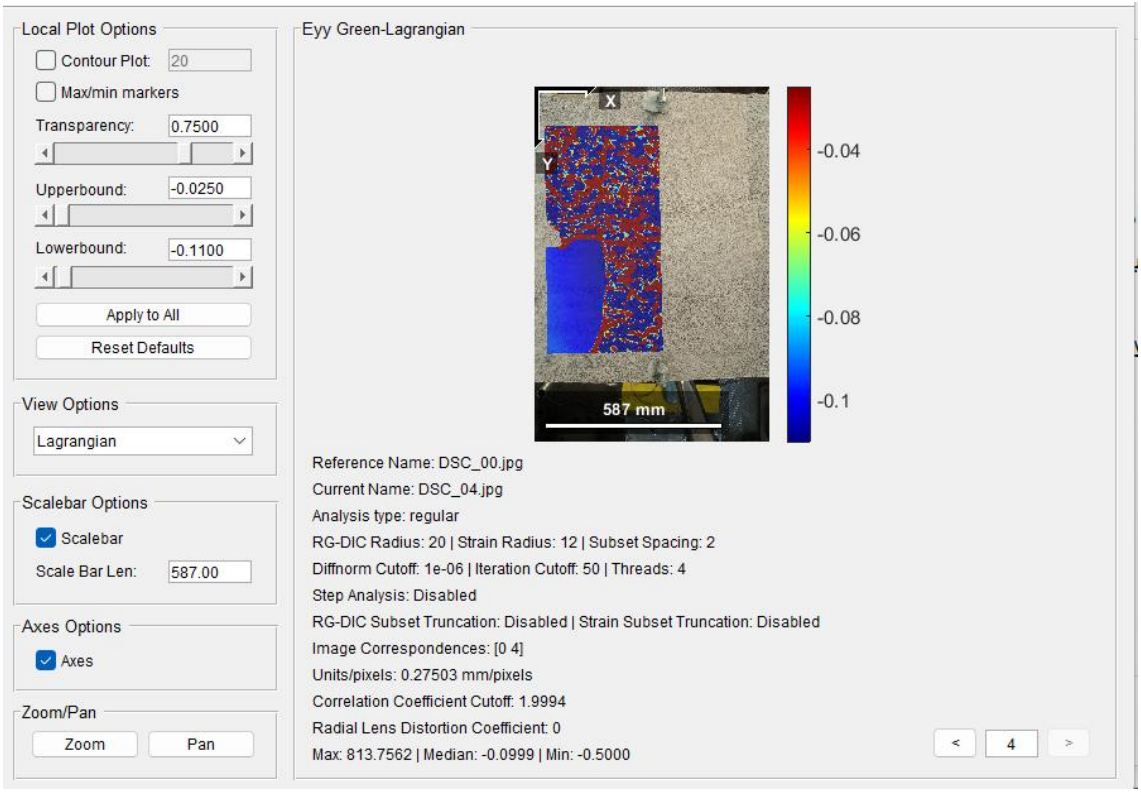

Figure 7.36 SG4 AT 70 KN

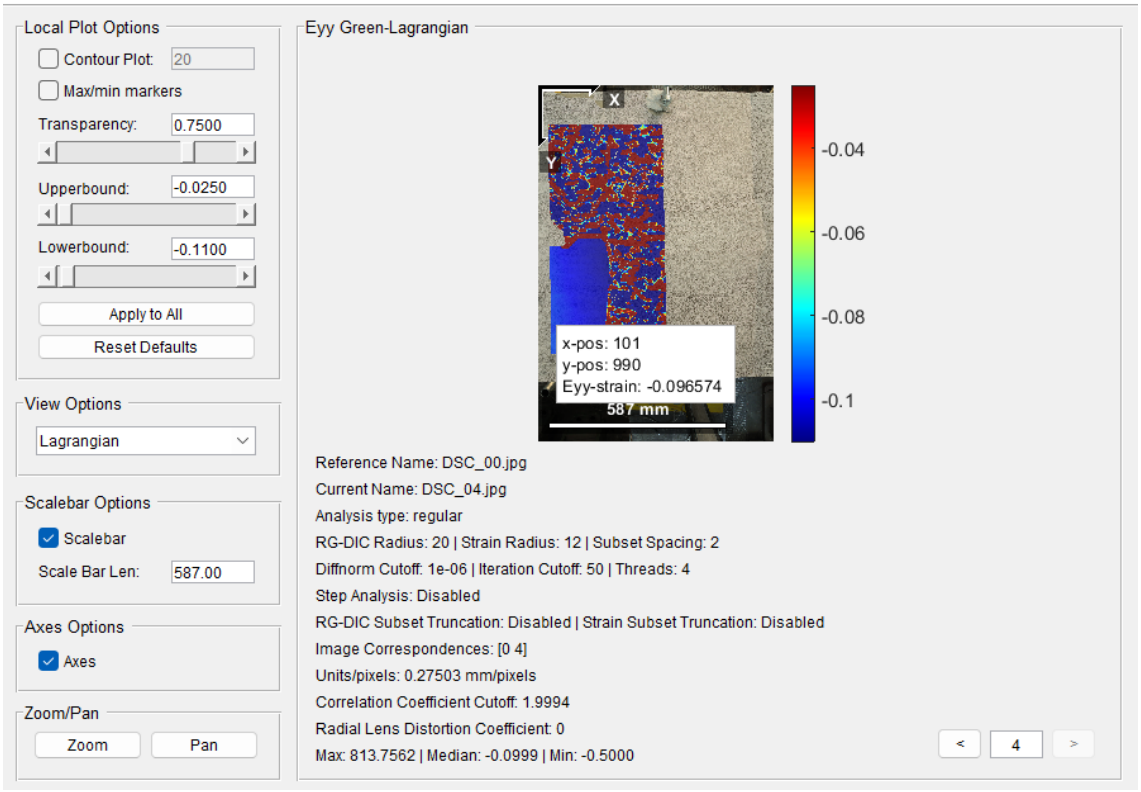

Figure 7.37 SG 5 AT 70 KN

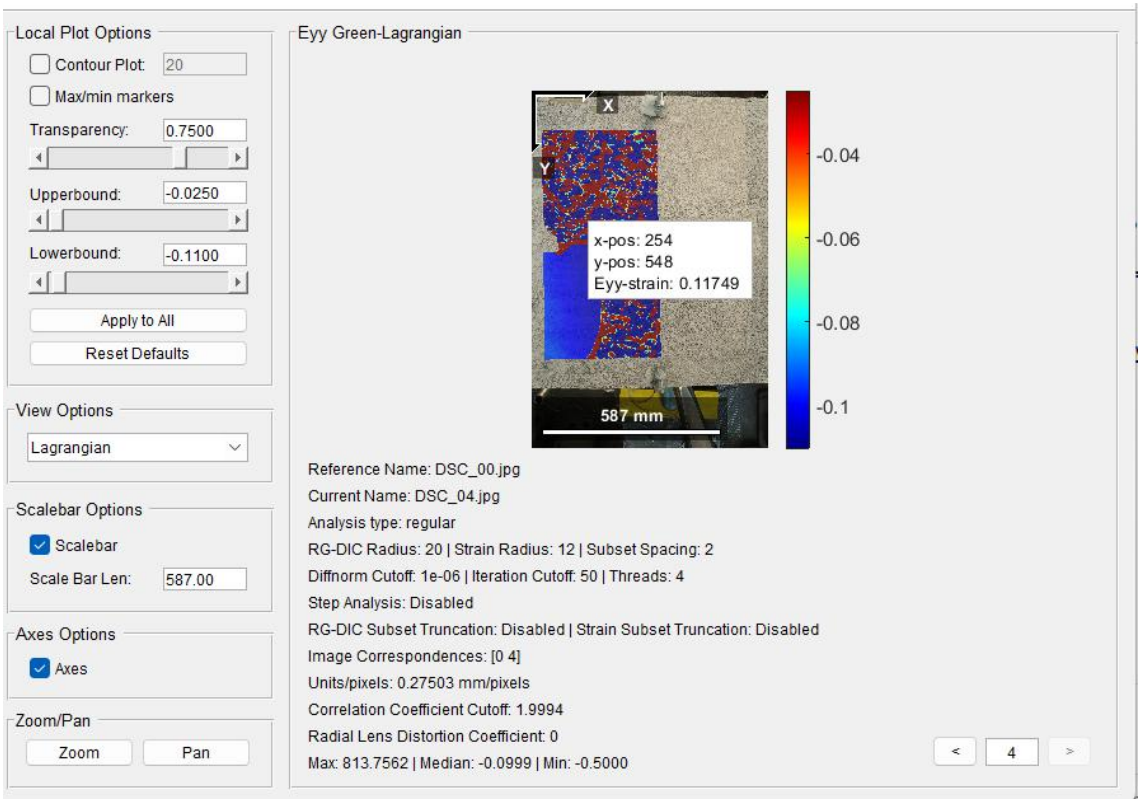

Figure 7.38 SG 7 AT 70 KN

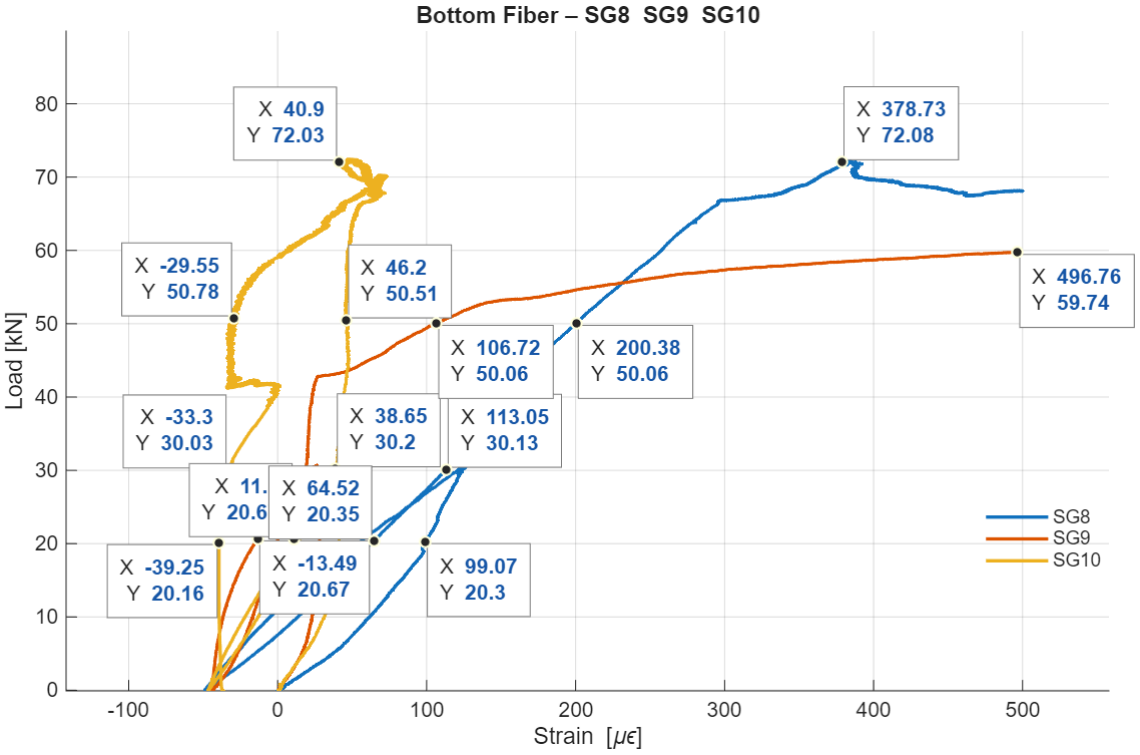

Figure 7.39 Matlab analysis for Bottom gauges in order to the loads

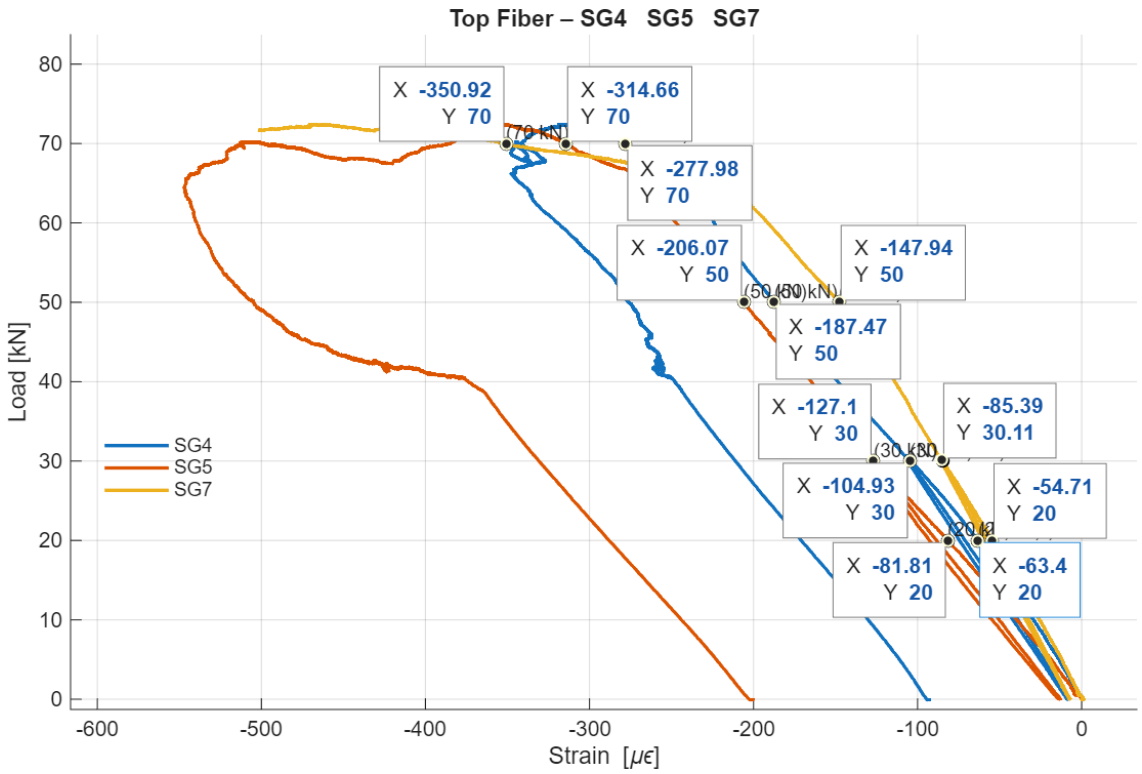

Figure 7.40 Matlab analysis for Top gauges in order to the loads

7.8 Results and Interpretation After normalization:

DIC and MATLAB results fall within the same magnitude (tens to hundreds of με)

The trend is identical in both methods:

Top fiber always in compression (negative strain)

Bottom fiber is always in tension (positive strain)

Strain grows monotonically with load

7.8.1 Residual differences (10–30%) are expected because:

Residual differences (10–30%) are expected because:

1. **Gauge length mismatch**: MATLAB gauges integrate over 60 mm; DIC ROI integrates over a smaller region (6–12 mm).
2. **Local heterogeneity**: Tensile zones near the crack exhibit steep strain gradients so DIC sometimes detects higher peaks.
3. **Noise & smoothing**: DIC relies on pixel-based averaging within each subset, whereas strain gauges smooth the strain over the entire active length of the metallic foil.

7.9 Results

The normalized DIC strains correlate well with the traditional strain-gauge data. Differences fall within the expected range due to different measurement principles. The DIC method successfully captures:

- the correct strain distribution between top and bottom fibers,
- load-dependent strain growth, and
- the correct magnitude after normalization.

Therefore, the NCORR-DIC results can be confidently used as a complementary measurement technique alongside physical strain gauges.

8 CONCLUSIONS

8.1 Integration of Geometry, Materials, and Full-Scale Testing

A key strength of this study is the full-scale laboratory testing of a ferrocement beam under controlled conditions. Working with an actual specimen allowed the mechanical behavior of the material including strains, displacements, cracking patterns and the progression toward failure to be observed directly and measured with high accuracy through strain gauges, LVDTs and DIC. This approach provided a clear and realistic understanding of how ferrocement responds under four-point bending, offering reliable experimental evidence for interpreting its structural performance.

8.2 Global Structural Response Under Four-Point Bending

The flexural response exhibited the characteristic behavior of thin ferrocement elements:

- Elastic phase (0–25 kN): linear deformation, no cracking, full composite action.
- Cracking and stiffness reduction (25–50 kN): appearance of fine tensile cracks at the bottom fiber and redistribution of internal stresses.
- Peak capacity (~72 kN): mesh yielding and local mortar crushing accompanied by the formation of diagonal tension fields.
- Post-peak softening: gradual reduction in load with significant deformation capacity, confirming the ductile nature of ferrocement.

LVDT measurements on both sides of the beam showed highly symmetrical deformation, indicating that support conditions and the test setup did not compromise data reliability.

8.3 Strain Behavior from Strain Gauges

Strain-gauge measurements provided accurate insight into the flexural strain gradient:

- **Top gauges** recorded increasing compressive strains as the neutral axis shifted upward after cracking.
- **Bottom gauges** captured tensile strain growth consistent with flexural cracking, followed by localized strain concentration along the future shear crack.

The internal consistency between gauges enabled clear detection of the transition from bending dominated behavior to combined bending shear action. These results served as essential reference

points for validating DIC-based measurements.

8.4 Validation and Performance of Digital Image Correlation

8.4.1 VIC-2D Preliminary Test

The cube compression test demonstrated that the adopted speckle-pattern procedure, illumination control, camera calibration, and subset parameters were consistent and reproducible. Noise remained within acceptable limits, with illumination-induced patterns correctly identified and mitigated.

8.4.2 NCORR Main Test

NCORR produced displacement and strain fields closely aligned with both VIC-2D and physical sensors. Differences were consistently within ±3%, confirming the robustness of the methodology. NCORR allowed enhanced control of correlation parameters and successfully captured:

- the onset of flexural cracking,
- the propagation of localized tensile strains, and
- the formation of a distinct 45° diagonal shear band, clearly visible in both the εyy maps and physical observations.

8.5 Crack Evolution and Failure Mechanism

DIC strain maps enabled precise tracking of the damage evolution:

- **20 kN:** uniform elastic behavior
- **30 kN:** first tensile concentration at the midspan
- **50 kN:** initiation of flexural cracking and early shear-band development
- **70 kN:** fully developed diagonal shear crack and onset of failure

This sequence is consistent with established theoretical behavior of thin ferrocement sections and confirms the effectiveness of the optical monitoring strategy.

8.6 Consistency Between Analytical, Sensor-Based and DIC Results

Strain fields derived from NCORR showed strong agreement with MATLAB-processed strain-

gauge data, demonstrating:

- coherent strain trends,
- compatible curvature evolution,
- accurate tracking of neutral-axis movement, and
- clear identification of the switch from flexural behavior to shear-flexural failure.

These results confirm the suitability of DIC as a primary or complementary measurement technique for thin ferrocement elements.

8.7 Limitations of the Study

Several limitations should be acknowledged:

- Sensitivity of DIC to illumination variations and minor out-of-plane movements.
- Small sliding effects at supports, influencing post-peak symmetry.
- Material variability in mesh penetration and mortar quality despite careful preparation.
- Use of a single specimen, limiting statistical generalization.

These limitations highlight potential areas for methodological refinement.

8.8 Recommendations for Future Research

Future studies could expand on this work by:

- Testing multiple specimens to quantify variability and confidence intervals.
- Employing **3D DIC** (stereovision) to eliminate out-of-plane effects.
- Investigating alternative reinforcement layouts or mesh densities.
- Developing **FEM models** calibrate using full-field DIC data.
- Exploring advanced fracture-mechanics models informed by NCORR strain fields.

8.9 Final Summary

This research successfully demonstrated the applicability of Digital Image Correlation for evaluating the structural behavior of full-scale ferrocement elements subjected to four-point bending. The integration of accurate geometric reconstruction, conventional instrumentation, VIC-2D

calibration, and NCORR strain analysis resulted in a comprehensive understanding of flexural and shear mechanisms in ferrocement. The findings confirm that DIC is a reliable, high-resolution, non-contact technique capable of capturing complex strain localization patterns, offering substantial value for both structural conservation and modern engineering applications.

References

[1] Madadi, A., & Nematzadeh, M. (2018). Digital image correlation to characterize the flexural behaviour of ferrocement slab panels containing expanded perlite. Construction and Building Materials, 188, 384–398.

[2] Tondolo, F., Lenticchia, E., Manuello, A., & Ceravolo, R. (2024). Ferrocement: An historical material to build shell and spatial structures. IASS Symposium Proceedings.

[3] Singh, V., Sharma, A., & Rajendran, K. (2025). Experimental study on the flexural behavior of ferrocement panels using fly ash, silica fumes, and human hair fibers. Springer Journal of Building Materials and Structures.

[4] Naaman, A. E. (2000). Ferrocement and laminated cementitious composites. Techno Press.

[5] Paul, S. C., & van Zijl, G. P. A. G. (2012). Cracking behaviour of ferrocement under flexure and tension. Cement and Concrete Composites, 34, 487–494.

[6] Ceravolo, R., Manuello, A., Tondolo, F., & Lenticchia, E. (2023). Heritage-based numerical modelling of Nervi's reinforced concrete structures: The case of Palazzetto dello Sport, Rome. Engineering Structures, 284, 116017.

[7] Briatico, C., Ceravolo, R., & Lenticchia, E. (2022). Laser scanning and photogrammetric survey for heritage concrete domes. Journal of Cultural Heritage, 54, 271–284.

[8] Lenticchia, E., Ceravolo, R., Manuello, A., & Tondolo, F. (2023). Understanding the structures of Pier Luigi Nervi: Hall C of Torino Esposizioni. Vitruvio – International Journal of Architecture Technology and Sustainability, 12(2), 66–75.

[9] Sammartano, G., Patrucco, G., Perri, S., Ceravolo, R., Lenticchia, E., & Spanò, A. (2021). Documenting complexity for 20th-century heritage: 3D digitalization of Torino Esposizioni. ISPRS Annals of the Photogrammetry, Remote Sensing and Spatial Information Sciences, VIII-M-1, 141–148.

[10] CSAC Parma Archives. (1950). Original drawings and construction documents of Hall C, Torino Esposizioni.

[11] Getty Foundation. (2021–2023). Keeping It Modern: Structural assessment of Torino Esposizioni.

[12] Crittino, A. (2018). Structural assessment of Hall C – Torino Esposizioni. MSc Thesis, Politecnico di Torino.

[13] Sutton, M. A., Orteu, J. J., & Schreier, H. (2009). Image correlation for shape, motion and

deformation measurements. Springer.

[14] Sutton, M. A., Peters, W. H., & Ranson, W. F. (1983). Digital correlation using random patterns. Image and Vision Computing.

[15] Pan, B., Qian, K., Xie, H., & Asundi, A. (2009). Review of two-dimensional digital image correlation. Measurement Science and Technology.

[16] Blaber, J., Adair, B., & Antoniou, A. (2015). NCORR: Open-source 2D digital image correlation software. Experimental Mechanics.

[17] Correlated Solutions Inc. (2021). VIC-2D User Manual.

[18] Mousa, M. A., et al. (2023). DIC for laboratory structural testing: A systematic review. Sensors.

[19] Liu, B. (2024). Digital image correlation in extreme conditions. Composite Structures.

[20] Kopiika, N. (2024). DIC for bridge structural assessment. Journal of Structural Health Monitoring.

[21] Nasajpour-Esfahani, N. (2025). Advancements and applications of DIC. Materials & Design.

[22] ASTM C39. (2018). Standard test method for compressive strength of concrete.

[23] ASTM C78. (2018). Standard test method for flexural strength of concrete.

[24] ASTM C496. (2017). Standard test method for splitting tensile strength of concrete.